

นิกเกิลฟอสไฟด์บนถ่านกัมมันต์ สำหรับปฏิกิริยาไฮโดรดีออกซิเจนชั้นของ
น้ำมันปาล์ม



นางสาวมัสติกา พิมพ์สุตะ

วิทยานิพนธ์นี้เป็นส่วนหนึ่งของการศึกษาตามหลักสูตรปริญญาวิทยาศาสตรดุษฎีบัณฑิต

สาขาวิชาเคมี

มหาวิทยาลัยเทคโนโลยีสุรนารี

ปีการศึกษา 2559

**NICKEL PHOSPHIDE ON ACTIVATED CARBON FOR
HYDRODEOXYGENATION OF PALM OIL**

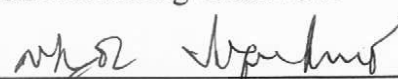


**A Thesis Submitted in Partial Fulfillment of the Requirements for the
Degree of Doctor of Philosophy in Chemistry
Suranaree University of Technology
Academic Year 2016**

**NICKEL PHOSPHIDE ON ACTIVATED CARBON FOR
HYDRODEOXYGENATION OF PALM OIL**


Suranaree University of Technology has approved this thesis submitted in partial fulfillment of the requirements for the Degree of Doctor of Philosophy.

Thesis Examining Committee




(Asst. Prof. Dr. Sanchai Prayoonpokarach)

Chairperson



(Prof. Dr. Jatuporn Wittayakun)

Member (Thesis Advisor)




(Assoc. Prof. Dr. Nurak Grisdanurak)

Member

SUPUNNEE J.


(Dr. Supunnee Junpirom)

Member




(Dr. Pongtanawat Khemthong)

Member



(Prof. Dr. Santi Maensiri)

Vice Rector for Academic Affairs and
Internationalization



(Asst. Prof. Dr. Worawat Meevasana)

Dean of Institute of Science

มัสติกา พิมพ์สุดตะ : นิกเกิลฟอสไฟด์บนถ่านกัมมันต์ สำหรับปฏิกิริยาไฮโดรดีออกซิเจนชันของน้ำมันปาล์ม (NICKEL PHOSPHIDE ON ACTIVATED CARBON FOR HYDRODEOXYGENATION OF PALM OIL) อาจารย์ที่ปรึกษา : ศาสตราจารย์ ดร.จตุพร วิทยาคูณ, 163 หน้า.

ถ่านกัมมันต์ผลิตจากลำต้นไม้กระถินที่มาจากพื้นที่ใกล้เคียงมหาวิทยาลัยเทคโนโลยีสุรนารี จังหวัดนครราชสีมา โดยขั้นแรกเป็นการผลิตถ่านจากเตาอิวาซากิ (IW) แล้วจึงนำถ่านที่ได้ไปวิเคราะห์สมบัติต่างๆ เทียบกับถ่านที่ผลิตจากเตาเผาแบบท่อในห้องปฏิบัติการ (TF) นอกจากนี้การผลิตถ่านจากเตาอิวาซากิมีผลผลิตพลอยได้ คือน้ำส้มควันไม้ ซึ่งในงานนี้ได้ศึกษาองค์ประกอบเคมีในน้ำส้มควันไม้ที่เก็บ ณ 3 ช่วงอุณหภูมิ และทำการสกัดน้ำส้มควันไม้ด้วยตัวทำละลาย 3 ชนิด องค์ประกอบหลักที่พบคือ กรดอะซิติก รองลงมาคือ เมทิลไซโคลเพนเทน และเฟอร์ฟิวริล แอลกอฮอล์ และตัวอย่างที่เก็บ ณ อุณหภูมิ 140-145°C มีองค์ประกอบอินทรีย์มากที่สุด

ถ่านที่ได้จากเตาอิวาซากิและจากเตาเผาแบบท่อในห้องปฏิบัติการ นำมาผลิตถ่านกัมมันต์ โดยเปรียบเทียบ 2 วิธีคือ การกระตุ้นทางกายภาพด้วยแก๊สคาร์บอนไดออกไซด์ และทางเคมีด้วยสารละลายซิงค์คลอไรด์ โดยศึกษาผลของขนาดอนุภาคถ่านที่จะนำมากระตุ้นเพื่อผลิตถ่านกัมมันต์ โดยแบ่งเป็น 3 ขนาดคือ ใหญ่ กลาง และเล็ก ผลการศึกษาพบว่าถ่านที่มีอนุภาคขนาดกลางให้ถ่านกัมมันต์ที่มีสมบัติทางกายภาพดีที่สุดทั้งแบบกระตุ้นทางกายภาพและเคมี โดยให้พื้นที่ผิวและปริมาณธาตุคาร์บอนสูง และพบว่ากระตุ้นทางกายภาพด้วยแก๊สคาร์บอนไดออกไซด์เป็นวิธีที่เหมาะสม ดังนั้นจึงนำถ่านขนาดกลางมาใช้เพื่อเตรียมถ่านกัมมันต์และกระตุ้นด้วยวิธีทางกายภาพ โดย พร้อมทั้งศึกษาผลของอุณหภูมิที่ใช้ในการเตรียมถ่านกัมมันต์ พบว่าที่อุณหภูมิ 800°C เป็นอุณหภูมิที่เหมาะสมที่สุด

ส่วนถัดไป คือการนำถ่านกัมมันต์ที่มีพื้นที่ผิวสูง มาเป็นตัวรองรับสำหรับโลหะฟอสไฟด์ เพื่อผลิตน้ำมันไบโอไฮโดรเจนเตตริเซล จากปฏิกิริยาไฮโดรดีออกซิเจนชันของน้ำมันปาล์ม แต่ก่อนจะใช้ตัวเร่งนี้ ต้องเลือกโลหะที่เหมาะสมก่อน โดยได้เปรียบเทียบสารประกอบฟอสไฟด์ของนิกเกิล โคบอลต์ และคอปเปอร์ ที่ทดสอบสภาวะการทดลองเดียวกัน ได้ศึกษาสมบัติของตัวเร่งปฏิกิริยาโดยหลายเทคนิค พบว่านิกเกิลฟอสไฟด์มีประสิทธิภาพการเร่งปฏิกิริยาดีที่สุด แต่มีปัญหา คือมีเฟสผสมและมีขนาดผลึกที่มีขนาดใหญ่

เพื่อเพิ่มประสิทธิภาพการเร่งปฏิกิริยา ได้เตรียมนิกเกิลฟอสไฟด์บนถ่านกัมมันต์ (AC) และ SBA-15 โดย AC เป็นวัสดุไมโครพอร์สที่ผลิตจากถ่านไม้กระถินจากเตาอิวาซากิ และจากเตาเผาแบบท่อ และ SBA-15 เป็นวัสดุเมโซพอร์สที่มีรูพรุนที่เป็นระเบียบ หลังจากการเตรียมตัวเร่งปฏิกิริยา

สารประกอบนิกเกิล จะเข้าไปอยู่ในรูพรุนของตัวรองรับ ทำให้พื้นที่ผิวลดลง เมื่อนำไปรีดิวซ์ ตัวเร่งปฏิกิริยาจะมีนิกเกิลในรูป Ni_2P มีการกระจายตัวดีที่สุดในตัวเร่งปฏิกิริยา NiP/AC_IW จากการเร่งปฏิกิริยา HDO ตัวเร่งปฏิกิริยาที่ดีที่สุดคือ NiP/AC_IW อย่างไรก็ตาม หลังการทดสอบ ตัวเร่งปฏิกิริยาทุกตัวมีเฟสผสมระหว่าง Ni_2P และ Ni_{12}P_5



สาขาวิชาเคมี

ลายมือชื่อนักศึกษา มัสดากา นิมพ์สตา:

ปีการศึกษา 2559

ลายมือชื่ออาจารย์ที่ปรึกษา จตุพร อินทกุล

MUSTIKA PIMSUTA : NICKEL PHOSPHIDE ON ACTIVATED
CARBON FOR HYDRODEOXYGENATION OF PALM OIL. THESIS
ADVISOR : PROF. JATUPORN WITTAYAKUN, Ph.D. 163 PP.

ACTIVATED CARBON/HYDRODEOXYGENATION/BIO-HYDROGENATED
DIESEL

Activated carbon was produced from *L. leucocephala* wood obtained from a land near Suranaree University of Technology, Nakhon Ratchasima Province. First, charcoal was produced in an Iwasaki kiln (IW) and analyzed by several techniques and compared with a charcoal produced from a laboratory tube furnace (TF). Besides, by-product from charcoal production was wood vinegar. In this work wood vinegar was collected at three temperature ranges and extracted with three solvents. The main components were acetic acid, methylcyclopentane and furfuryl alcohol. The sample collected at 140-145°C gave the highest amount of organic compounds.

Charcoals from Iwasaki kiln and laboratory tube furnace were used to produce activated carbon by physical activation with carbon dioxide and chemical activation with zinc chloride. The three different particle sizes of charcoals, namely, large, medium and small were studied. The results showed that the medium size charcoal from both activation methods gave activated carbon with high surface area and carbon contents. The suitable activation was physical method with carbon dioxide. Thus, the medium size of charcoal was further used with various activating temperature in physical method. The optimum activating temperature was 800°C.

In the next part, activated carbon was employed as a support for metal phosphides to produce bio-hydrogenated diesel from hydrodeoxygenation (HDO) of palm oil. Prior to that, it was necessary to screen the metal by comparing phosphides of Ni, Co and Cu at the same reaction condition. The catalysts were characterized by several techniques. Nickel phosphide provided the best catalytic activity. The reduced catalyst contained a mixed phase between Ni_2P and Ni_{12}P_5 . After the catalytic testing, the phase was Ni_{12}P_5 dominant.

To enhance the catalytic performance, nickel phosphide was prepared on activated carbons (AC) and SBA-15. ACs were microporous materials produced from two type of charcoals from *L. leucocephala* wood : from Iwasaki kiln (IW) and from tube furnace (TF). SBA-15 was a mesoporous silica with uniform pores. After the catalyst preparation, the support pores were occupied by nickel species leading to the decrease of the surface areas. The reduced catalysts on all supports contained Ni_2P and the best dispersion was obtained in $\text{NiP}/\text{AC_IW}$. From the HDO catalytic testing, $\text{NiP}/\text{AC_IW}$ was the best catalyst. However, after the test, a mixed phase between Ni_2P and Ni_{12}P_5 was observed from all catalysts.

School of Chemistry

Academic Year 2016

Student's Signature มัสตกา มิมพ์สตา

Advisor's Signature อ.พร. ภาณุ

ACKNOWLEDGEMENTS

I would like to thank everybody that helped me throughout my studies. First of all, I would like to thank my advisor, Prof. Dr. Jatuporn Wittayakun, for sharing his knowledge with me, supporting in term of the finance, guiding me and editing my thesis. He taught me not only the subject matter, but also life lessons and this I appreciate very much. His encouragement, understanding and instruction are invaluable and I will treasure it. I am also thankful to the thesis examining committee, including Asst. Prof. Dr. Sanchai Prayoonpokarach, Assoc. Prof. Dr. Nurak Grisadanurak, Dr. Pongtanawat Khemthong and Dr. Supunnee Junpirom for their helpful and valuable comments and suggestions during my thesis defense.

I would like to acknowledge the scholarship, Science Achievement Scholarship of Thailand, (SAST), from the Thai government, Synchrotron Light Research Institute, National Nanotechnology Center (NANOTEC) and Thailand Research Fund (TRF; TRG5780192).

Finally, I would like to thank my family for their enduring love, support and encouragement. I would like to thank all of the friends in my catalysis group, NEC group and my friend at Suranaree University of Technology, Mr. Chanintorn Ruangudomsakul, for their inspiration.

Mustika Pimsuta

CONTENTS

	Page
ABSTRACT IN THAI.....	I
ABSTRACT IN ENGLISH.....	III
ACKNOWLEDGEMENTS.....	V
CONTENTS.....	VI
LIST OF TABLES.....	XII
LIST OF FIGURES.....	XIV
LIST OF SCHEMES.....	XIX
CHAPTER	
I INTRODUCTION.....	1
1.1 Introduction.....	1
1.2 <i>L. leucocephala</i> wood as a raw material for activated carbon.....	2
1.3 Modification of activated carbon from <i>L. leucocephala</i> wood for a catalyst support.....	4
1.4 Bio-hydrogenated diesel (BHD).....	7
1.5 Metal catalysts for bio-hydrogenated diesel.....	12
1.6 References.....	13
II LITERATURE REVIEWS.....	17
2.1 Preparation of wood-based activated carbon.....	17
2.2 Synthesis of siliceous SBA-15.....	21

CONTENTS (Continued)

	Page
2.3 Applications of activated carbon, SBA-15 and metal phosphide catalysts.....	22
2.4 Advantages of bio-hydrogenated diesel (BHD) over fatty acid methyl ester (FAME or biodiesel)	25
2.5 References.....	27
III PRODUCTION OF CHARCOAL AND WOOD VINEGAR BY PYROLYSIS OF <i>L. LEUCOCEPHALA</i> WOOD.....	33
3.1 Abstract.....	33
3.2 Introduction.....	33
3.3 Experimental.....	35
3.3.1 Configuration of Iwasaki kiln.....	35
3.3.2 Pyrolysis process and collection of wood vinegar from Iwasaki kiln.....	36
3.3.3 Preparation of charcoal in a tube furnace.....	37
3.3.4 Characterization of the charcoal.....	38
3.3.5 Extraction and analysis of wood vinegar by using GC-MS.....	39
3.4 Results and discussion.....	41
3.4.1 Composition, morphology and thermal stability of <i>L. leucocephala</i> charcoal.....	41
3.4.2 Chemicals in wood vinegar from <i>L. leucocephala</i> wood.....	48

CONTENTS (Continued)

	Page
3.5 Conclusions.....	58
3.6 References.....	59
IV PREPARATION OF ACTIVATED CARBON FROM CHARCOAL PRODUCED IN IWASAKI KILN AND TUBE FURNACE.....	62
4.1 Abstract.....	62
4.2 Introduction.....	63
4.3 Experimental.....	64
4.3.1 Preparation of activated carbon.....	64
4.3.2 Characterization of the activated carbon.....	66
4.4 Results and discussion.....	68
4.4.1 Characterization of activated carbon from physical activation..	68
4.4.2 Characterization of activated carbon from chemical activation.	75
4.4.3 Characterization of activated carbon by various activation temperature.....	82
4.5 Conclusions.....	90
4.6 References.....	91
V HYDRODEOXYGENATION OF PALM OIL TO BIO- HYDROGENATED DIESEL (BHD) PRODUCT OVER METAL PHOSPHIDES.....	94
5.1 Abstract.....	94

CONTENTS (Continued)

	Page
5.2 Introduction.....	95
5.3 Experimental.....	98
5.3.1 Preparation of metal phosphides for catalysts scanning in HDO reaction.....	98
5.3.2 Catalyst characterization.....	98
5.3.3 Catalytic deoxygenation testing.....	99
5.3.4 Product analysis.....	101
5.4 Results and discussion.....	103
5.4.1 Catalysts appearance after the synthesis, calcination and reduction.....	103
5.4.2 Catalyst morphology from SEM.....	104
5.4.3 Catalysts characterization by XRD.....	106
5.4.4 Catalysts characterization by XANES.....	112
5.4.5 Catalytic hydrotreating of palm oil.....	117
5.4.6 Characterization of spent catalysts.....	124
5.5 Conclusions.....	124
5.6 References.....	125
 VI HYDRODEOXYGENATION OF PALM OIL TO BIO- HYDROGENATED PRODUCT OVER NICKEL PHOSPHIDE SUPPORTED ON ACTIVATED CARBON AND SBA-15.....	 128

CONTENTS (Continued)

	Page
6.1 Abstract.....	128
6.2 Introduction.....	129
6.3 Experimental.....	130
6.3.1 Preparation of activated carbon.....	130
6.3.2 Preparation of NiP/AC by wet impregnation.....	131
6.3.3 Synthesis of siliceous SBA-15.....	132
6.3.4 Preparation of NiP/SBA-15 by wet impregnation.....	132
6.3.5 Catalyst characterization.....	133
6.3.6 Catalytic deoxygenation testing.....	134
6.4 Results and discussion.....	135
6.4.1 Results from characterization and catalytic testing of NiP/AC.....	135
6.4.2 Results from characterization and catalytic testing of NiP/SBA-15.....	144
6.5 Conclusions.....	153
6.6 References.....	153
VII CONCLUSIONS AND RECOMMENDATION.....	156
APPENDICES.....	158
APPENDIX A CALIBRATION CURVES OF STANDARDS.....	159

CONTENTS (Continued)

	Page
APPENDIX B CHROMATOGRAMS OF STANDARDS AND SAMPLES.....	162
CURRICULUM VITAE.....	163



LIST OF TABLES

Table	Page
1.1	Typical compositions of palm oil..... 9
1.2	The important properties of diesel specified, tested in the methods of ASTM D-975-11b and ASTM D-7566-11a..... 12
2.1	Catalysts, conditions and product yield from HDO reaction..... 25
2.2	Comparison of ester-based biodiesel and hydrocarbon-based green diesel (BHD)..... 27
3.1	Results from Nitrogen adsorption-desorption analysis of charcoal from Iwasaki kiln and a tube furnace..... 45
3.2	Elemental analysis of charcoal from Iwasaki kiln and a tube furnace..... 48
3.3	Chemical components of <i>L. leucocephala</i> wood vinegar collected with varied outlet temperature in <i>n</i> -hexane phase detected by GC-MS analysis..... 52
3.4	Chemical components of <i>L. leucocephala</i> wood vinegar collected with varied outlet temperature in diethyl ether phase detected by GC-MS analysis..... 55
3.5	Chemical components of <i>L. leucocephala</i> wood vinegar collected with varied outlet temperature in ethyl acetate phase detected by GC-MS analysis..... 57
4.1	Elemental analysis of charcoal and activated carbon by physical activation at 800°C, 1 h..... 70

LIST OF TABLES (Continued)

Table	Page
4.2	Nitrogen adsorption-desorption analysis of charcoal and activated carbon..... 72
4.3	Elemental analysis of activated carbon produced by chemical activation at 800°C for 1 h..... 78
4.4	Nitrogen adsorption-desorption analysis of activated carbon..... 80
4.5	The elemental composition of activated carbon..... 87
4.6	Adsorption analysis of charcoal and activated carbon by physical activation..... 88
5.1	Operating condition for GC-TCD..... 102
5.2	Edge position of nickel sample and standards..... 113
5.3	Edge position of cobalt sample and standards..... 114
5.4	Edge position of copper sample and standards..... 115
5.5	The physical properties of BHD product..... 123
6.1	Nitrogen adsorption-desorption analysis of activated carbon and NiP/AC catalysts..... 140
6.2	The physical properties of BHD product..... 152

LIST OF FIGURES

Figure		Page
1.1	Structure of (a) cellulose, (b) hemicellulose and (c) lignin.....	3
1.2	Surface functional groups on carbon.....	6
1.3	Proposed deoxygenation pathways.....	8
1.4	The possible reaction pathways during hydroprocessing of some triglyceride.....	11
3.1	Iwasaki kiln from Energy Ashram: Appropriate Technology Association, Nakhon Ratchasima, Thailand.....	35
3.2	Iwasaki kiln and pyrolysis process.....	37
3.3	A horizontal tube furnace for preparation of charcoal.....	38
3.4	Scheme of extraction of <i>L. leucocephala</i> wood vinegar.....	40
3.5	SEM images of (a, b) wood, (c, d) charcoal, (e) SEM-EDX of charcoal form <i>L. leucocephala</i> wood.....	42
3.6	XRD patterns of <i>L. leucocephala</i> charcoal from Iwasaki kiln and a tube furnace.....	43
3.7	Nitrogen adsorption-desorption isotherm of charcoal from Iwasaki kiln and a tube furnace.....	44
3.8	FTIR spectra of charcoal from Iwasaki kiln and tube furnace.....	46
3.9	TGA results of (a) wood, (b) charcoal from an Iwasaki kiln and a tube furnace.....	47

LIST OF FIGURE (Continued)

Figure	Page
3.10	Appearance of wood vinegar at various collecting temperatures and wood vinegar yield (%) and pH..... 49
3.11	The relative content of organic compositions at various collecting temperatures..... 50
3.12	Extraction ability of different extraction solvents on main components in wood vinegar..... 51
4.1	Equipment setup for activation in a horizontal tube furnace..... 65
4.2	SEM images of charcoal and activated carbons with different sizes preparation by physical activation (CO ₂) at 800°C for 1 h..... 68
4.3	XRD patterns of activated carbon by physical activation with different sizes from <i>L. leucocephala</i> charcoal..... 69
4.4	Adsorption-desorption isotherms, pore size distributions of charcoal and activated carbons..... 71
4.5	FTIR spectra of charcoal and activated carbons of physical method..... 74
4.6	Raman spectra of activated carbon..... 75
4.7	SEM images of charcoal and activated carbons with different sizes preparation by chemical activation (ZnCl ₂) at 800°C for 1 h..... 76
4.8	XRD patterns of charcoal and activated carbon by chemical activation..... 77
4.9	Nitrogen adsorption-desorption isotherms and pore size distributions of charcoal and activated carbons..... 79

LIST OF FIGURE (Continued)

Figure	Page
4.10	FTIR spectra of charcoal and activated carbons of chemical method..... 81
4.11	Raman spectra of activated carbon..... 82
4.12	XRD patterns of activated carbon with charcoal from, (a) Iwasaki kiln and (b) tube furnace with various activating temperature for 1h.....83
4.13	SEM images of (a) charcoal, (b to d) activated carbon, (e, f) its EDX composition, (g, h) TEM images of AC800IW.....85
4.14	SEM images of (a) charcoal (from a tube furnace), (b - d) activated carbon.....86
4.15	Adsorption isotherms of (a) activated carbon from charcoal in Iwasaki kiln and (b) charcoal in a tube furnace.....89
5.1	Hydrotreating reactor setup..... 100
5.2	Apparatus of Karl Fischer titrator.....103
5.3	Appearance of catalysts after drying, calcination and reduction of nickel, cobalt and copper.....104
5.4	SEM images of reduced nickel catalyst before testing in HDO reaction....105
5.5	SEM images of reduced cobalt catalyst before testing in HDO reaction....105
5.6	SEM images of (a) reduced-copper catalyst without SiO ₂ and (b) reduced-copper catalyst with SiO ₂ before testing in HDO reaction.....105
5.7	XRD patterns of as-synthesized, calcined and reduced nickel catalyst, and structure of Ni ₂ P generated from ICSD program.....107

LIST OF FIGURE (Continued)

Figure	Page
5.8	XRD patterns of as-synthesized-, calcined- and reduced-cobalt catalysts and structure of Co_2P generated from ICSD program.....109
5.9	XRD patterns of as-synthesized-, calcined- and reduced-copper catalysts and structure of Cu_3P generated from ICSD program.....111
5.10	XANES spectrum of nickel catalysts and standards..... 112
5.11	XANES spectrum of cobalt catalysts and standards..... 114
5.12	XANES spectrum of copper catalysts.....115
5.13	XRD patterns of commercial Ni_2P catalyst at before and after HDO reaction of palm oil.....116
5.14	SEM images of commercial nickel phosphide catalyst before testing in HDO reaction.....117
5.15	Conversion and selectivity and product yield and competitive reaction of sample screening by varying the temperature.....118
5.16	Appearance BHD product of screening samples (a) Ni_xP_y , (b) Co_2P , (c) Cu_3P ; at 300, 350 and 400°C, hydrogen pressure 50 bar..... 120
5.17	Conversion, product yield and competitive reaction, selectivity, gas product of palm oil tested at 380°C, hydrogen pressure of 50 bar, product collecting time of 0-9 h and LHSV of 1 h^{-1}121
5.18	Appearance BHD product of screening samples (a) Ni_xP_y , (b) commercial Ni_2P at 380°C and hydrogen pressure 50 bar.....123

LIST OF FIGURE (Continued)

Figure	Page
6.1	Equipment setup for activation in a horizontal tube furnace.....131
6.2	SEM images and TEM image of NiP/AC_IW; SEM images and TEM image of NiP/AC_TF.....136
6.3	XRD patterns of (a) NiP/AC_IW, (b) NiP/AC_TF.....138
6.4	Adsorption-desorption isotherms and pore size distributions of nickel catalyst.....139
6.5	Conversion, product yield, selectivity of C ₁₅ to C ₁₈ and competitive reaction, selectivity, gas product distribution of NiP/AC_IW and NiP/AC_TF catalysts.....142
6.6	SEM images of SBA-15 and reduced NiP/SBA-15 ; TEM images of SBA-15, reduced NiP/SBA-15 and spent NiP/SBA-15..... 145
6.7	XRD patterns of NiP/SBA-15 at low angle range, SBA-15, fresh- and spent- NiP/SBA-15 at broad angle range catalysts.....147
6.8	Nitrogen adsorption-desorption isotherms and pore size distribution of unloaded SBA-15 and NiP/SBA-15.....149
6.9	Conversion, product yield, selectivity of C ₁₅ to C ₁₈ and competitive reaction and gas product distribution of NiP/SBA-15 catalysts.....151
6.10	BHD product from (a) NiP/AC_IW, (b) NiP/AC_TF, (c) NiP/SBA-15 catalysts..... 152

LIST OF SCHEMES

Scheme	Page
5.1 Proposed pathways to convert palm oil to bio-hydrogenated diesel (BHD) via deoxygenation.....	97



CHAPTER I

INTRODUCTION

1.1 Introduction

Leucaena leucocephala (Lam.) de Wit wood (*L. leucocephala*) or Lead tree is abundant in Thailand, especially in Nakhon Ratchasima province. The fast growing rate of *L. leucocephala* inhibit the growth of economic plants and make it undesirable. Thailand is an agriculture country where spaces are needed for growing of economic plants such as cassava, sugar cane, corn, vegetable, rice, palm oil, and rubber tree. Thus, the *L. leucocephala* can be considered a problem.

Normally, fresh parts of *L. leucocephala* including young leaf, flower buds, and young pod are edible. However, the wood is not much used. Orwa et al. (2009) reported that the wood of *L. leucocephala* is an excellent firewood species with a specific gravity of 0.45-0.55 and the wood burns steadily with little smoke, few spark and produces less than 1% ash.

L. leucocephala is a source to produce charcoal in some countries. To increase the value of the charcoal, it can be further used to produce activated carbon. Jambulingam et al. (2007) prepared the activated carbon by *L. leucocephala* shell with chemical method with various agents including $ZnCl_2$, $CaCl_2$, Na_2SO_4 , and Na_2CO_3 . The best activated carbon was obtained from the process with $ZnCl_2$. Their results were consistent with the fact that $ZnCl_2$ was widely used as an activating agent in the preparation of activated carbon (Hayashi et al., 2002).

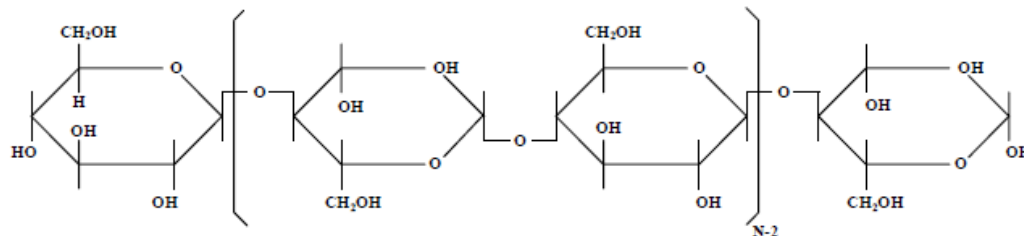
Activated carbon is widely used as an adsorbent and support for metal catalyst. It can be produced from a variety of carbonaceous source materials by chemical and physical methods. Several researchers have studied the preparation of activated carbons from agricultural wastes such as pistachio-nut shells (Lua et al., 2004), walnut shell (Zabihi et al., 2009), plant wastes (Açıkyıldız et al., 2014), eucalyptus and wattle wood (Ngernyen et al., 2006). Ozdemir et al. (2014) prepared low-cost activated carbon from grape stalk by chemical activation with $ZnCl_2$ in carbon dioxide (CO_2) atmosphere. They varied conditions including carbonization temperature, activation time, impregnation time and impregnation ratios. The optimum condition to prepare the activated carbon with the highest surface area was as follows: carbonization temperature of $700^\circ C$, carbonization time of 120 min, impregnation time of 36 h and $ZnCl_2$ /grape stalk ratio of 2.

Up to date, there are not many studies on the applications of activated carbon from *L. leucocephala* wood. Thus, a motivation of this study is to employ it as a catalyst support.

1.2 *L. leucocephala* wood as a raw material for activated carbon

L. leucocephala composes of cellulose (40.8%), hemicellulose (15.9%) and lignin (26.9%) (Antal et al., 2000). The high amount of cellulose makes it suitable as a raw material to convert to charcoal and activated carbon. Figure 1.1 shows molecular structure of cellulose, hemicellulose and lignin.

(a) Cellulose



(b) Hemicellulose

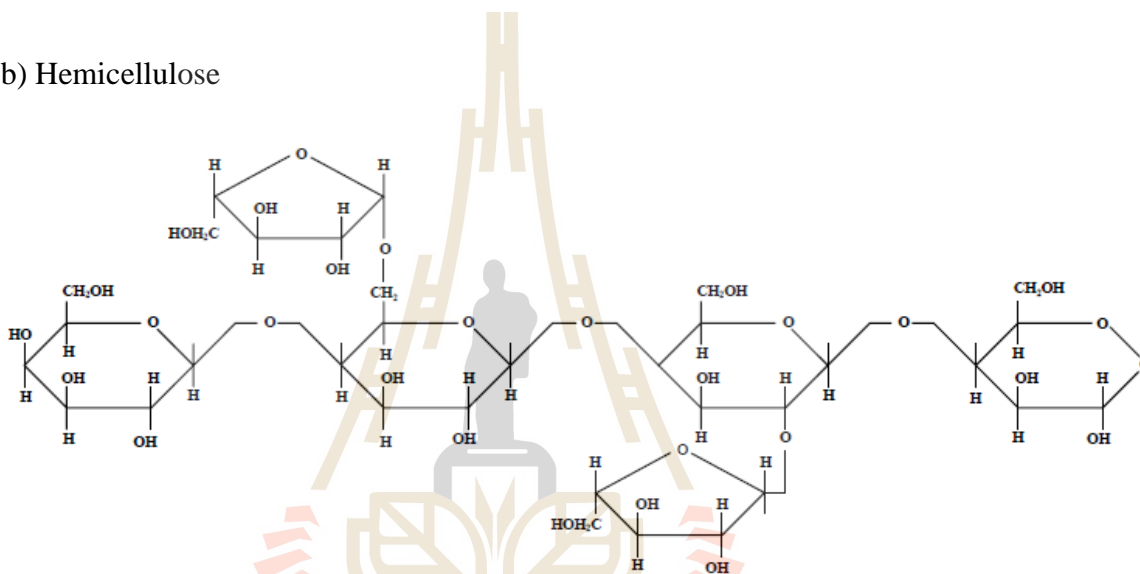


Figure 1.1 Structure of (a) cellulose, (b) hemicellulose (Jagtoyen and Derbyshire, 1998).

(c) Lignin

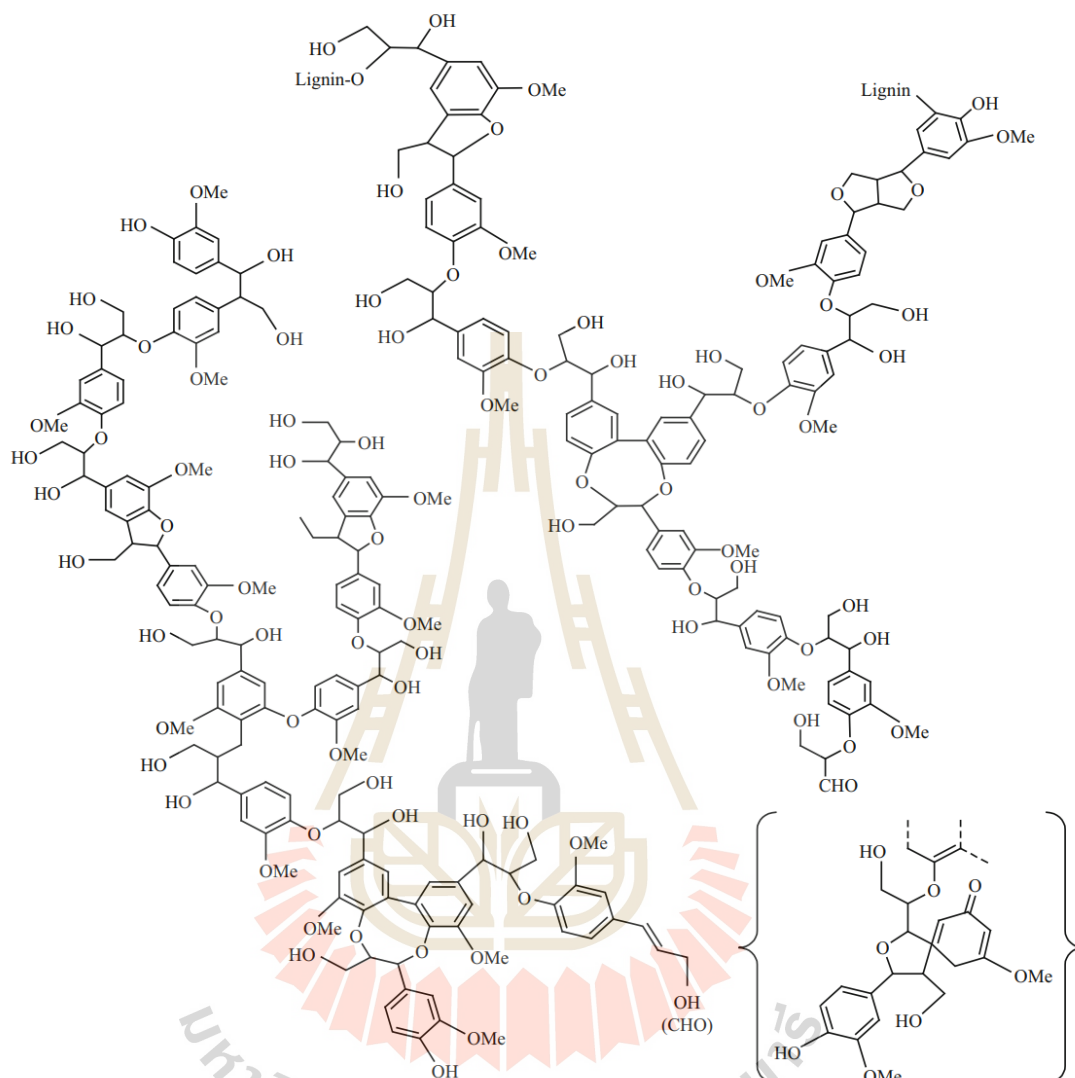


Figure 1.1 (Continued) (c) Lignin (Chen, 2014).

1.3 Modification of activated carbon from *L. leucocephala* wood for a catalyst support

Activated carbon is a carbonaceous solid material with a black color. It is an amorphous solid with a large surface area from the presence of microspores (width < 2 nm). Its specific volume of mesopores (width 2-50 nm) is less than 0.2 cm³/g

(Jambulingam et al., 2007; Phooratsamee et al., 2014). Normally, activated carbon with high surface area was obtained by either chemical activation with $ZnCl_2$ or physical activation with CO_2 (Ozdemir et al., 2014; Ngernyen et al., 2007). In addition, surface of activated carbons has both hydrophilic and hydrophobic functional groups that are specific for some compounds. For examples, organic compounds adsorb mainly on the hydrophobic graphene layer while polar species and heavy metal ions adsorb selectively on hydrophilic functional groups. Therefore, modification of the surface of activated carbon is important, especially, for catalysis purpose.

Generally, activated carbon was used as an adsorbent, a catalyst support for an active phase, or even as a catalyst (Shen, 2015). The surface functional groups are shown in Figure 1.2. The acidic oxygen functional groups are carboxyl, lactone and phenol while basic characters are carbonyl, ether and chromene (Moreno-Castilla et al., 2000). The surface functional groups on activated carbon were important to prepare metal catalysts in hydrodeoxygenation reaction (HDO) of palm oil to produce bio-hydrogenated diesel (BHD).

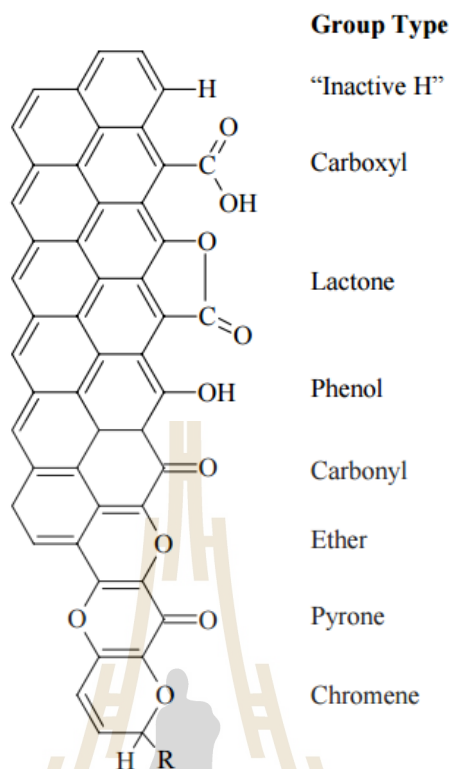


Figure 1.2 Surface functional groups on carbon (Leon y Leon and Radovic, 1994).

Ruiz et al. (2012) prepared MoS₂ supported on the activated carbon with different porosity and functional group of oxygen, and then tested in HDO reaction of guaiacol. The reaction was studied in a batch reactor at 300°C and 5 MPa of hydrogen. The result showed the porosity did not affect the kinetics or selectivity of guaiacol via HDO but the surface functional group has effect for dispersion of Mo sulfide species. High concentration of surface oxygen showed lower catalyst dispersion and lower HDO activity. As a catalyst support, surface functional groups of oxygen (mainly carboxylic, quinonic and lactonic groups) on activated carbon did not help dispersion of metal catalysts.

Activated carbon is an interesting choice for supporting materials in HDO reaction because it has both acidic hydrophilic surface and basic hydrophobic surface that

depended on the preparation method. The acidic nature facilitates hydrogenation and cleavage $C_{(sp^2)}-O$ bond and deoxygenation while the basic nature helps to reduce coke formation (Arun et al., 2015).

In addition, siliceous Santa Barbara Amorphous (SBA-15) is an interesting choice for HDO reaction because of the suitable properties as a support. SBA-15 is a mesoporous silica sieve based on uniform hexagonal pores (in range 4-30 nm) with a narrow pore size distribution, high thermal stability and high surface area (from 400 to above 1000 m^2/g) which helped dispersion of active phase (Soni et al., 2013; Huirache-Acuña et al., 2013; Thielemann et al., 2011).

1.4 Bio-hydrogenated diesel (BHD)

Bio-hydrogenated diesel (BHD) is a straight chain hydrocarbon that was produced via decarboxylation (DCO_2), decarbonylation (DCO) and hydrodeoxygenation (HDO). These reactions removed oxygenated part from a molecule, in the form of carbon dioxide (CO_2), carbon monoxide (CO) and water, respectively. The reaction pathways are shown in Figure 1.3. All reactions improved the properties of biodiesel from high oxygen content, high viscosity and low heating value to high thermal and oxidation stability.

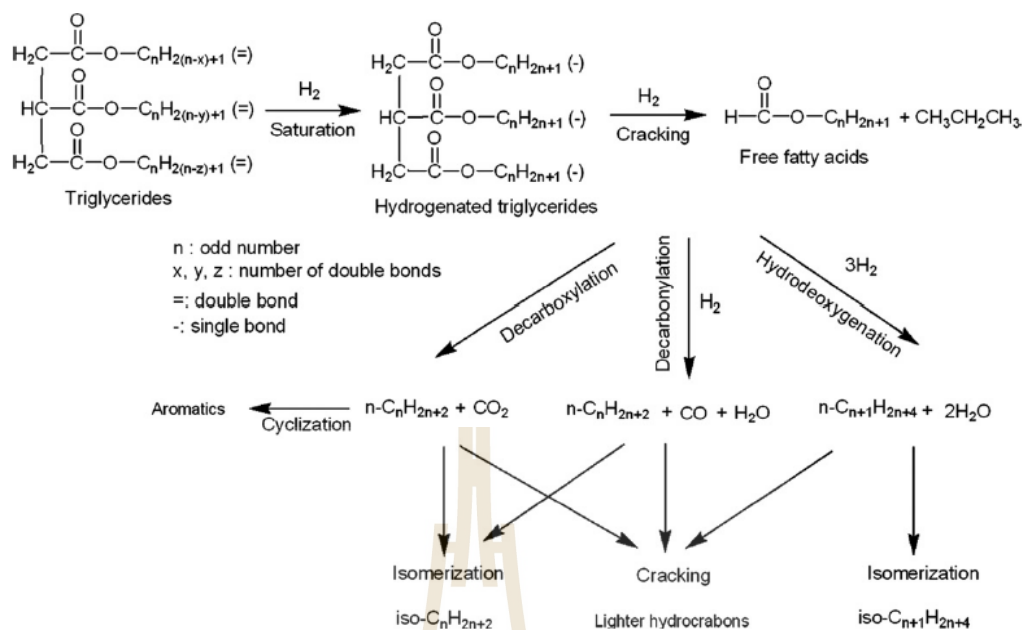


Figure 1.3 Proposed deoxygenation pathways (Veriansyah et al., 2012).

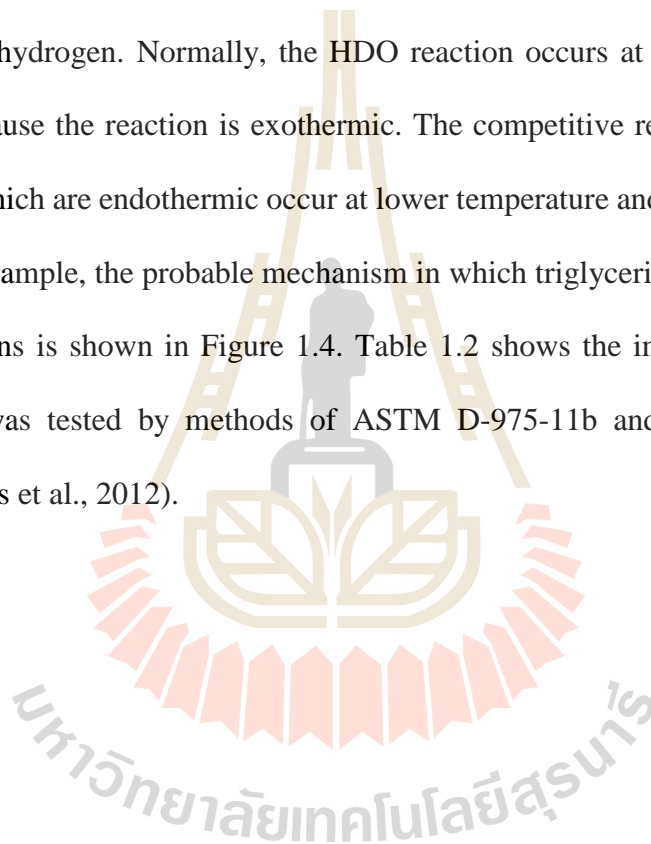
The deoxygenation started from hydrogenation of triglycerides which are long chains fatty acid ester including saturated and unsaturated acids. The properties of triglycerides depend on the composition of raw materials. In this work, the triglycerides typically composed of C₁₄-C₁₈ that are the composition of palm oil as shown in Table 1.1 (Sotelo-Boyás et al., 2012).

Table 1.1 Typical compositions of palm oil, modified from literature Sotelo-Boyás et al. (2012).

Normal source	Structure	Molecular formula	Molecular weight (MW)		Typical composition wt. %
			Fatty acid	Triglyceride	Palm oil
Capric	C10:0	C ₁₀ H ₂₀ O ₂	172.3	554.8	0.0
Lauric	C12:0	C ₁₂ H ₂₄ O ₂	200.3	639.0	0.0
Myristic	C14:0	C ₁₄ H ₂₈ O ₂	228.4	723.2	2.5
Palmitic	C16:0	C ₁₆ H ₃₂ O ₂	256.4	807.3	40.8
Palmitoleic	C16:1	C ₁₆ H ₃₀ O ₂	254.4	801.3	0.0
Stearic	C18:0	C ₁₈ H ₃₆ O ₂	284.5	891.5	3.6
Oleic	C18:1	C ₁₈ H ₃₄ O ₂	282.5	885.4	45.2
Linoleic	C18:2	C ₁₈ H ₃₂ O ₂	280.4	879.4	7.9
Linolenic	C18:3	C ₁₈ H ₃₀ O ₂	278.4	873.3	0.0
Arachidic	C20:0	C ₂₀ H ₄₀ O ₂	312.5	975.6	0.0
Eicosenoic	C20:1	C ₂₀ H ₃₈ O ₂	310.5	969.6	0.0
Behenic	C22:0	C ₂₂ H ₄₄ O ₂	340.6	1059.8	0.0
Erucic	C22:1	C ₂₂ H ₄₂ O ₂	338.6	1053.8	0.0
Estimated MW					847.0

After hydrogenation of triglycerides, hydrogenolysis occurred and free fatty acids and propane were produced as a primary product. In decarboxylation, oxygen is removed in the form of CO₂. In decarbonylation, the oxygen is removed in the form of carbon monoxide (CO) and water. In the both cases, one carbon atom is removed from

free fatty acids. This work focuses on the HDO reaction. In hydrodeoxygenation, the oxygen is eliminated in the form of water. This reaction produces straight-chain alkane with the same number of carbon corresponding to fatty acids bound to triglyceride by using acidic support and non-support catalysts. A serious problem for acid catalyst during the reaction is deactivation by coking. These routes cannot be easily occurred; they depend on the experimental conditions and surface reaction on the catalysts to CO_2 , CO or hydrogen. Normally, the HDO reaction occurs at high temperature and pressure because the reaction is exothermic. The competitive reactions such as DCO and DCO_2 which are endothermic occur at lower temperature and pressure (Srifa et al., 2014). For example, the probable mechanism in which triglycerides are converted into linear paraffins is shown in Figure 1.4. Table 1.2 shows the important properties of diesel that was tested by methods of ASTM D-975-11b and ASTM D-7566-11a (Sotelo-Boyás et al., 2012).



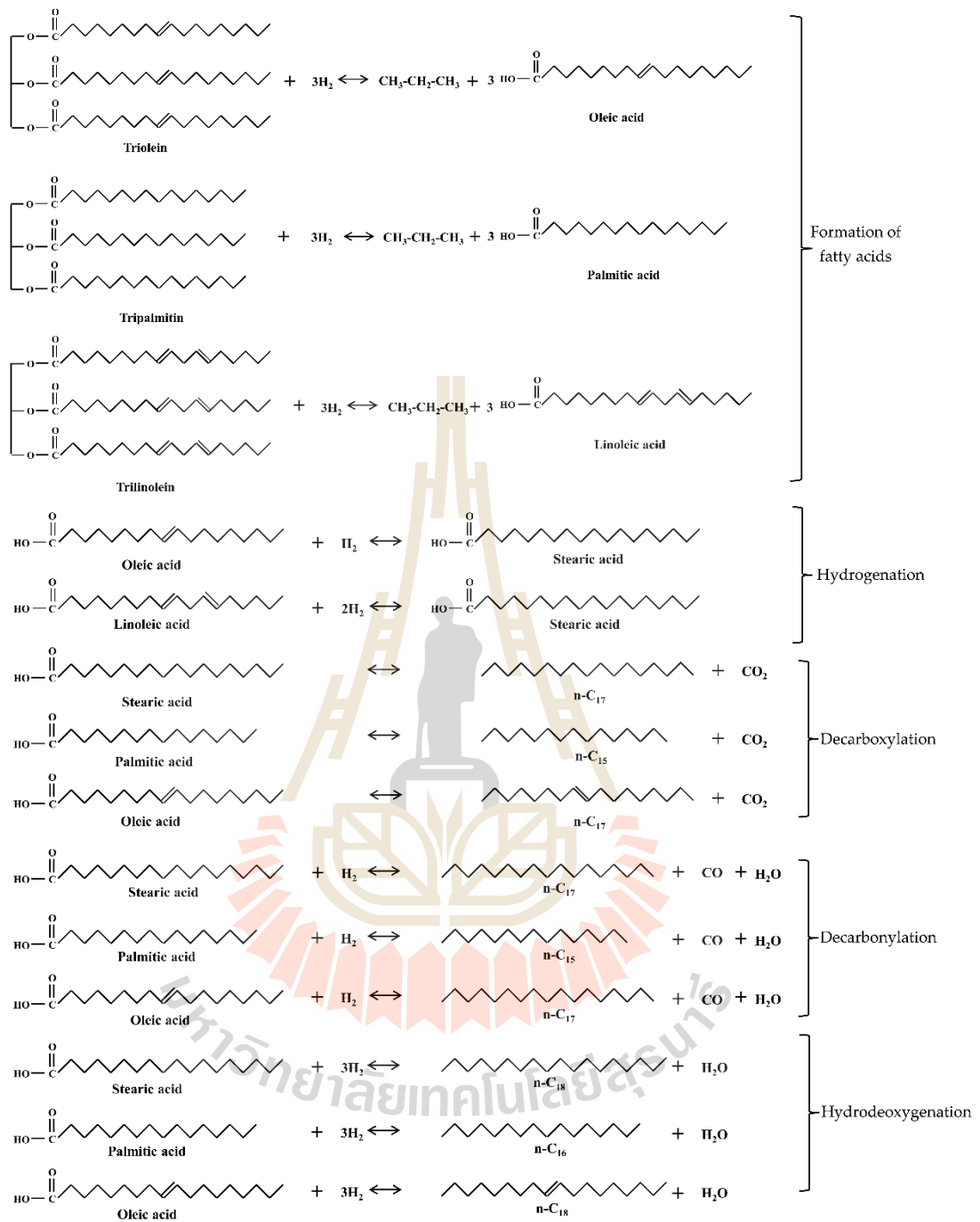


Figure 1.4 The possible reaction pathways during hydroprocessing of some triglyceride adapted from literature Guzman et al. (2010).

Table 1.2 The important properties of diesel specified, tested in the methods of ASTM D-975-11b and ASTM D-7566-11a from literature Sotelo-Boyás et al. (2012).

Property	Value	Test method	
		ASTM	EN
Flash point (°C)	38 (Min.)	D93	2719
Kinematic viscosity (mm ² /s) @ 40°C	1.9 (Min.) 4.1 (Max.)	D445	3104
Ash (wt.%)	0.01 (Max.)	D482	6245
Cetane number	40 (Min.)	D613	5165
Cloud point (°C)	Report	D2500	ISO 3015

1.5 Metal catalysts for bio-hydrogenated diesel

Elkasabi et al. (2014) used the metals of Pt, Ru, or Pd on carbon support for HDO reaction. They found that Pt/C was the best performance in terms of hydrogen consumption and deoxygenation efficiency. Noble metals and sulfide catalysts showed high selectivity and activity for HDO reaction and high cetane number. However, high cost of noble metal catalysts and sulfur-contamination from the sulfide catalysts in the end of product were the major disadvantages (Mohammad et al., 2013).

Ryymin et al. (2010) used the catalyst of sulphide NiMo/ γ -Al₂O₃ for the HDO reaction of phenol and methyl heptanoate. The result showed low heptanoic acid and methanol products. After the reaction, sulfur was contained in product of 5.6 wt.%. Thus, developing low cost Ni-based non-sulfide catalysts is an interesting choice. The utilization of metal phosphide catalysts

received more attention according to the possibility to derive triglyceride into the biofuel by their acid properties which could lead to high activity and selectivity for hydroprocessing.

Finally, to compare properties of support such as high surface area, acidic support and high thermal stability of activated carbon and SBA-15 were used as support for nickel phosphide catalyst in HDO reaction.

1.6 References

- Antal, M. J., Allen, S. G., Dai, X., Shimizu, B., Tam, M. S., and Grønli, M. (2000). Attainment of the theoretical yield of carbon from biomass. **Industrial and Engineering Chemistry Research**. 39: 4024-4031.
- Arun, N., Sharma, R. V., and Dalai, A. K. (2015). Green diesel synthesis by hydrodeoxygenation of bio-based feedstocks: Strategies for catalyst design and development. **Renewable and Sustainable Energy Reviews**. 48: 240-255.
- Açıkyıldız, M., Gürses, A., and Karaca, S. (2014). Preparation and characterization of activated carbon from plant wastes with chemical activation. **Microporous and Mesoporous Materials**. 198: 45-49.
- Chen, H. (2014). Chemical composition and structure of natural lignocellulose. **Biotechnology of Lignocellulose**. Springer Netherlands. 25-71.
- Elkasabi, Y., Mullen, C. A., Pighinelli, A. L. M. T., and Boateng, A. A. (2014). Hydrodeoxygenation of fast-pyrolysis bio-oils from various feedstocks using carbon-supported catalysts. **Fuel Processing Technology**. 123: 11-18.
- Guzman, A., Torres, J. E., Prada, L. P., and Nunez, M. L. (2010). Hydroprocessing of crude palm oil at pilot plant scale. **Catalysis Today**. 156(1-2): 38-43.

- Hayashi, J., Horikawa, T., Takeda, I., Muroyama, K., and Ani, F. N. (2002). Preparing activated carbon from various nutshells by chemical activation with K_2CO_3 . **Carbon**. 40: 2381-2386.
- Huirache-Acuña, R., Nava, R., Peza-Ledesma, C. L., Lara-Romero, J., Alonso-Núñez, G., Pawelec, B., and Rivera-Muñoz, E. M. (2013). SBA-15 mesoporous silica as catalytic support for hydrodesulfurization catalysts. **Materials**. 6(9): 4139-4167.
- Jagtoyen, M. and Derbyshire, F. (1998). Activated carbons from yellow poplar and white oak by H_3PO_4 activation. **Carbon**. 36: 1085-1097.
- Jambulingam, M., Karthikeyan, S., Sivakumar, P., Kiruthika, J., and Maiyalagan, T. (2007). Characteristic studies of some activated carbons from agricultural wastes. **Journal of Scientific and Industrial Research**. 66: 495-500.
- Leon y Leon, C. A. and Radovic, L. R. (1994). Interfacial chemistry and electrochemistry of carbon surfaces. **Chemistry and Physics of Carbon**. 24: 213-310.
- Lua, A. C., Yang, T., and Guo, J. (2004). Effects of pyrolysis conditions on the properties of activated carbons prepared from pistachio-nut shells. **Journal of Analytical and Applied Pyrolysis**. 72: 279-287.
- Moreno-Castilla, C., López-Ramón, M. V., and Carrasco-Marín, F. (2000). Changes in surface chemistry of activated carbon by wet oxidation. **Carbon**. 38(14): 1995.
- Ngernyen, Y., Tangsathitkulchai, C., and Tangsathitkulchai, M. (2006). Porous properties of activated carbon produced from Eucalyptus and wattle wood by carbon dioxide activation. **Korean Journal of Chemical Engineering**. 23(6): 1046-1054.

- Ngernyen, Y., Tangsathitkulchai, C., Khaoyin, S., Intasa-ard, W., and Tangsathitkulchai, M. (2007). Effect of surface functional groups on water vapor adsorption of eucalyptus wood-based activated carbon. **Suranaree Journal of Science and Technology**. 66: 495-500.
- Orwa, C., Mutua, A., Kindt, R., Jasnadass, R., and Simons, A. (2009). Agroforestry Database: a tree reference and selection guide version 4.0.
- Ozdemir, I., Şahin, M., Orhan, R., and Erdem, M. (2014). Preparation and characterization of activated carbon from grape stalk by zinc chloride activation. **Fuel Processing Technology**. 125: 200-206.
- Phooratsamee, W., Hussaro, K., Teekasap, S., and Hirunlabh, J. (2014). Increasing adsorption of activated carbon from palm oil shell for adsorb H₂S from biogas production by impregnation. **American Journal of Environmental Sciences**. 10(5): 431-445.
- Ryymin, E-M., Honkela, M. L., Viljava, T-R., and Krause, A. O. I. (2010). Competitive reactions and mechanisms in the simultaneous HDO of phenol and methyl heptanoate over sulphide NiMo/γ-Al₂O₃. **Applied Catalysis A: General**. 389: 114-121.
- Ruiz, P. E., Frederick, B. G., De Sisto, W. J., Austin, R. N., Radovic, L. R., Leiva, K., García, R., Escalona, N., and Wheeler, M. C. (2012). Guaiacol hydrodeoxygenation on MoS₂ catalysts: Influence of activated carbon supports. **Catalysis Communications**. 27: 44-48.
- Shen, Y. (2015). Chars as carbonaceous adsorbents/ catalysts for tar elimination during biomass pyrolysis or gasification. **Renewable and Sustainable Energy Reviews**. 43: 281-295.

- Soni, K. K., Boahene, P. E., Rambabu, N., Dalai, A. K., and Adjaye, J. (2013). Hydrotreating of coker light gas oil on SBA-15 supported nickel phosphide catalysts. **Catalysis Today**. 207: 119-126.
- Sotelo-Boyás, R., Trejo-Zárraga, F., and de Jesús Hernández-Loyo, F. (2012). Hydroconversion of triglycerides into green liquid fuels. In Hydrogenation. **InTech**. 187-214.
- Srifa, A., Faungnawakij, K., Itthibenchapong, V., Viriya-empikul, N., Charinpanitkul, T., and Assabumrungrat, S. (2014). Production of bio-hydrogenated diesel by catalytic hydrotreating of palm oil over NiMoS₂/γ-Al₂O₃ catalyst. **Bioresource Technology**. 158: 81-90.
- Srifa, A., Faungnawakij, K., Itthibenchapong, V., and Assabumrungrat, S. (2015). Roles of monometallic catalysts in hydrodeoxygenation of palm oil to green diesel. **Chemical Engineering Journal**. 278: 249-258.
- Thielemann, J. P., Girgsdies, F., Schlögl, R., and Hess, C. (2011). Pore structure and surface area of silica SBA-15: influence of washing and scale-up. **Beilstein Journal of Nanotechnology**. 2: 110.
- Veriansyah, B., Han, J. Y., Kim, S. K., Hong, S. A., Kim, Y. J., and Lim, J. S. (2012). Production of renewable diesel by hydroprocessing of soybean oil: effect of catalysts. **Fuel**. 94: 578-585.
- Zhabihi, M., Ahmadpour, A., and Haghghi Asl, A. (2009). Removal of mercury from water by carbonaceous sorbents derived from walnut shell. **Journal of Hazardous Materials**. 167: 230-236.

CHAPTER II

LITERATURE REVIEW

This chapter gives a review on the preparations of wood-based activated carbons and synthesis SBA-15. Applications of activated carbon, SBA-15 and metal phosphide catalysts were tested in hydrodeoxygenation (HDO) of palm oil to bio-hydrogenated diesel (BHD) product. Finally, advantages of BHD over fatty acid methyl ester (FAME or biodiesel) that produced over transesterification.

2.1 Preparation of wood-based activated carbon

Activated carbon is an amorphous solid with a large surface area and pore volume. It can be produced from various carbonaceous materials such as pistachio-nut shells (Lua et al., 2004), walnut shell (Zabihi et al., 2009), *Feronia limonia* (apple wood) shell and plant wastes (Açıkyıldız, et al., 2014), eucalyptus (Ngernyen et al., 2006), grape stalk (Ozdemir et al., 2014), Tamarind (Sahu et al., 2010), walnut and poplar (Heibati et al., 2015) and Lead tree (Mahmoud et al., 2014; Hou et al., 2015). Morphology and porosity of activated carbon were depended on the types of raw materials and activation conditions.

Activated carbon can be produced by chemical activation and physical activation. The chemical activation employed chemicals which have to be washed out and generated waste.

2.1.1 Physical activation

Physical activation is a process to produce activated carbon from raw materials at the high temperature (800-1100°C) (Phooratsamee et al., 2014). There are two methods: one-step procedure and two-step procedure involves the carbonization in an inert atmosphere and activation by using carbon dioxide, air, or steam. In carbon dioxide activation, the gas was dispersed through graphite layer and interacted with the interior layer's functional group and external surface area during the reaction. The moisture and volatile organic compounds were eliminated by inert gas. After reaction, the pores were generated.

Lua et al. (2004) prepared activated carbon from pistachio-nut shells with carbon dioxide by varying factors such as temperature (250-1000°C), hold time (1-3 h), heating rate (5-40°C/min) and nitrogen flow rate (150 ml/min). They found that the optimum activation conditions were temperature of 500°C, an activation holds time of 2 h, a heating rate of 10°C/min, a flow rate of carbon dioxide of 100 ml/min and a nitrogen flow rate of 150 ml/min. From these activation conditions, they obtained the maximum BET surface area of 778 m²/g and total pore volume of 0.466 cm³/g. When increasing the temperature, the product yield decreased.

Ngernyen et al. (2006) prepared activated carbon from eucalyptus and wattle wood by activation with carbon dioxide, varying activation temperature from 600 to 900°C and activation time from 60 to 300 min. Moreover, they studied the effect of carbon dioxide concentration during activation that led to increase BET surface area, micropore volume and total pore volume. The optimum activation conditions of eucalyptus wood were temperature of 900°C for 60 min that gave maximum BET surface area and total pore volume of 1491 m²/g and 0.80 cm³/g, respectively. From

wattle wood, the maximum BET surface area of 1032 m²/g and total pore volume of 0.56 cm³/g was obtained at 800°C for 300 min. The advantage for this method was high BET surface area and high purity.

2.1.2 Chemical activation

Chemical activation is a process to produce activated carbon involving impregnation of chemicals such as ZnCl₂, NaOH, HNO₃, KI, Na₂CO₃, K₂CO₃ and followed by pyrolysis at 500-800°C (Nasri et al., 2014). In chemical procedure, metal oxide diffused and interacted between graphite layers to form a new linkage structure. When the temperature was raised, the thermal expansion was increased depending on the molecular length of the chemicals to d-spacing of the graphite layers (0.33 nm). The volatile organic compounds and some carbonaceous components were eliminated. Pores were generated during the activation.

Chemical activation can be carried out by impregnation of charcoal with zinc chloride (ZnCl₂). During activation, the volume of micropores developed as similar to volume of ZnCl₂ introduced into the particles. The microporosity was uniform and ZnCl₂ acts at temperature lower than 500°C. The porosity was generated due to the space left by ZnCl₂ after washing (Marsh and Rodríguez-Reinoso, 2006).

The advantages of chemical activation were low energy cost, short activating time, and high product yield when compared with physical activation. The most widely used activating agent was ZnCl₂. The process began with impregnation of a raw material with the activating reagent and heated in the inert atmosphere (500-700°C). On the other hand, physical activation by non-toxic gas such as carbon dioxide was more environmental friendly. Thus, many researchers studied the preparation of activated

carbon by chemical activation. Chemical reagent for activation such as ZnCl_2 was the most widely used in the preparation of activated carbon (Hayashi et al., 2002).

Jambulingam et al. (2007) prepared the activated carbon from *L. leucocephala* shell by a chemical method using ZnCl_2 , CaCl_2 , Na_2SO_4 and Na_2CO_3 as chemical precursors at 800°C for 60 min. The optimum activation was ZnCl_2 process that showed high surface area of $1320 \text{ m}^2/\text{g}$.

Ozdemir et al. (2014) prepared a low cost activated carbon from grape stalk by ZnCl_2 process. They studied the effect of carbonization temperature ($500\text{-}700^\circ\text{C}$) and time (30-120 min), impregnation time (24-48 h) and impregnation ratio (1-3). The optimum conditions producing the highest surface area were activation temperature of 700°C , activation time of 120 min, impregnation time of 36 h and ZnCl_2 / grape stalk of 2. The result showed high BET surface area and total pore volume of $1411 \text{ m}^2/\text{g}$ and $0.723 \text{ cm}^3/\text{g}$, respectively.

Açıkyıldız et al. (2014) studied materials for preparation of a low cost activated carbon from plant wastes by activation with ZnCl_2 . They studied the effect of activation parameters such as carbonization temperature ($300\text{-}800^\circ\text{C}$), impregnation ratio (0.5-2) and impregnation time (1-3 h). The highest surface area was $1823 \text{ m}^2/\text{g}$ at carbonization temperature of $400\text{-}500^\circ\text{C}$ from the impregnation ratio of 1.5 and the impregnation time of 1-2 h.

In addition, Hou et al. (2014) prepared the activated carbon (AC) which combined the chemical and physical activation from *L. leucocephala* wood. First, the wood was carbonized in a conventional earth kiln (designated as L), at $560\text{-}750^\circ\text{C}$ for 4 days and a lab-scale tubular reactor (designated as R), at $400 \pm 10^\circ\text{C}$, heating rate $5^\circ\text{C}/\text{min}$ for 1 h. Next, the derived char was activated with chemical activation at

H₂O:char:KOH of 2:1:1, 2:1:2 and 2:1:4 at 800°C followed by carbon dioxide activation at 700, 800 and 900°C. The activating agent was removed from the resulting activated carbons by HCl and rinsed with hot DI water, filtered and dried. The BET surface area of LAC sample increased from 1336.8 m²/g (LAC-4-0.5) to 2326.5 m²/g (LAC-4-4) and the BET surface area of RAC sample increased from 1166.3 m²/g (RAC-4-0.5) to 1438.7 m²/g (RAC-4-4). The obtained activated carbons were used as electrode capacitive deionization (CDI) for water desalination.

2.2 Synthesis of siliceous SBA-15

Siliceous SBA-15 (SBA = Santa Barbara Amorphous) is a mesoporous silica sieve based on uniform hexagonal pores (in range 4-30 nm) with a narrow pore size distribution. A tunable pore diameter was 5 and 15 nm, the thickness of the framework walls of 3.1 to 6.4 nm, high thermal stability and high surface area (400 to above 1000 m²/g) which helped in high dispersion of the active phase (Soni et al., 2013; Huirache-Acuña et al., 2013; Thielemann et al., 2011).

Thielemann et al. (2011) studied the effect of scale-batch synthesis and washing solvent has the influence on the quality of the SBA-15. Pluronic (P123; EO₂₀PO₇₀EO₂₀) was used as template and tetraethoxysilane (TEOS) was used as the silica source. Four grams of P123 was dissolved in distilled water and HCl, then TEOS was added and stirred at 35°C for 20 h. The mixture was aged at 85°C for 24 h, after that the template was removed with distilled water or ethanol. The obtained solid was dried and calcined at 550°C for 12 h.

Yang et al. (2012) synthesized the SBA-15 by using P123 as a template and TEOS as the silica source. The P123 was dissolved in HCl solution and heated to 40°C then,

TEOS was added. The mixture was stirred at 40°C for 20 h and aged at 100°C for 24 h after that filtered, dried and calcined at 550°C for 5 h. The calcined SBA-15 was used as a support for nickel phosphide catalyst and tested in HDO reaction.

2.3 Applications of activated carbon, SBA-15 and metal phosphide catalysts

For the supporting material, Elkasabi et al. (2014) loaded 5 wt.% Pt on carbon and tested in a batch HDO reaction at 320°C under 14.5 MPa, hydrogen atmosphere for 4 h. They found that the sample of Pt/C performed the best in terms of hydrogen consumption and deoxygenation efficiency.

Xin et al. (2016) studied the effect of Ni/P molar ratios of 0.5, 0.8, 1.0, 1.5, 2.0, 3.0 and 4.0 influence for dispersion of metal on support. Application of the catalyst was to produce the high-grade diesel from palmitic acid over nickel phosphide supported on activated carbon. The molar ratios of Ni/P supported on activated showed the phase of pure Ni₂P of 0.5:1 and 0.8:1. At the Ni/P ratios of 1.0:1 and 1.5:1 displayed the mixed phase Ni₂P and Ni₁₂P₅. Increasing the large metal ratio of 2.0:1 showed only crystalline Ni₁₂P₅. At the ratios of 3.0:1 and 4.0:1 showed the mixed phase of Ni₁₂P₅ and Ni. For HDO reaction, the oil yield clearly decreased with increasing the crystalline size of Ni₁₂P₅ and crystalline Ni favors for the cracking reaction.

Echeandia et al. (2010) synthesized Ni-W supported on activated carbon and performed in a flow fixed-bed reactor set-up of phenol HDO at a hydrogen pressure of 1.5 MPa, temperatures ranging from 150 to 300°C and weight hourly space velocity (WHSV) of 0.5 g_{phenol}/(g_{catalyst} h). Before reaction, the catalyst was treated with hydrogen at 400°C for 4 h. From the result at 300°C, the catalyst gave the highest product

selectivity because supporting Ni and W phase on activated carbon induced lower coke formation on the surface.

Sepúlveda et al. (2011) studied the HDO reaction of 2-methoxyphenol using Mo₂N supported on activated carbon (Pica, Norit and Cudu) in a batch reactor in the conditions of temperature at 300°C and hydrogen pressure of 5 MPa. The Mo₂N/Norit catalyst showed the highest activity and conversion.

Srifa et al. (2014) studied important parameters that have effect for HDO of palm oil to BHD product over NiMoS₂/γ-Al₂O₃ including hydrotreating temperature (270-420°C), pressure (1.5-8 MPa), liquid hourly space velocity (LHSV; 0.25-5 h⁻¹) and hydrogen to oil ratio (250-2000 N(cm³/cm³)). The temperature is strongly affected the reaction pathways such as decarbonylation (DCO), decarboxylation (DCO₂), hydrodeoxygenation (HDO), cracking and isomerization, while higher pressure promoted HDO reaction. The high acidity of catalyst has effect for the cracking and selectivity to product.

In addition, Srifa et al. (2015) studied the effect of metal loading including Co, Pd, Pt and Ni on γ-Al₂O₃ and tested in a trickle-bed HDO reaction at 330°C, 5 MPa, LHSV of 1 h⁻¹, and H₂/oil ratio of 1000 N(cm³/cm³). The catalysts with various metal loadings of 2-10 wt.% were prepared by incipient wetness impregnation method. The results showed that the activity of deoxygenation decreased in order of product yield Co > Pd > Pt > Ni when compared at the same amount of metal loading. They found that the activity and selectivity of HDO was dominant when using Co catalyst.

Moreover, many researchers investigated the HDO reaction over metal catalysts with different supports such as alumina, zeolite beta, SAPO-11 and MCM-41 in different condition as shown in Table 2.1. Nickel is a popular metal loading on various

support for HBD reaction because it gave high product yield. Srifa et al. (2014) showed high product yield of sulfide nickel catalyst. Ma and Zho (2015) synthesized high-grade diesel by HDO of palm oil over hierarchical Ni/HBEA catalyst at 260°C and 4 MPa of hydrogen in a batch reactor. The result showed 85% n-C₁₇/C₁₈ production. Liu et al. (2014) prepared Ni supported on the mesoporous SAPO-11 and tested the catalytic performance in HDO of palm oil at 360°C, hydrogen pressure of 4 MPa and LHSV of 1 h⁻¹ in a fixed-bed reactor. The weak and medium of SAPO-11 matched with Ni catalyst decreased the cracking of primary long chain alkane and gave high liquid alkane yield of 70 wt.%. Guan et al. (2016) prepared Ni₂P supported on MCM-41 and studied the catalytic properties of catalyst in HDO of methyl palmitate in a continuous-flow fixed-bed micro-reactor at 290°C, 3 MPa of hydrogen and WHSV of 3 h⁻¹. The result showed the product yield of 84.6 wt.% at lower temperature and pressure. Yang et al. (2012) studied the effect of phosphorous for HDO reaction of Ni/SBA-15 and Ni₂P/SBA-15 catalysts. The result showed that Ni₂P/SBA-15 catalyst more selected to BHD yield and decreased the cracking reaction of the product than Ni/SBA-15 catalyst. Phimsen et al. (2017) compared a series of nickel catalysts of nickel sulfide (NiS), nickel phosphide (NiP) and nickel carbide (NiC) supported on γ -alumina for selectivity in HDO reaction. A catalytic test was carried out at 375-425°C, 20-40 bar hydrogen pressure and the reaction time of 0-3 h. At 400°C, 20 bar hydrogen and reaction time of 2 h, the nickel phosphide catalyst has the highest conversion and selective to diesel product, while nickel carbide was selected to gasoline product. The selectivity of catalyst for diesel product increased in order NiP > NiS > NiC.

Table 2.1 Catalysts, conditions and product yield from HDO reaction.

Catalyst	Feed	T (°C)	H ₂ pressure (bar)	Selectivity for product yield (wt.%)	Reference
Co/ γ -Al ₂ O ₃	Oleic acid (C18:1)	330	50	C18:50.1	Srifa et al. (2015)
Ni/HBEA	Stearic acid (C18:0)	260	40	C18:52.0	Ma and Zho (2015)
Ni/SAPO-11	Palm oil	280	40	C15-C18:52.8	Liu et al. (2014)
NiMoS ₂ / γ - Al ₂ O ₃	Palm oil	330	50	C15-C18:72.4	Srifa et al. (2014)
Ni ₂ P/MCM-41	Methyl palmitate (C17:0)	290	30	C16:58.0	Guan et al. (2016)
Ni/SBA-15	Methyl oleate (C19:1)	340	30	C17:46.0	Yang et al. (2012)
Ni ₂ P/SBA-15	Methyl oleate (C19:1)	340	30	C17:72.0	Yang et al. (2012)
Pd/AC	Stearic acid (C18:0)	300	9	C17:91.0	Santillan-Jimenez et al. (2013)
Ni/AC	Stearic acid (C18:0)	360	40	C17:81.0	Santillan-Jimenez et al. (2013)
Ni ₂ P/AC	Palmitic acid (C16:0)	350	1	C15:74.9	Xin et al. (2016)

2.4 Advantages of bio-hydrogenated diesel (BHD) over fatty acid methyl ester (FAME or biodiesel)

In comparison, from the literature Mikkonen et al. (2008), the bio-hydrogenated diesel production from hydroprocessing of vegetable oil has advantages over biodiesel as the following:

1. The product is compatible with existing engines.
2. Flexibility with the feedstock as the content of free fatty acids in the vegetable oil does not matter.
3. It has higher cetane number.
4. It has higher energy density.
5. It has higher oxidation stability (zero O₂ content).
6. It does not increase the emission of NO_x.
7. It does not require water.
8. There are not by-products that require additional treatment (e.g. glycerol).
9. The distribution of the renewable diesel does not cause additional pollution since it can be transported through the same pipelines that are currently used for distribution of petrodiesel.
10. It has better performance in cold weather.

Comparison the properties of biodiesel and bio-hydrogenated diesel are shown in the Table 2.2.

Table 2.2 Comparison of ester-based biodiesel and hydrocarbon-based green diesel (BHD) from the literature Satyarthi et al. (2013).

Properties	Biodiesel	Green diesel
Chemical composition	Methyl or ethyl ester of fatty acids	Saturated hydrocarbons
Oxygen content	10-12%	Nil
Density (g/ml)	0.880	0.780
Heating value (KJ/g)	38	45
Cloud point (°C)	-5	-5 to +30
Sulfur content (ppm)	<1	<1
Oxidative stability	Unstable	Stable
Cetane number	50-65	70-90
Feedstock flexibility	Good quality	More feedstock flexibility
Production facility	Production require new facility	Can be produced in existing refinery
Engine modification	Some changes required in existing diesel engine	No change is required

2.5 References

- Açıkyıldız, M., Gürses, A., and Karaca, S. (2014). Preparation and characterization of activated carbon from plant wastes with chemical activation. **Microporous and Mesoporous Materials**. 198: 45-49.
- Echeandia, S., Arias, P. L., Barrio, V. L., Pawelec, B., and Fierro, J. L. G. (2010). Synergy effect in the HDO of phenol over Ni-W catalysts supported on active

- carbon: Effect of tungsten precursors. **Applied Catalysis B: Environmental**. 101: 1-12.
- Elkasabi, Y., Mullen, C. A., Pighinelli, A. L. M. T., and Boateng, A. A. (2014). Hydrodeoxygenation of fast-pyrolysis bio-oils from various feedstocks using carbon-supported catalysts. **Fuel Processing Technology**. 123: 11-18.
- Guan, Q., Wan, F., Han, F., Liu, Z., and Li, W. (2016). Hydrodeoxygenation of methyl palmitate over MCM-41 supported nickel phosphide catalysts. **Catalysis Today**. 259: 467-473.
- Hayashi, J., Horikawa, T., Takeda, I., Muroyama, K., and Ani, F. N. (2002). Preparing activated carbon from various nutshells by chemical activation with K_2CO_3 . **Carbon**. 40: 2381-2386.
- Heibati, B., Rodriguez-Couto, S., Al-Ghouti, M. A., Asif, M., Tyagi, I., Agarwal, S., and Gupta, V. K. (2015). Kinetics and thermodynamics of enhanced adsorption of the dye AR 18 using activated carbons prepared from walnut and poplar woods. **Journal of Molecular Liquids**. 208: 99-105.
- Hou, H-C., Liu, N-L., and His, H-C. (2015). Highly porous activated carbons from resource-recovered *Leucaena leucocephala* wood as capacitive deionization electrodes. **Chemosphere**. 141: 71-79.
- Huirache-Acuña, R., Nava, R., Peza-Ledesma, C. L., Lara-Romero, J., Alonso-Núñez, G., Pawelec, B., and Rivera-Muñoz, E. M. (2013). SBA-15 mesoporous silica as catalytic support for hydrodesulfurization catalysts. **Materials**. 6(9): 4139-4167.

- Jambulingam, M., Karthikeyan, S., Sivakumar, P., Kiruthika, J., and Maiyalagan, T. (2007). Characteristic studies of some activated carbons from agricultural wastes. **Journal of Scientific and Industrial Research**. 66: 495-500.
- Liu, Q., Zuo, H., Zhang, Q., Wang, T., and Ma, L. (2014). Hydrodeoxygenation of palm oil to hydrocarbon fuels over Ni/SAPO-11 catalysts. **Chinese Journal of Catalysis**. 35: 748-756.
- Lua, A. C., Yang, T., and Guo, J. (2004). Effects of pyrolysis conditions on the properties of activated carbons prepared from pistachio-nut shells. **Journal of Analytical and Applied Pyrolysis**. 72: 279-287.
- Ma, B., and Zho, C. (2015). High-grade diesel production by hydrodeoxygenation of palm oil over a hierarchically structured Ni/HBEA catalyst. **Green Chemistry**. 17: 1692-1701.
- Mahmoud, D. K., Salleh, M. A. M., Karim, A. W. A., and Idris, A. (2014). Utilization of *Leucaena leucocephala* wood char as bioenergy by-product for methylene blue adsorption: Production, characterization and application. **Journal of Advanced Science and Engineering Research**. 4(4): 204-211.
- Marsh, H., and Rodríguez-Reinoso, F. (2006). **Activated carbon (vol. 1)**. (pp. 324-326). UK: Elsevier's Right Department in Oxford.
- Mikkonen, S. (2008). Second-generation renewable diesel offers advantages. **Hydrocarbon Processing**. 87(2): 63-66.
- Nasri, N. S., Hamza, U. D., Ismail, S. N., Ahmed, M. M., and Mohsin, R. (2014). Assessment of porous carbons derived from sustainable palm solid waste for carbon dioxide capture. **Journal of Cleaner Production**. 71: 148-157.

- Ngernyen, Y., Tangsathitkulchai, C., and Tangsathitkulchai, M. (2006). Porous properties of activated carbon produced from Eucalyptus and wattle wood by carbon dioxide activation. **Korean Journal of Chemical Engineering**. 23(6): 1046-1054.
- Ozdemir, I., Şahin, M., Orhan, R., and Erdem, M. (2014). Preparation and characterization of activated carbon from grape stalk by zinc chloride activation. **Fuel Processing Technology**. 125: 200-206.
- Phimsen, S., Kiatkittipong, W., Yamada, H., Tagawa, T., Kiatkittipong, K., Laosiripojana, N., and Assabumrungrat, S. (2017). Nickel sulfide, nickel phosphide and nickel carbide catalysts for bio-hydrotreated fuel production. **Energy Conversion and Management**. 151: 324-333.
- Phooratsamee, W., Hussaro, K., Teekasap, S., and Hirunlabh, J. (2014). Increasing adsorption of activated carbon from palm oil shell for adsorb H₂S from biogas production by impregnation. **American Journal of Environmental Sciences**. 10(5): 431-445.
- Sahu, J. N., Acharya, J., and Meikap, B. C. (2010). Optimization of production conditions for activated carbons from Tamarind wood by zinc chloride using response surface methodology. **Bioresource Technology**. 101(6): 1974-1982.
- Santillan-Jimenez, E., Morgan, T., Lacny, J., Mohapatra, S., and Crocker, M. (2013). Catalytic deoxygenation of triglycerides and fatty acids to hydrocarbons over carbon-supported nickel. **Fuel**. 103: 1010-1017.
- Satyarthi, J. K., Chiranjeevi, T., Gokak, D. T., and Viswanathan, P. S. (2013). An overview of catalytic conversion of vegetable oils/fats into middle distillates. **Catalysis Science and Technology**. 3(1): 70-80.

- Sepúlveda, C., Leiva, K., García, R., Radovic, L. R., Ghampson, I. L., DeSisto, W. J., García Fierro, J. L., and Escalona, N. (2011). Hydrodeoxygenation of 2-methoxyphenol over Mo₂N catalysts supported on activated carbons. **Catalysis Today**. 172: 232-239.
- Soni, K. K., Boahene, P. E., Rambabu, N., Dalai, A. K., and Adjaye, J. (2013). Hydrotreating of coker light gas oil on SBA-15 supported nickel phosphide catalysts. **Catalysis Today**. 207: 119-126.
- Srifa, A., Faungnawakij, K., Itthibenchapong, V., Viriya-empikul, N., Charinpanitkul, T., and Assabumrungrat, S. (2014). Production of bio-hydrogenated diesel by catalytic hydrotreating of palm oil over NiMoS₂/γ-Al₂O₃ catalyst. **Bioresource Technology**. 158: 81-90.
- Srifa, A., Faungnawakij, K., Itthibenchapong, V., and Assabumrungrat, S. (2015). Roles of monometallic catalysts in hydrodeoxygenation of palm oil to green diesel. **Chemical Engineering Journal**. 278: 249-258.
- Thielemann, J. P., Girgsdies, F., Schlögl, R., and Hess, C. (2011). Pore structure and surface area of silica SBA-15: influence of washing and scale-up. **Beilstein Journal of Nanotechnology**. 2: 110.
- Xin, H., Guo, K., Li, D., Yang, H., and Hu, C. (2016). Production of high-grade diesel from palmitic acid over activated carbon-supported nickel phosphide catalysts. **Applied Catalysis B: Environmental**. 187: 375-385.
- Yang, Y., Ochoa-Hernández, C., de la Peña O'Shea, V. A., Coronado, J. M., and Serrano, D. P. (2012). Ni₂P/SBA-15 as a hydrodeoxygenation catalyst with enhanced selectivity for the conversion of methyl oleate into n-octadecane. **ACS Catalysis**. 2(4): 592-598.

Zhabihi, M., Ahmadpour, A., and Haghghi Asl, A. (2009). Removal of mercury from water by carbonaceous sorbents derived from walnut shell. **Journal of Hazardous Materials**. 167: 230-236.



CHAPTER III

PRODUCTION OF CHARCOAL AND WOOD VINEGAR BY PYROLYSIS OF *L. LEUCOCEPHALA* WOOD

3.1 Abstract

Wood of *L. leucocephala* which is a fast growing unwanted plant was pyrolyzed in a tube furnace and Iwasaki kiln to produce charcoal and wood vinegar. The charcoal was analyzed by X-ray diffraction (XRD), scanning electron microscopy with energy dispersive X-ray fluorescence (SEM-EDX), N₂ adsorption-desorption, elemental analysis (EA) and thermogravimetric analysis (TGA). The charcoal in Iwasaki kiln and tube furnace has a graphite-like structure with surface area of 329 and 3 m²/g, respectively. It was stable in a wide temperature ranges. In addition, wood vinegar was collected during the pyrolysis at three temperature ranges and extracted by *n*-hexane, diethyl ether and ethyl acetate. The compositions depended on collecting temperature. The main components were ketone, organic acids, furan and pyran derivatives, ester, phenol and derivatives, alcohol and alkanes.

3.2 Introduction

Leucaena Leucocephala (*L. leucocephala*) or Lead tree is abundant in Thailand including Nakhon Ratchasima province. It is a fast growing tree which can be considered a problem because it could inhibit the growth of economic plants. From

different origins, *L. leucocephala* wood composed of cellulose (37-41%), hemicellulose (15-20%) and lignin (18-27%) (Antal et al., 2000; Jiménez et al., 2007; Feria et al., 2011). In general, wood can be converted to charcoal via a slow pyrolysis. For example, hemicellulose and cellulose from Moroccan wood decomposed under a nitrogen atmosphere at 180-240°C and 230-310°C, respectively, whereas lignin decomposed slowly in a wide range at 150-750°C (Zerriouh and Belkbir, 1995). During the process, lignocellulose was decomposed (Ozdemir et al. 2014) and produced wood vinegar as a by-product.

Wood vinegar or pyroligneous acid was obtained from condensation of gaseous products during the wood pyrolysis. Wood vinegar is a reddish-brown liquid containing organic acids, phenols, ketones, aldehydes, alcohols and esters. Alcohols, acetic acid and phenols are from decomposition of cellulose, hemicellulose, and lignin, respectively (Wu et al., 2015). Chemical contents in the liquid depended on raw material types and a pyrolysis temperature (Wu et al., 2015; Wei et al., 2010). For example, the wood vinegar was prepared from walnut tree and a waste from the cultivation of walnut fruit at the temperature range of 90-230°C, 230-370°C and 370-450°C (Wei et al., 2010). The wood vinegar from 230-370°C had the highest chemical compositions such as phenols, organic acids, ketones, phenyl ethers, furans and pyran derivatives. Wood vinegar was widely used to promote plant growth because of its effects against pathogens, microbial and insects. Phenols and organic acids were the main organic compounds which had the strongest antimicrobial activity (Ma et al., 2011).

The aim of this Chapter is to produce and characterize the charcoal and the wood vinegar from *L. leucocephala* wood via the conventional carbonization in an Iwasaki

kiln and a tube furnace. Another goal is to analyze components of the wood vinegar by-product.

3.3 Experimental

3.3.1 Configuration of Iwasaki kiln

Pyrolysis of *L. leucocephala* wood was carried out in an Iwasaki kiln with a courtesy from Energy Ashram: Appropriate Technology Association (Nakhon Ratchasima, Thailand). The components were illustrated in Figure 3.1. The kiln was built from a 200-L drum with a dimension of 0.58 m diameter and 0.9 m height. A removable drum covers with a dimension of 0.2 m width and 0.2 m height connected with a 4-bricks entrance. The cement pipe outlet, equipped with a mobile thermocouple, pipelined a vaporized product to a 3-meter stainless steel condenser. The drum was surrounded by a cement wall which was filled by sand. The sand on the kiln top was removed after the pyrolysis was terminated to allow the kiln to cool down.

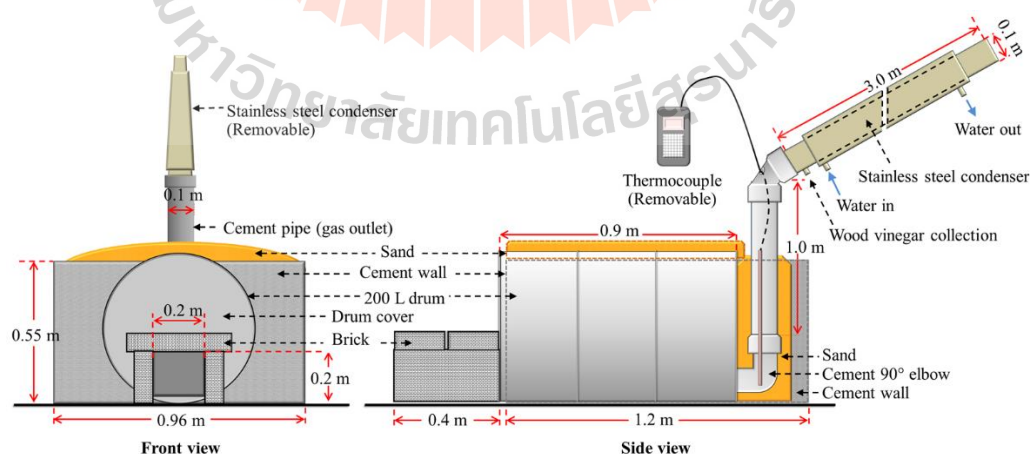


Figure 3.1 Iwasaki kiln from Energy Ashram: Appropriate Technology Association, Nakhon Ratchasima, Thailand.

3.3.2 Pyrolysis process and collection of wood vinegar from Iwasaki kiln

L. leucocephala wood was obtained locally near the university. The fresh wood with diameter around 2 to 5 cm was cut into the length of approximately 80 cm, sundried in an open air for a month and packed in the kiln (see Figure 3.2(a) and (b)). After the kiln was closed, the firewood at the front stove was ignited and allowed to complete, this step indicated by the presence of opaque white smoke. Then, the kiln front was closed and the 3-meter stainless steel condenser was connected to the outlet where the temperature was measured (see Figure 3.2(c)). The carbonization temperature inside the kiln was around 300-400°C. The kiln was left overnight and the charcoal was collected next day. At the beginning of the carbonization process, the gaseous products were condensed to wood vinegar under a continuous water flow and collected based on the temperature of smokestack in three ranges: 80-85°C, 110-115°C and 140-145°C. The wood vinegar from the pyrolysis site was transported to the university where it was refrigerated at 5°C until extraction.

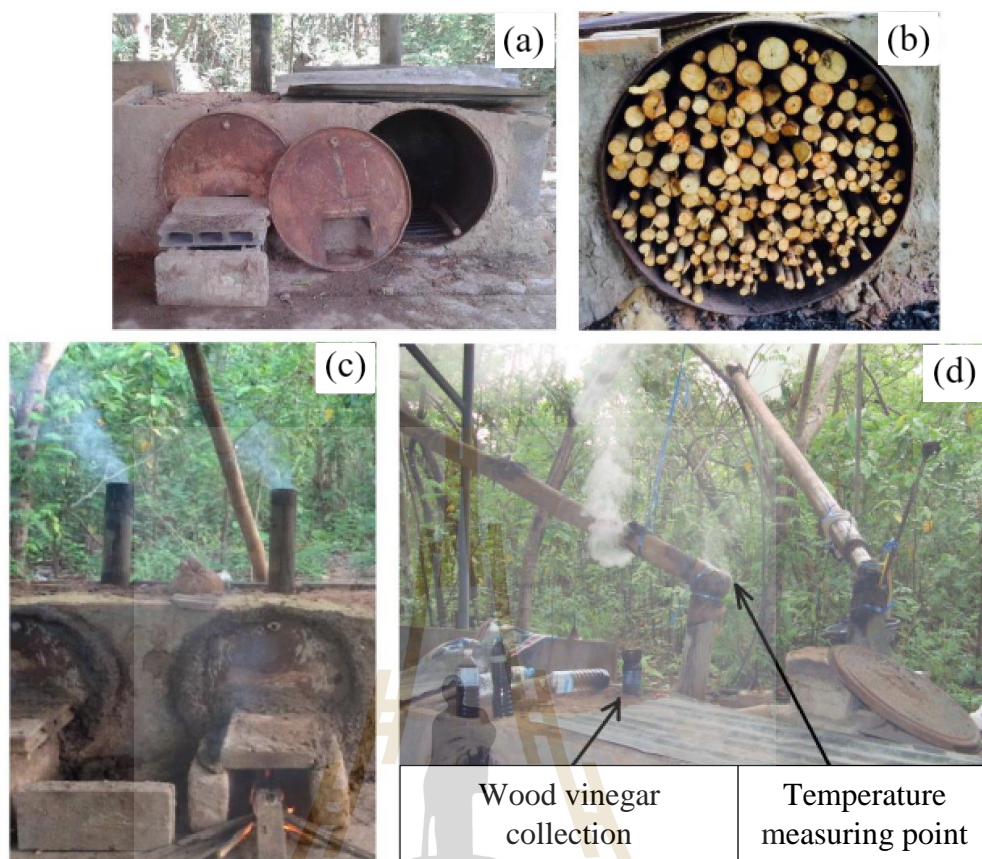


Figure 3.2 Iwasaki kiln and pyrolysis process: (a) front view before packing, (b) after packing with *L. leucocephala* wood, (c) after fire ignition, (d) showing the long condenser tube, point of wood vinegar collection and point of temperature measurement.

3.3.3 Preparation of charcoal in a tube furnace

L. leucocephala wood was cut with a length of 80 cm, dried in sunlight 24 days. Then, it was cut, chopped and dried at 100°C, overnight in a hot air oven. The wood was ground by using mill with 0.50 mm and sieved with 20x30 mesh sizes. A ceramic boat was filled a half with 8 g of the dried wood and placed at the middle of a horizontal tube furnace (Carbolite, UK) with a length of 122.2 cm and internal diameter of 3.8 cm (see Figure 3.3). The sample was purged with N₂ gas about 15 min.

The temperature was increased from room temperature to 400°C in a heating rate of 10°C/min under the N₂ flow (100 ml/min, Lind Gas, 99.995%) and held for 1 h. The decomposition of volatile organic compounds during the carbonization was trapped in the water. After that the furnace was switched off and cool down to ambient temperature under the N₂ gas and then kept in a desiccator for further analysis.

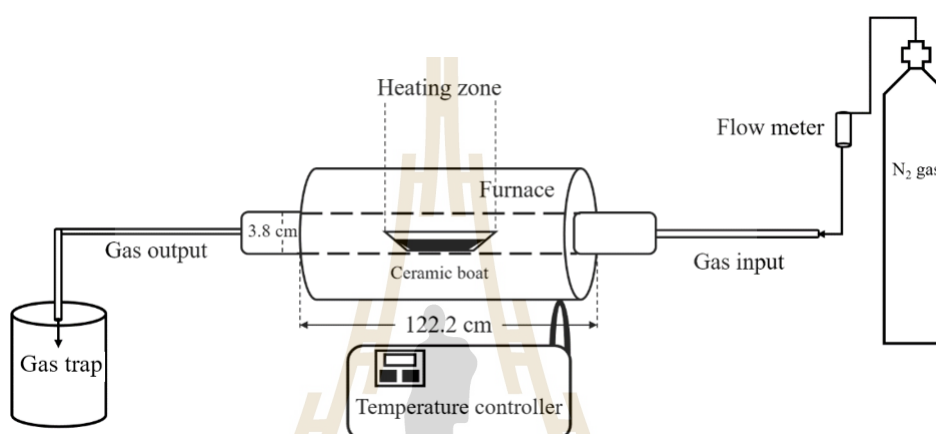


Figure 3.3 A horizontal tube furnace for preparation of charcoal.

3.3.4 Characterization of the charcoal

Morphology of charcoal was analyzed by scanning electron microscopy (SEM, JEOL model JSM-6400) running with an electron beam accelerating voltage of 20 kV, vacuum pressure of 10^{-4} Pa and a tungsten filament. Thermal stability of the charcoal was studied by thermogravimetric analysis (TGA) on a SDT 2960, TGA-DTA, TA Instrument, approximately 10 mg of sample was placed on an aluminum pan and heated from 30 to 900°C with a heating rate 20°C/min under N₂ gas with a flow rate 100 ml/min.

The charcoal was also analyzed by X-ray diffraction (XRD, Bruker AXS D8 diffractometer) using Cu K α radiation with Ni filtered at 40 kV and 40 mA with a step

increment of 0.02 degree and step time of 0.5 s. The elemental composition was determined by elemental analysis (EA, Leco, TruSpec Micro CHNO/S analyzer).

Nitrogen adsorption-desorption isotherms were obtained from a BELSORP-mini II. Before analysis, about 0.15 g of each sample was purged with helium and then pretreated at 150°C under vacuum system. Surface and pore size distribution were obtained from Brunauer-Emmett-Teller (BET) method and Non-Local Density Functional Theory (NL-DFT) method, respectively.

Functional groups of samples were studied by Fourier-transform infrared spectroscopy (FT-IR) (Bruker, Tensor 27). About 0.03 mg of sample was mixed with a small amount of dried KBr, ground and pressed with a hydraulic press. The sample was put on sample holder and measured in the condition; resolution of 4 cm³, sample scans of 500 at 120 mW and scan range from 400 to 4000 cm⁻¹.

3.3.5 Extraction and analysis of wood vinegar by using GC-MS

The refrigerated wood vinegar was warmed to room temperature (in about 2 h) and filtered through Whatman paper no. 2. The filtrate volume of 100 ml was extracted three times with *n*-hexane, a volume of 40, 30 and 30 ml, respectively. After extraction, the *n*-hexane layer was collected in an Erlenmeyer flask, added with anhydrous sodium sulfate (Na₂SO₄) to remove water and filtered through cotton wool. The aqueous layer was separated again with the same ratio of extracting solvent of diethyl ether and ethyl acetate as shown in Figure 3.4, respectively. The three collected fractions were evaporated overnight at room temperature and filtered through Nylon Syringe filter to analyze by GC-MS (Gas Chromatograph; 450-GC, Mass Spectrometer; 320-MS Bruker) with splitless mode, fused silica capillary column stabilwax and helium as a carrier gas with a flow rate of 1 ml/min. The column was heated from 35°C

to 100°C with a rate 3°C/min and to 240°C with a rate 5°C/min, then held for 10 min. The injection port temperature was 250°C. Detection was carried out by electron ionization mass (EI) with ionization energy of 70 eV and the mass acquisition range of 30 to 400 amu (Chinnici et al., 2009). Organic components were identified by matching retention time and mass spectra with library data of mass spectra (NIST). Although the quantitative analysis was not conducted, the peak areas imply the quantity.

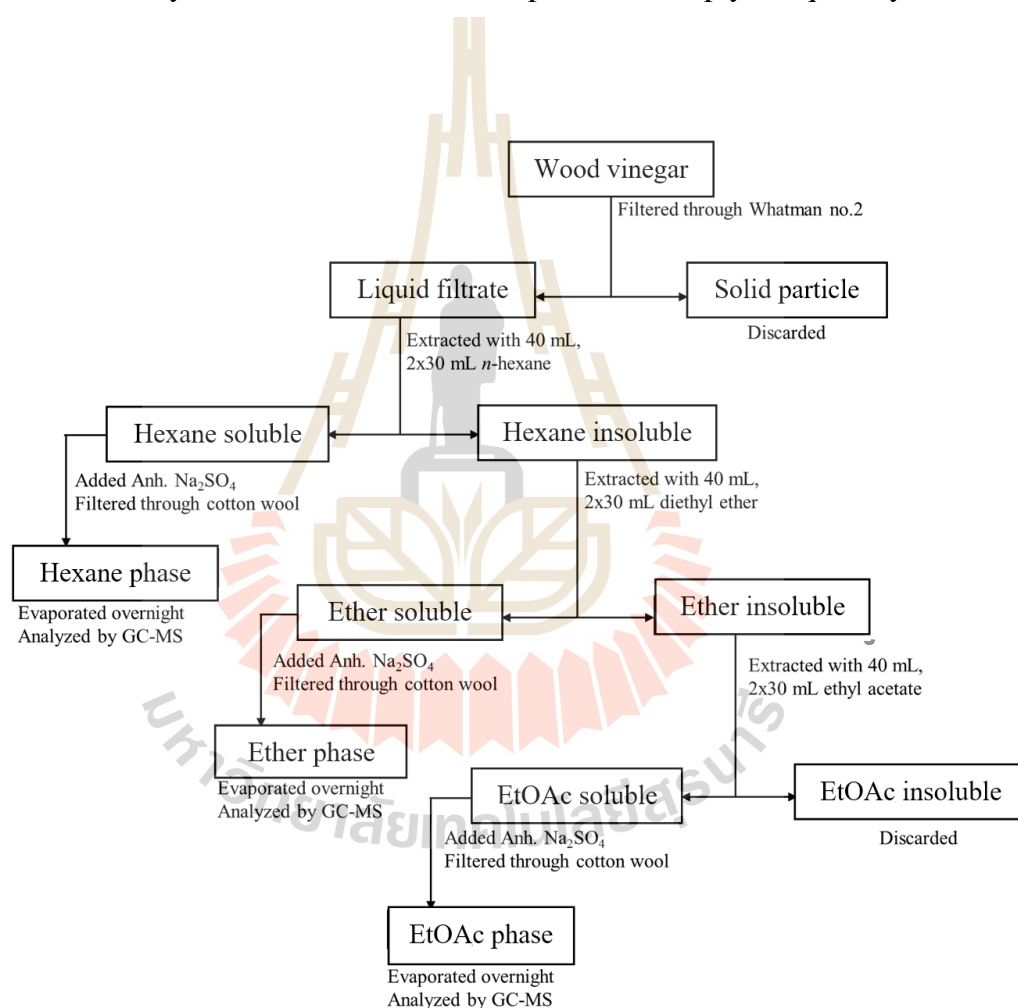


Figure 3.4 Scheme of extraction of *L. leucocephala* wood vinegar.

3.4 Results and discussion

3.4.1 Composition, morphology and thermal stability of *L. leucocephala* charcoal

SEM images of charcoal from various positions are shown in Figure 3.5(a) to (d) displaying a rough external surface and various pore sizes. Figure 3.5(a) and (b) shows the external surface area of the dried wood displayed the roughness material without the vascular structure. After pyrolysis, the decomposition of lignocellulose (cellulose, hemicellulose and lignin) generated mesoporous and microporous structure (see Figure 3.5(c, d)). Figure 3.5(d) also shows pores with diameters of approximately 10-40 μm . Some pores partially contain non-uniform particles. In addition, Figure 3.5(d) shows a macropore which contains small pores on its wall and shows particles attached to the pore wall. Elemental compositions of charcoal measured by SEM-EDX analysis showed that the main component was carbon, 95.31 wt.% (see Figure 3.5(e)). Other elements including silicon (Si), aluminium (Al) and chloride (Cl) were detected. Those were found in biomass and could not be removed under pyrolysis (Raveendran et al., 1995; Lee et al., 2013).

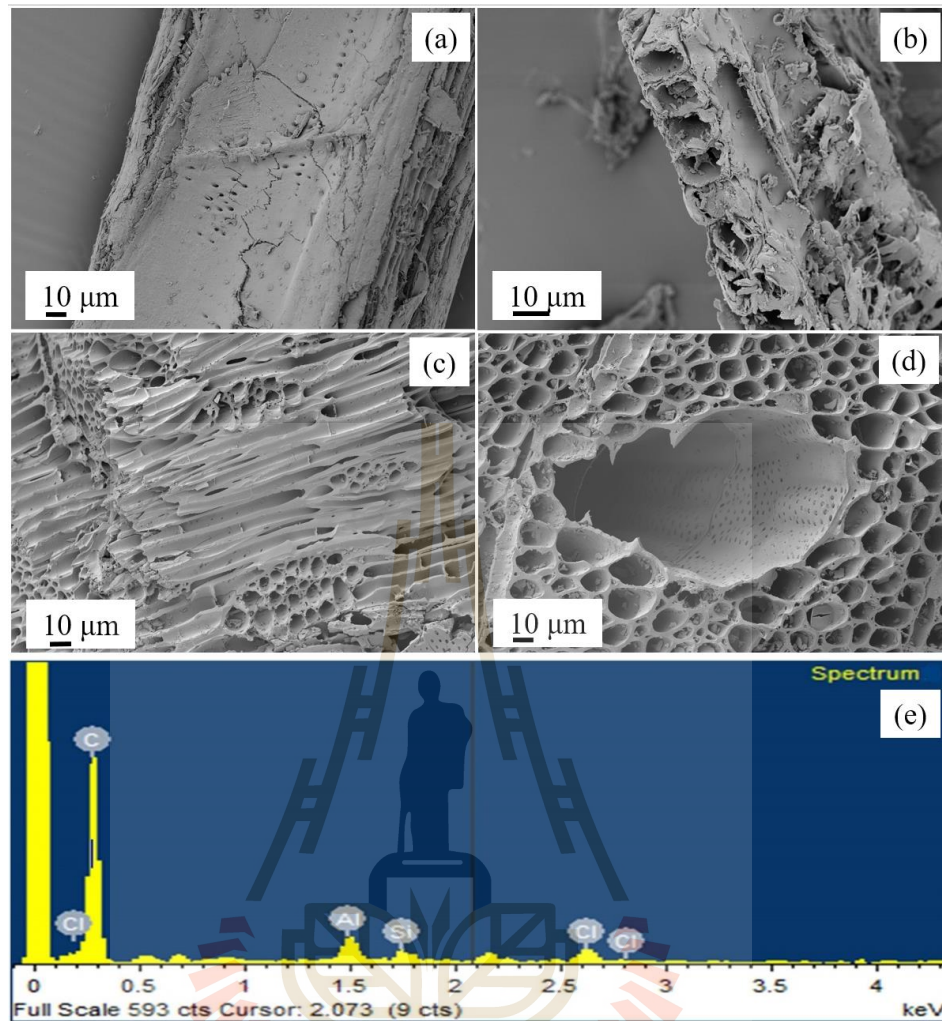


Figure 3.5 SEM images of (a, b) wood, (c, d) charcoal, (e) SEM-EDX of charcoal form *L. leucocephala* wood.

XRD pattern of both charcoal, production from Iwasaki kiln and a tube furnace is shown in Figure 3.6. All of the charcoal displayed two broad diffraction peaks at 24 and 43° corresponding to (002) and (100) reflection planes of graphitic-type lattice in graphitic carbon (*). The diffraction peaks at 29.3, 36.7, 39.3, 47.2 and 48.2° correspond to calcium carbonate, also called calcite were observed (Xu and Poduka, 2014). When the wood, or the leaves, were burnt, the calcium oxalate crystals (monoclinic whewellite, $\text{CaC}_2\text{O}_4 \cdot 2\text{H}_2\text{O}$) or quadratic weddellite, $\text{CaC}_2\text{O}_4 \cdot 2\text{H}_2\text{O}$) were

converted into calcium carbonate when the temperature reach 430-510°C (Brochier and Thinon, 2003). These calcium species were commonly found in the ash of biomass (Raveendran et al., 1995).

The diffraction peaks at 29.3 and 36.7° related to CaCO₃ (o) and CaO (#), respectively (Viriya-empikul et al., 2012). Furthermore, the CaCO₃ peak (o) in Charcoal-TF dominantly decreased and CaO (#) increased, suggesting that CaCO₃ decomposed to CaO when increasing the temperature (Viriya-empikul et al., 2012). The possible reaction mechanism was shown in below.

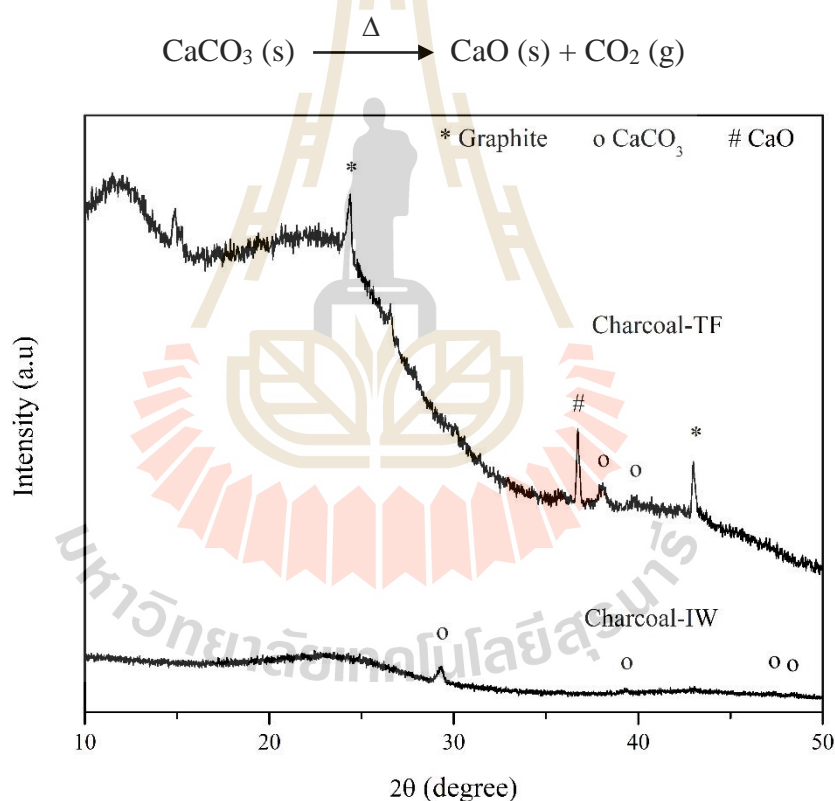


Figure 3.6 XRD patterns of *L. leucocephala* charcoal from Iwasaki kiln and a tube furnace.

Porosity of the charcoal was confirmed by nitrogen adsorption-desorption analysis as shown in Figure 3.7 and Table 3.1. The isotherm was type I according to

the IUPAC classification. This indicated that the microporous topology of the produced carbon material was generated during the pyrolysis (Moreno-Piraján et al., 2010). The specific surface area (S_{BET}) of charcoal in Iwasaki kiln (IW) and a tube furnace (TF) was $392 \text{ m}^2/\text{g}$ and $3 \text{ m}^2/\text{g}$, respectively. The long-time carbonization would transform micropore to mesopore resulting to obtain the both micropores and mesopores volumes. These properties were suitable to further use as an absorbent and support material. In Table 3.1, pore size distribution of Charcoal-IW sample was 1.23 nm that were calculated by DFT mode. In contrast, the sample of Charcoal-TF could not calculate pore size distribution indicating that the gasification did not occur.

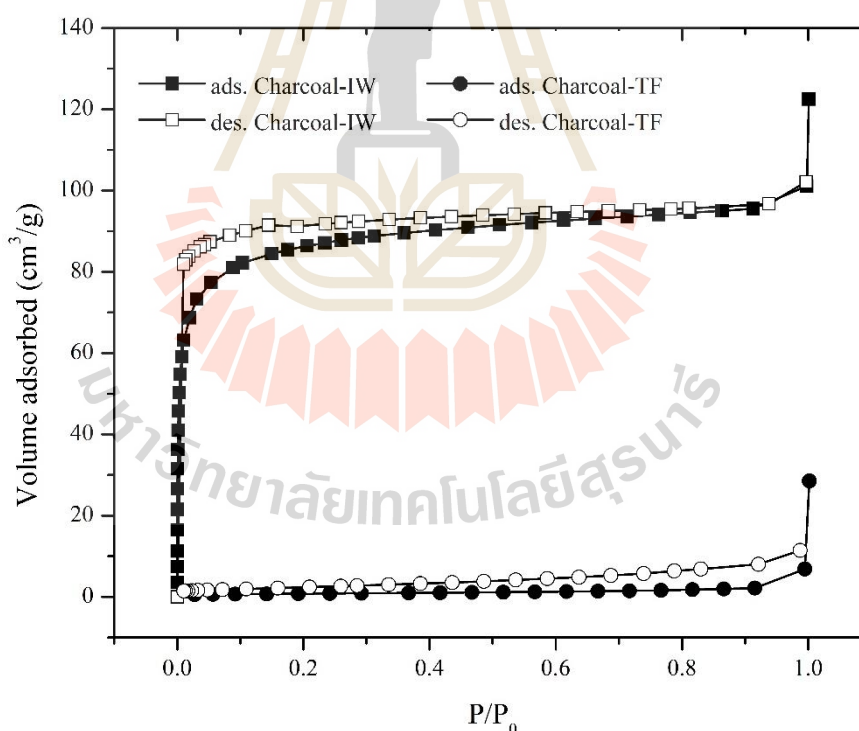


Figure 3.7 Nitrogen adsorption-desorption isotherm of charcoal from Iwasaki kiln and a tube furnace; filled: adsorption, empty: desorption.

Table 3.1 Results from Nitrogen adsorption-desorption analysis of charcoal from Iwasaki kiln and a tube furnace.

Sample	$S_{\text{BET}}^{\text{a}}$ (m^2/g)	$V_{\text{micro}}^{\text{b}}$ (cm^3/g)	$V_{\text{meso}}^{\text{c}}$ (cm^3/g)	$V_{\text{Total}}^{\text{d}}$ (cm^3/g)	D_{p}^{e} (nm)
Charcoal-IW	329	0.143	0.034	0.156	1.23
Charcoal-TF	3	0.001	0.010	0.010	-

Note: a = BET surface area, b = Micropore volume, c = Mesopore volume, d = Total pore volume, e = Mean pore diameter.

Figure 3.8 shows FTIR spectra of the charcoal samples. All of the samples have band positions similar to the literature (Ozdemir et al., 2014). The band around 3400 cm^{-1} corresponds to -OH stretching vibration of alcohol and phenol. The bands around 1600 and 1400 cm^{-1} were assigned C=C aromatic ring stretching vibration (Ozdemir et al., 2014). The band in the region of 1300 to 1000 cm^{-1} might be ascribed to C-O in carboxylic acids, alcohols, phenols, ether or ester groups. The peaks between 900 and 650 cm^{-1} were related to C-H out-of-plane bending of aromatic rings. The peak at 878 cm^{-1} was assigned to isolated H in the aromatic rings (Liu et al., 2016) and at 750 cm^{-1} related to C-H of alkane. The IR results agreed with the elemental analysis that charcoal samples still contain hydrogen and oxygen that confirmed in the results of elemental analysis.

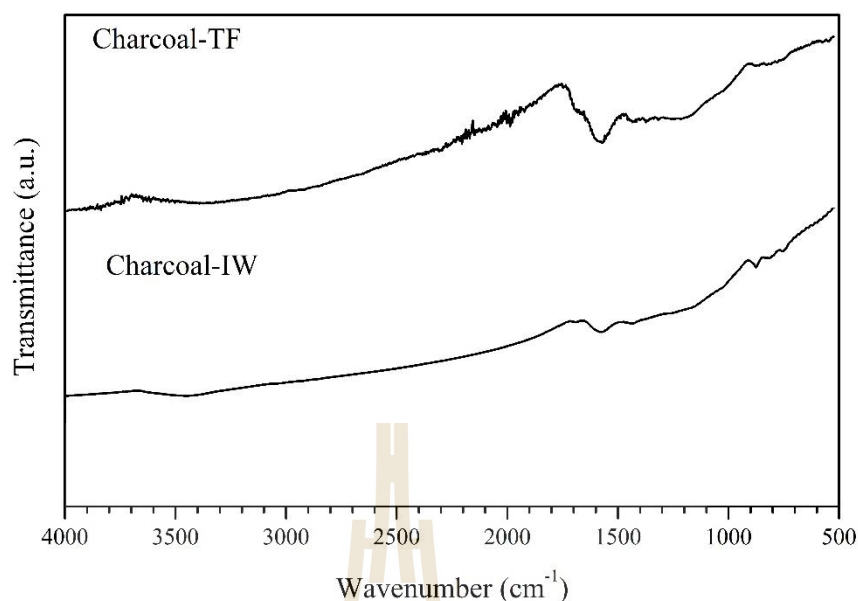


Figure 3.8 FTIR spectra of charcoal from Iwasaki kiln and tube furnace.

Thermograms of *L. leucocephala* wood and charcoal were shown in Figure 3.9(a) and (b), respectively, under inert gas. Figure 3.9(a) shows the weight loss of wood sample in temperature range of 50 to 180°C due to dehydration of sample. The highest weight losses was observed between 220 and 550°C, which indicated the thermal decomposition of lignocellulose (Ozdemir et al., 2014). At temperature above 600°C was not observed significant weight loss. The charcoal samples were shown in Figure 3.9(b). The decrease between 50 and 150°C corresponded to the removal of moisture. Then, the weight loss occurred slightly until approximately 400°C. Therefore, the decrease occurred more sharply until the final temperature. Although, both charcoals were obtained from pyrolysis in Iwasaki kiln and a tube furnace, the weight loss indicated that the pyrolysis was not complete. These were consistent with the elemental analysis that the charcoal still contained 21 and 25% oxygen, respectively (see Table 3.2). Thus, the further decomposition of carbon fiber, cellulose, hemicellulose and

lignin could take place. The degradation of hemicellulose and cellulose took place around 300 and 350°C, respectively (Poletto et al., 2012). The degradation of lignin occurred between 250 and 500°C.

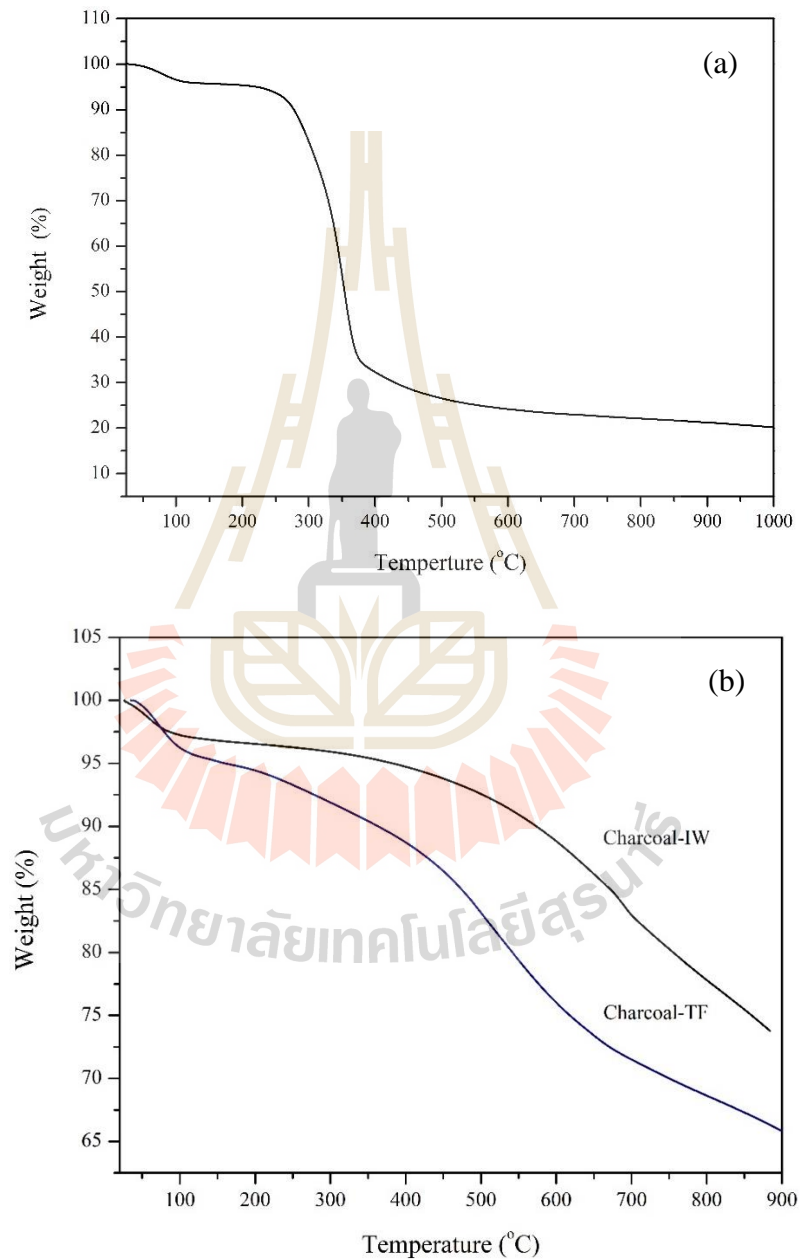


Figure 3.9 TGA results of (a) wood, (b) charcoal from an Iwasaki kiln and a tube furnace.

Elemental compositions of charcoal are shown in Table 3.2. The main component of charcoal was C followed by O with a trace of H, N and S. The oxygen content was estimated by difference [100- (% C+ % H+ % N+ %S)]. The high C content or C/H ratio indicated that pyrolysis in the Iwasaki kiln and a tube furnace converted hydrocarbon compounds to carbon via graphitization (Hou et al., 2015). Long-carbonization time of charcoal-IW gave a lower product yield than charcoal-TF.

Table 3.2 Elemental analysis of charcoal from Iwasaki kiln and a tube furnace.

Sample	Elemental composition (%)					C/H	Product yield (%)
	C	H	N	S	O		
Charcoal-IW	76.18	1.899	0.849	0.069	21.00	40.1	19.6
Charcoal-TF	71.09	3.651	0.571	0.065	24.62	19.4	31.0

3.4.2 Chemicals in wood vinegar from *L. leucocephala* wood

Appearance of wood vinegar collected at various temperatures (80-85°C, 110-115°C and 140-145°C) was displayed in Figure 3.10(a). As the temperature increased, the color of vinegar was darker. With complicate composition and change that may happen during the storage period, the fraction collected at a higher temperature was darker in color with some black residue on the top. During the storage, the wood vinegar seemed to separate to layers. The bottom layer had darker color than the top. Consequently, it was neither worthwhile nor reliable to determine the actual quantity of each compound. As shown from the Figure 3.10(b), the percent yield of wood vinegar decreased from 47.8 % to 1.73% as the smokestack temperature range increased from 80-85°C to 140-145°C. Considering the wood tar was produced by the increase

carbonization temperature corresponding to the pH of wood vinegar increased from 3 to 4. Then, in Iwasaki kiln, the 17.1 liters of wood vinegar were produced from 70.3 kg of *L. leucocephala* wood and gave 13.8 kg of charcoal.

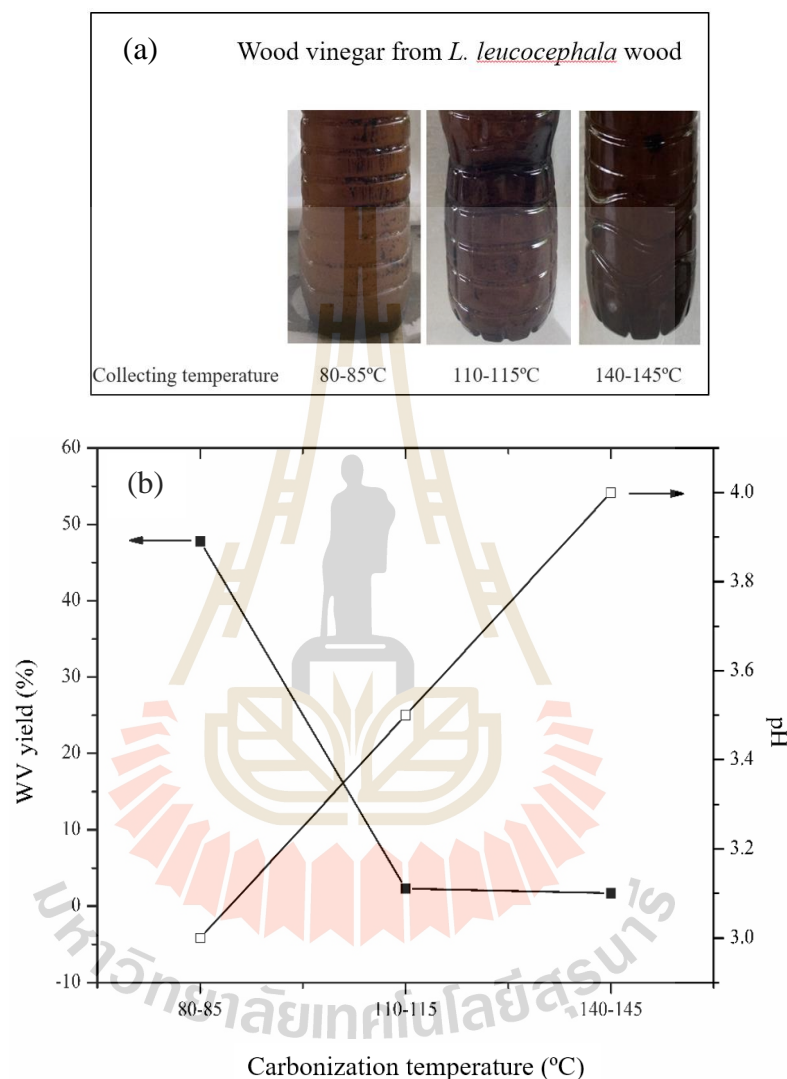


Figure 3.10 (a) Appearance of wood vinegar at various collecting temperatures, (b) wood vinegar yield (%) and pH.

Figure 3.11, the amount of acids, phenol and alkane increased with increasing temperature because high decomposition of cellulose and lignin were the main components in wood vinegar. However, the relative contents of ketone, furan, ester and

alcohol were lower and had no obvious change with the carbonization temperature (Wu et al., 2015). Distribution of the main organic compounds from extraction by each solvent is shown in Figure 3.12. Acids were the major component from the extraction by ethyl acetate and diethyl ether whereas alkanes were extracted well by *n*-hexane. In general, composition and distribution of compounds in wood vinegar vary with type of wood (Wu et al., 2015).

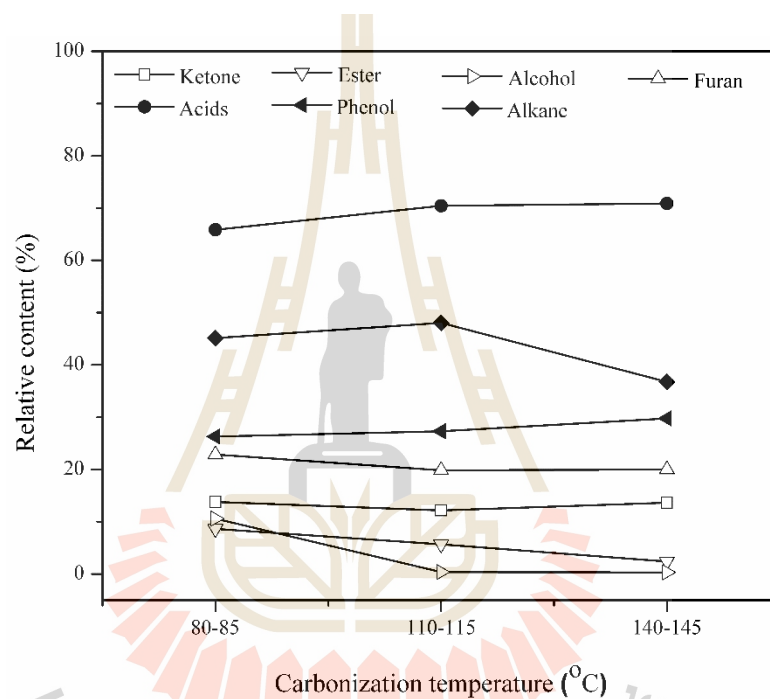


Figure 3.11 The relative content of organic compositions at various collecting temperatures.

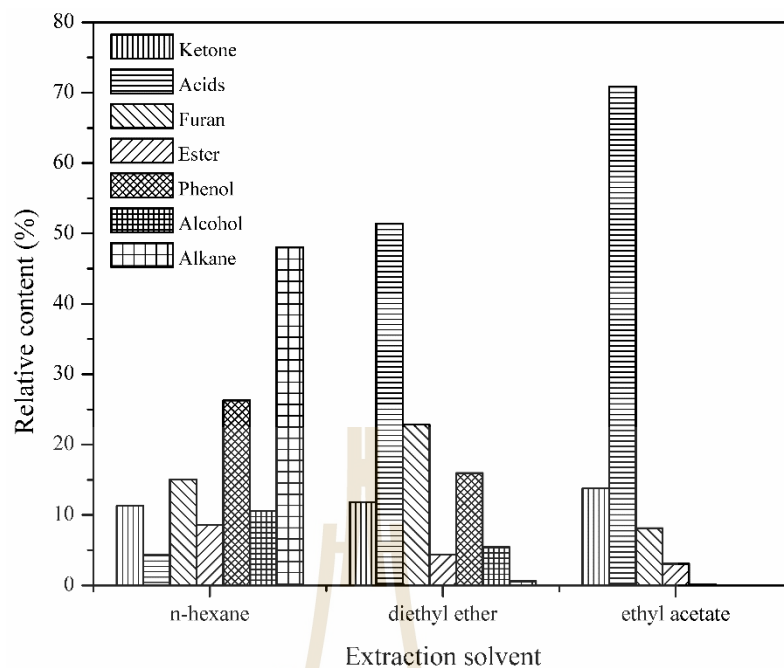


Figure 3.12 Extraction ability of different extraction solvents on main components in wood vinegar.

Table 3.3, 3.4 and 3.5, display the detail of chemicals in the wood vinegar with different solvent extraction and relative amount based on the peak area. In Table 3.3, 43 compounds were identified from extraction with *n*-hexane of the samples collected at 80-85°C, 110-115°C and 140-145°C. The main groups of organic compounds were alkane (48.06% from 110-115°C), phenol and derivatives (29.77% from 140-145°C) and furan and pyran derivatives (15.06% from 140-145°C). Methylcyclopentane was the highest compound which can be extracted to use as a solvent in organic synthesis (Breuer et al., 2014). Table 3.4 shows 46 compounds from extraction with diethyl ether. The main chemical components were organic acids (51.40% from 110-115°C), furan and pyran derivatives (22.84% from 80-85°C) and phenol and derivatives (17.11% from 80-85°C). Table 3.5 shows 32 compounds,

extraction by ethyl acetate, the highest chemical composition was organic acid (70.88% from 140-145°C).

The main compounds in wood vinegar were ketones, organic acids, furan and pyran derivatives, ester, phenol and derivatives, alcohol and alkane. The collecting temperature slightly affected to the yield of each component. The higher temperature could generate smaller chemicals. The highest extracted chemical composition in wood vinegar was acetic acid because it was mainly derived from thermal decomposition of hemicellulose that main chemical composition in *L. leucocephala* wood (28.9-32.9%) (Feria et al., 2011). Acetic acid is widely used as a chemical reagent for production of vinyl acetate monomer and ester. It is also used as a solvent for Friedel-Crafts alkylation. For food production industry, additive could improve the taste, odor and color of the product (Ko et al., 2012).

Table 3.3 Chemical components of *L. leucocephala* wood vinegar collected with varied outlet temperature in *n*-hexane phase detected by GC-MS analysis.

No.	Compounds	Relative percentage (%)		
		80-85°C	110-115°C	140-145°C
Ketone				
1	Cyclopentanone (C ₅ H ₈ O)	0.87	1.22	0.89
2	2-Methyl-2-cyclohexen-1-one (C ₇ H ₁₀ O)	1.11	1.45	1.35
3	2-Methyl-2-cyclopenten-1-one (C ₆ H ₈ O)	1.60	2.20	2.11
4	1-(Acetyloxy)-2-propanone (C ₅ H ₈ O ₃)	0.24	n.d.	0.38
5	3,4-Dimethyl-2-cyclopenten-1-one (C ₇ H ₁₀ O)	n.d.	0.36	0.39
6	2,3,4-Trimethyl-2-cyclopenten-1-one (C ₈ H ₁₂ O)	n.d.	0.32	0.29

n.d. = no detection

Table 3.3 (Continued) Chemical components of *L. leucocephala* wood vinegar collected with varied outlet temperature in *n*-hexane phase detected by GC-MS analysis.

No.	Compounds	Relative percentage (%)		
		80-85°C	110-115°C	140-145°C
7	3-Methyl-2-cyclopenten-1-one (C ₆ H ₈ O)	0.80	n.d.	1.27
8	1-(Acetyloxy)-2-butanone (C ₆ H ₁₀ O ₃)	0.37	0.28	0.49
9	2,3-Dimethyl-2-cyclopenten-1-one (C ₇ H ₁₀ O)	0.93	1.37	1.58
10	2-Hydroxy-3-methyl-2-cyclopenten-1-one (C ₆ H ₈ O ₂)	n.d.	n.d.	0.48
11	3-Ethyl-2-hydroxy-2-cyclopenten-1-one (C ₇ H ₁₀ O ₂)	n.d.	n.d.	0.31
Organic acid				
12	Acetic acid (C ₂ H ₄ O ₂)	0.84	2.32	1.03
13	Propanoic acid (C ₃ H ₆ O ₂)	n.d.	n.d.	0.39
14	Methyl 2-furoate (C ₆ H ₆ O ₃)	n.d.	0.54	0.64
15	Butanoic acid (C ₄ H ₈ O ₂)	0.54	1.04	1.05
16	Pentanoic acid (C ₅ H ₁₀ O ₂)	n.d.	0.40	0.41
Furan and pyran derivatives				
17	Furfural (C ₅ H ₄ O ₂)	2.37	3.61	2.12
18	1-(Furan-2-yl)ethan-1-one (C ₆ H ₆ O ₂)	1.34	2.13	1.94
19	Tetrahydro-2-furanmethanol (C ₅ H ₁₀ O ₂)	4.15	6.98	8.08
20	5-Methyl-2-furancarboxaldehyde (C ₆ H ₆ O ₂)	0.60	0.90	0.90
21	5-Ethyl-2-furaldehyde (C ₇ H ₈ O ₂)	n.d.	n.d.	0.47
22	2-Furanmethanol (C ₅ H ₆ O ₂)	0.77	1.33	1.55
Ester				
23	Ethyl acetate (C ₄ H ₈ O ₂)	8.43	3.30	2.38
24	1,2-Ethanediole, diacetate (C ₆ H ₁₀ O ₄)	0.19	2.38	n.d.
Phenol and derivatives				
25	2-Methoxyphenol (C ₇ H ₈ O ₂)	8.47	1.21	12.07
26	2-Methoxy-6-methylphenol (C ₈ H ₁₀ O ₂)	n.d.	0.56	0.53
27	2-Methoxy-4-methylphenol (C ₈ H ₁₀ O ₂)	3.16	4.60	4.39
28	2-Methylphenol (C ₇ H ₈ O)	1.01	1.36	1.77
29	Phenol (C ₆ H ₆ O)	0.83	1.17	1.68

n.d. = no detection

Table 3.3 (Continued) Chemical components of *L. leucocephala* wood vinegar collected with varied outlet temperature in *n*-hexane phase detected by GC-MS analysis.

No.	Compounds	Relative percentage (%)		
		80-85°C	110-115°C	140-145°C
30	4-Ethyl-2-methoxyphenol (C ₉ H ₁₂ O ₂)	1.69	2.68	2.50
31	2,3-Dimethyl-phenol (C ₈ H ₁₀ O)	n.d.	0.37	0.49
32	4-Methylphenol (C ₇ H ₈ O)	0.31	1.06	0.87
33	3-Methylphenol (C ₇ H ₈ O)	0.74	0.95	1.38
34	2-Methoxy-4-propylphenol (C ₁₀ H ₁₄ O ₂)	n.d.	n.d.	0.31
35	3,5-Dimethylphenol (C ₈ H ₁₀ O)	n.d.	0.63	0.75
36	2,6-Dimethoxyphenol (C ₈ H ₁₀ O ₃)	1.01	1.57	1.82
37	5- <i>Tert</i> -butylpyrogallol (C ₁₀ H ₁₄ O ₃)	0.78	1.15	1.21
38	2-Methyl-1,4-benzenediol (C ₇ H ₈ O ₂)	3.01	n.d.	n.d.
39	Quinhydrone (C ₁₂ H ₁₀ O ₄)	5.27	n.d.	n.d.
Alkyl phenyl ether				
40	1,4-Dimethoxybenzene (C ₈ H ₁₀ O ₂)	n.d.	0.37	0.37
41	1,2,4-Trimethoxybenzene (C ₉ H ₁₂ O ₃)	0.85	1.20	1.29
Alkane				
42	2-Methylpentane (C ₆ H ₁₄)	2.78	2.01	1.37
43	Methylcyclopentane C ₆ H ₁₂	42.37	46.05	35.39

n.d. = no detection

Table 3.4 Chemical components of *L. leucocephala* wood vinegar collected with varied outlet temperature in diethyl ether phase detected by GC-MS analysis.

No.	Compounds	Relative percentage (%)		
		80-85°C	110-115°C	140-145°C
Ketone				
1	Cyclopentanone (C ₅ H ₈ O)	n.d.	n.d.	0.20
2	Hydroxyacetone (C ₃ H ₆ O ₂)	0.77	0.89	0.88
3	2-Methyl-2-cyclohexen-1-one (C ₇ H ₁₀ O)	2.14	1.77	1.76
4	2-Methyl-2-cyclopenten-1-one (C ₆ H ₈ O)	1.21	0.99	0.86
5	1-Hydroxy-2-butanone (C ₄ H ₈ O ₂)	0.58	0.57	0.54
6	1-(Acetyloxy)-2-propanone (C ₅ H ₈ O ₃)	1.65	1.46	1.59
7	3,4-Dimethyl-2-cyclopenten-1-one (C ₇ H ₁₀ O)	n.d.	n.d.	0.17
8	2-Methyl-3-pentanone (C ₆ H ₁₂ O)	0.67	0.46	0.44
9	3-Methyl-2-cyclopenten-1-one (C ₆ H ₈ O)	1.05	0.94	1.20
10	2,3-Dimethyl-2-cyclopenten-1-one (C ₇ H ₁₀ O)	0.75	0.62	0.62
11	Methyl cyclopentenolone (C ₆ H ₈ O ₂)	2.02	1.81	2.21
12	3-Ethyl-2-hydroxy-2-cyclopenten-1-one (C ₇ H ₁₀ O ₂)	0.74	0.58	0.60
13	3-Hydroxy-2-methyl-4H-pyran-4-one (C ₆ H ₆ O ₃)	n.d.	0.62	0.74
Organic acids				
14	Acetic acid (C ₂ H ₄ O ₂)	35.57	45.21	37.39
15	Propionic acid (C ₃ H ₆ O ₂)	4.40	3.87	3.94
16	2-Methylpropanoic acid (C ₄ H ₈ O ₂)	n.d.	n.d.	0.29
17	Butanoic acid (C ₄ H ₈ O ₂)	2.98	2.32	2.71
18	Pentanoic acid (C ₅ H ₁₀ O ₂)	n.d.	n.d.	0.32
Furan and pyran derivatives				
19	Furfural (C ₅ H ₄ O ₂)	3.43	2.86	1.93
20	1-(Furan-2-yl)ethan-1-one (C ₆ H ₆ O ₂)	1.52	1.35	1.23
21	Tetrahydro-2-furanmethanol (C ₅ H ₁₀ O ₂)	6.80	6.49	6.99
22	5-Methylfurfural (C ₆ H ₆ O ₂)	0.52	0.41	0.32
23	2-Furanmethanol (C ₅ H ₆ O ₂)	10.57	8.73	9.37
24	3-Methyl-2(5H)-furanone (C ₅ H ₆ O ₂)	n.d.	n.d.	0.16

n.d. = no detection

Table 3.4 (Continued) Chemical components of *L. leucocephala* wood vinegar collected with varied outlet temperature in diethyl ether phase detected by GC-MS analysis.

No.	Compounds	Relative percentage (%)		
		80-85°C	110-115°C	140-145°C
Ester				
25	Methyl 2-hydroxypropanoate (C ₄ H ₈ O ₃)	n.d.	n.d.	0.23
26	Methyl glycolate (C ₃ H ₆ O ₃)	n.d.	n.d.	0.27
27	2-Oxobutyl acetate (C ₆ H ₁₀ O ₃)	0.85	0.60	0.58
28	Methyl levulinate (C ₆ H ₁₀ O ₃)	n.d.	0.33	0.48
29	2-hydroxyethyl acetate (C ₄ H ₈ O ₃)	n.d.	n.d.	0.27
30	γ -Butyrolactone (C ₄ H ₆ O ₂)	0.57	0.80	1.79
31	Guaiacylacetone (C ₁₀ H ₁₂ O ₃)	1.05	0.76	0.76
Phenol and derivatives				
32	2-Methoxyphenol (C ₇ H ₈ O ₂)	3.26	2.79	2.43
33	2-Methoxy-4-methylphenol (C ₈ H ₁₀ O ₂)	n.d.	n.d.	0.20
34	2-Methylphenol (C ₇ H ₈ O)	0.82	0.54	0.64
35	Phenol (C ₆ H ₆ O)	4.38	2.77	3.92
36	4-Methylphenol (C ₇ H ₈ O)	0.79	0.53	0.61
37	3-Methylphenol (C ₇ H ₈ O)	1.28	0.73	1.01
38	2,6-Dimethoxyphenol (C ₈ H ₁₀ O ₃)	3.05	2.60	2.45
39	3-Methoxy-1,2-benzenediol (C ₇ H ₈ O ₃)	1.33	1.32	1.26
40	3,4-Dimethoxyphenol (C ₈ H ₁₀ O ₃)	n.d.	n.d.	0.49
41	Benzene-1,2-diol (C ₆ H ₆ O ₂)	2.20	1.99	2.32
42	4-Methylbenzene-1,2-diol (C ₇ H ₈ O ₂)	n.d.	n.d.	0.63
Alcohol				
43	Pentan-3-ol (C ₅ H ₁₂ O)	n.d.	0.36	0.32
Alkyl phenyl ether				
44	2-Methoxypyridine (C ₆ H ₇ NO)	n.d.	n.d.	0.29
45	1,2,4-Trimethoxybenzene (C ₉ H ₁₂ O ₃)	0.73	0.66	0.58
Alkane				
46	2-Methylbutane (C ₅ H ₁₂)	0.61	0.26	0.38

n.d. = no detection

Table 3.5 Chemical components of *L. leucocephala* wood vinegar collected with varied outlet temperature in ethyl acetate phase detected by GC-MS analysis.

No.	Compounds	Relative percentage (%)		
		80-85°C	110-115°C	140-145°C
Ketone				
1	Propan-2-one (C ₃ H ₆ O)	2.24	0.95	1.97
2	Butane-2,3-dione (C ₄ H ₆ O ₂)	0.47	0.28	n.d.
3	3-Hydroxy-2-butanone (C ₄ H ₈ O ₂)	0.72	0.57	0.63
4	1-Hydroxy-2-propanone (C ₃ H ₆ O ₂)	3.02	3.38	3.62
5	2-Methyl-2-cyclohexen-1-one (C ₇ H ₁₀ O)	2.44	1.94	1.85
6	2-Methyl-2-cyclopenten-1-one (C ₆ H ₈ O ₂)	0.31	0.22	0.18
7	1-Hydroxy-2-butanone (C ₄ H ₈ O ₂)	1.30	1.23	1.23
8	2-Propanone, 1-(acetyloxy)- (C ₅ H ₈ O ₃)	2.11	1.86	2.28
9	3-Methyl-2-cyclopenten-1-one (C ₆ H ₈ O)	0.54	0.81	0.95
10	2-Hydroxy-3-methyl-2-cyclopenten-1-one (C ₆ H ₈ O ₂)	0.95	0.91	0.93
Organic acids				
11	Acetic acid, hydroxy-, methyl ester (C ₃ H ₆ O ₃)	0.64	0.76	0.80
12	Acetic acid (C ₂ H ₄ O ₂)	62.93	67.84	67.90
13	Propanoic acid (C ₃ H ₆ O ₂)	2.01	1.59	1.91
14	Pentanoic acid, 4-oxo-, methyl ester (C ₆ H ₁₀ O ₃)	0.27	0.24	0.27
Furan and pyran derivatives				
15	Furfural (C ₅ H ₄ O ₂)	0.81	0.52	n.d.
16	1-(Furan-2-yl)ethan-1-one (C ₆ H ₆ O ₂)	0.51	0.47	0.47
17	Tetrahydro-2-Furanmethanol (C ₅ H ₁₀ O ₂)	3.25	2.92	2.73
18	2(3H)-Furanone, dihydro-5-methyl- (C ₅ H ₈ O ₂)	n.d.	n.d.	0.14
19	2-Furanmethanol (C ₅ H ₆ O ₂)	3.56	2.67	2.46
20	3-Methyl-2(5H)-Furanone (C ₅ H ₆ O ₂)	n.d.	0.17	1.71
21	2(5H)-Furanone (C ₄ H ₄ O ₂)	n.d.	0.29	0.35
Phenol and derivatives				
22	Methyl 2-hydroxypropanoate (C ₄ H ₈ O ₃)	0.47	0.41	0.41

n.d. = no detection

Table 3.5 (Continued) Chemical components of *L. leucocephala* wood vinegar collected with varied outlet temperature in ethyl acetate phase detected by GC-MS analysis.

No.	Compounds	Relative percentage (%)		
		80-85°C	110-115°C	140-145°C
23	2-Hydroxyethyl acetate (C ₄ H ₈ O ₃)	n.d.	0.33	0.52
24	Butyrolactone (C ₄ H ₆ O ₂)	n.d.	2.32	n.d.
Phenol and derivatives				
25	Phenol (C ₆ H ₆ O)	n.d.	0.16	n.d.
Alcohol				
26	Methanol (CH ₃ OH)	8.72	5.44	2.76
27	Ethanol (C ₂ H ₆ O)	0.61	n.d.	0.17
28	Pentan-3-ol (C ₅ H ₁₂ O)	0.26	n.d.	0.17
29	3-Hydroxy-2-methyl-4 <i>H</i> -pyran-4-one (C ₆ H ₆ O ₃)	n.d.	n.d.	0.39
Alkyl phenyl ether				
30	Pyridine (C ₅ H ₅ N)	n.d.	n.d.	0.46
31	2-Methylpyridine (C ₆ H ₇ N)	n.d.	n.d.	0.23
32	3-Methoxypyridine (C ₆ H ₇ NO)	0.20	0.25	0.23
n.d. = no detection				

3.5 Conclusions

Charcoal from *L. leucocephala* wood was obtained from pyrolysis in an Iwasaki kiln and a tube furnace. All samples have graphitic structure with low crystallinity. They show adsorption isotherm type I. Functional groups of the charcoal were also analyzed and the results were in good agreement with elemental analysis. Moreover, wood vinegar is collected at various temperatures during the pyrolysis of Lead tree wood. After extraction with *n*-hexane, diethyl ether and ethyl acetate, the compounds are analyzed by GC-MS. The main compounds are ketones, organic acids, furan and pyran derivatives, ester, phenol and derivatives, alcohol and alkanes.

3.6 References

- Antal, M. J., Allen, S. G., Dai, X., Shimizu, B., Tam, M. S., and Grønli, M. (2000). Attainment of the theoretical yield of carbon from biomass. **Industrial and Engineering Chemistry Research**. 39(11): 4024-4031.
- Breuer, D., and Friedrich, C. (2014). Hexane isomers (except n-hexane) and methylcyclopentane [Air monitoring methods, 2013]. **The MAK Collection for Occupational Health and Safety**. 1-15.
- Brochier, J. E., and Thinon, M. (2003). Calcite crystals, starch grains aggregate or...POCC? Comment on 'calcite crystals inside archaeological plant tissues'. **Journal of Archaeological Science**. 30(9): 1211-1214.
- Chinnici, F., Duran Guerrero, E., Sonni, F., Natali, N., Natera Marín, R., and Riponi, C. (2009). Gas chromatography-mass spectrometry (GC-MS) characterization of volatile compounds in quality vinegars with protected European geographical indication. **Journal of Agricultural and Food Chemistry**. 57(11): 4784-4792.
- Feria, M. J., López, F., García, J. C., Pérez, A., Zamudio, M. A., and Alfaro, A. (2011). Valorization of *Leucaena leucocephala* for energy and chemicals from autohydrolysis. **Biomass and Bioenergy**. 35(5): 2224-2233.
- Hou, C. H., Liu, N. L., and Hsi, H. C. (2015). Highly porous activated carbons from resource-recovered *Leucaena leucocephala* wood as capacitive deionization electrodes. **Chemosphere**. 141: 71-79.
- Jiménez, L., Pérez, A., de la Torre, M. J., Moral, A., and Serrano, L. (2007). Characterization of vine shoots, cotton stalks, *Leucaena leucocephala* and *Chamaecytisus proliferus*, and of their ethyleneglycol pulps. **Bioresource Technology**. 98(18): 3487-3490.

- Ko, W. C., Cheng, J. Y., Chen, P. Y., and Hsieh, C. W. (2013). Optimized extraction method of acetic acid in vinegar and its effect on SNIF-NMR analysis to control the authenticity of vinegar. **Food and Bioprocess Technology**. 6(8): 2202-2206.
- Lee, Y., Park, J., Gang, K. S., Ryu, C., Yang, W., Jung, J. H., and Hyun, S. (2013). Production and characterization of biochar from various biomass materials by slow pyrolysis. **Technical Bulletin Journal-Food and Fertilizer Technology Center**. 197: 1-11.
- Liu, Z., Huang, Y., and Zhao, G. (2016). Preparation and characterization of activated carbon fibers from liquefied wood by $ZnCl_2$ activation. **BioResources**. 11(2): 3178-3190.
- Ma, X., Wei, Q., Zhang, S., Shi, L., and Zhao, Z. (2011). Isolation and bioactivities of organic acids and phenols from walnut shell pyrolygneous acid. **Journal of Analytical and Applied Pyrolysis**. 91(2): 338-343.
- Moreno-Piraján, J. C., Tirano, J., Salamanca, B., and Giraldo, L. (2010). Activated carbon modified with copper for adsorption of propanethiol. **International Journal of Molecular Sciences**. 11(3): 927-942.
- Ozdemir, I., Şahin, M., Orhan, R., and Erdem, M. (2014). Preparation and characterization of activated carbon from grape stalk by zinc chloride activation. **Fuel Processing Technology**. 125: 200-206.
- Poletto, M., Zattera, A. J., and Santana, R. M. (2012). Thermal decomposition of wood: kinetics and degradation mechanisms. **Bioresource Technology**. 126: 7-12.
- Raveendran, K., Ganesh, A., and Khilar, K.C. (1995). Influence of mineral matter on biomass pyrolysis characteristics. **Fuel**. 74(12): 1812-1822.

- Viriya-empikul, N., Krasae, P., Nualpaeng, W., Yoosuk, B., and Faungnawakij, K., 2012. Biodiesel production over Ca-based solid catalysts derived from industrial wastes. **Fuel**. 92: 239-244.
- Wei, Q., Ma, X., and Dong, J. (2010). Preparation, chemical constituents and antimicrobial activity of pyroligneous acids from walnut tree branches. **Journal of Analytical and Applied Pyrolysis**. 87(1): 24-28.
- Wu, Q., Zhang, S., Hou, B., Zheng, H., Deng, W., Liu, D., and Tang, W. (2015). Study on the preparation of wood vinegar from biomass residues by carbonization process. **Bioresource Technology**. 179: 98-103.
- Xu, B., and Poduska, K. M. (2014). Linking crystal structure with temperature-sensitive vibrational modes in calcium carbonate minerals. **Physical Chemistry Chemical Physics**. 16(33): 17634-17639.
- Zeriouh, A., and Belkbir, L. (1995). Thermal decomposition of a Moroccan wood under a nitrogen atmosphere. **Thermochimica Acta**. 258: 243-248.

CHAPTER IV

PREPARATION OF ACTIVATED CARBON FROM CHARCOAL PRODUCED IN IWASAKI KILN AND TUBE FURNACE

4.1 Abstract

Activated carbons were produced from charcoals of *L. leucocephala* or Lead tree that were prepared in Iwasaki kiln and tube furnace. The charcoal was ground in to three different particle sizes (large, medium and small) and activated with carbon dioxide (CO₂) and zinc chloride (ZnCl₂). Activating temperatures were varying in three temperature ranges of 600, 700 and 800°C. Structure, morphology, elemental composition, porosity and functional groups of activated carbon samples were compared with the charcoal precursor. The medium particle size of charcoal gave the activated carbon with the large surface area and carbon content, up to 593 m²/g and 90%, respectively. The obtained activated carbons were characterized by XRD to confirm the patterns of graphitic carbon. Surface functional group and graphitic carbon were analyzed by FT-IR and Raman spectroscopy. The elemental compositions were analyzed by elemental analysis (EA). The morphology and surface area were characterized by SEM, TEM and Nitrogen adsorption-desorption techniques.

4.2 Introduction

As mentioned in Chapter III, charcoals were produced from *L. leucocephala* wood in an Iwasaki kiln (IW) and a tube furnace (TF). Graphitic-like structure and high carbon content of charcoal make them interesting as a source for activated carbon (AC). As the surface area of the charcoals were low, this could be improved by varying activating temperatures and produced through physical and chemical methods under nitrogen gas.

As the charcoal from pyrolysis is rich in carbon, it can be modified to activated carbon to increase porosity, internal surface area and mechanical strength (Sahu et al., 2010). Activated carbon is a carbonaceous materials resembling granular or powder charcoal. It is widely used in many applications, for example, as an adsorbent for methylene blue (Mahmoud et al., 2014; Açıkyıldız et al., 2014; Angın et al., 2013), as a part of electrode for capacitive deionization (Hou et al., 2015) and as a support material for metal catalysts (Xin et al., 2016; Cheng et al., 2016).

Many researchers studied the activation process that was concerned for low cost materials and activating process to increase the surface area and inhibited tar formation. Other by-products were influenced for decreasing the carbon yield. Activated carbon can be produced from various kinds of wood such as grape stalk (Ozdemir et al., 2014), eucalyptus and wattle wood (Ngernyen et al., 2006), Tamarind (Sahu et al., 2010), walnut and poplar (Heibati et al., 2015), and Lead tree (Mahmoud et al., 2014; Hou et al., 2015). Morphology and porosity of activated carbon depended on the types of raw materials and activation conditions.

Activated carbon can be produced by chemical activation and physical activation. The chemical activation employed chemicals which have to be washed out and

generated waste. Ozdemir et al. (2014) prepared activated carbon by chemical activation by ZnCl_2 , KOH and H_3PO_4 . The advantages of this method were low energy cost, short activating time, and high product yield when compared with physical activation. The most widely used activating chemical was ZnCl_2 . The process began with impregnation of a raw material with the activating reagent and heated in the inert atmosphere ($500\text{-}700^\circ\text{C}$). On the other hand, physical activation by a non-toxic gas was more environmental friendly. The most widely used activating agent was carbon dioxide (CO_2) and the process involves carbonization and activation. Ngernyen et al. (2006) prepared activated carbon by physical activation with CO_2 , air and steam. Raw materials were carbonized under inert atmosphere and then resulting charcoal was activated by carbon dioxide at high temperature ($800\text{-}1,100^\circ\text{C}$). The advantage of this method has high BET surface area. However, the activation may be limited by the size of charcoal, the activation by carbon dioxide could be more thoroughly when the charcoal with the small size was used.

In this Chapter activated carbon is produced and characterized. Then it is applied as a catalyst supporting material (in Chapter V). The effect of charcoal particle size and activating methods on properties of activated carbon is studied.

4.3 Experimental

4.3.1 Preparation of activated carbon

4.3.1.1 Physical activation with carbon dioxide (CO_2)

Activated carbon was prepared by a procedure modified from literature (Ngernyen et al., 2006). The obtained charcoal was ground by using ball mill, sieved and classified into three different sizes: large (L, between $2.36\text{ mm-}1.70\text{ mm}$),

medium (M, 1.70 mm-250 μm) and small (S, 250 μm -180 μm). The charcoal was dried at 100°C overnight in a hot-air oven. Then, the dried charcoal (4 g) was filled in a ceramic boat and placed at the middle of a horizontal tube furnace (Carbolite, UK) with a length of 122.2 cm and internal diameter of 3.8 cm and purged with nitrogen for about 15 min. The setup of activating equipment is shown in Figure 4.1. The temperature was increased from room temperature to desire temperature at a heating rate of 10°C/min under the flow of nitrogen (100 ml/min, Lind Gas, 99.995%). After the nitrogen flow was stopped, carbon dioxide (Lind Gas, 99.9%) was flowed into the furnace at a constant flow rate of 100 ml/min and held for 1 h. After that the power was switched off and the furnace was allowed to cool to ambient temperature under the flow of nitrogen. The obtained activated carbon was collected and stored in a desiccator for further analysis. The samples from large, medium and small charcoal particles were named L-AC-C, M-AC-C and S-AC-C, respectively. “C” noted as carbon dioxide activation.

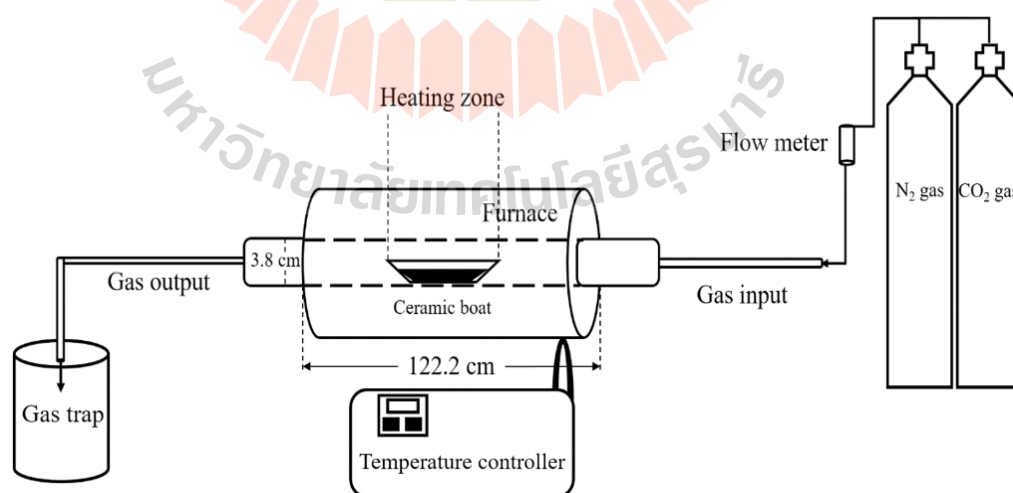


Figure 4.1 Equipment setup for activation in a horizontal tube furnace.

4.3.1.2 Chemical activation with zinc chloride (ZnCl₂)

The chemical activation procedure was modified from literature (Angin et al., 2013 and Jambulingam et al., 2007). The obtained charcoal was ground by using ball mill, sieved and classified into three different sizes as mentioned in section 4.3.1.1 and then dried in a hot-air oven at 100°C overnight. Impregnation ratio of ZnCl₂: charcoal was 4:1. Twenty grams of zinc chloride was dissolved in 250 ml of DI water, and then 5 g of dried charcoal was mixed with the zinc chloride solution by refluxing and stirring at 80°C for 24 h to ensure the adsorption complete. The mixture was filtered with Whatman™ paper no. 1 and the remaining solid was dried at 105°C for 24 h. Then, the dried charcoal (4 g) was filled in a ceramic boat and placed at the middle of a horizontal tube furnace (Carbolite, UK) with a length of 122.2 cm and internal diameter of 3.8 cm and purged with nitrogen for about 15 min. The temperature was increased from room temperature to desire temperature at a heating rate of 10°C/min under the flow of nitrogen (100 ml/min, Lind Gas, 99.995%) and held for 1h. After that the power was switched off and the furnace was allowed to cool to ambient temperature under the flow of nitrogen. Then the sample was refluxed and stirred with 100 ml of 1.0 M HCl solution at 90°C for 30 min to leach out the activating agent, filtered and rinsed with warm DI water in several times until the pH was 7, and dried at 105°C for 24 h. The samples from large, medium and small charcoal particles were named L-AC-Z, M-AC-Z and S-AC-Z, respectively. “Z” noted as zinc chloride activation.

4.3.2 Characterization of the activated carbon

Morphology of activated carbon was analyzed by scanning electron microscopy (SEM, JEOL model JSM-6400) running with an electron beam accelerating voltage of 20 kV, vacuum pressure of 10⁻⁴ Pa and a tungsten filament. Transmission

electron microscopy (TEM, JEOL model JEM-2100) running of 200 kV. Sample preparation, a small amount of the sample was dispersed into 1 ml of ethanol (99 wt.%), sonicated for 10 min and dropped on carbon film on 200-square-mesh copper grid and dried. The grid was put into TEM sample holder and inserted into vacuum chamber. The voltage for electron acceleration was 200 mV.

Thermal stability of the activated carbon was studied by thermogravimetric analysis (TGA) on a SDT 2960, TGA-DTA, TA Instrument, approximately 10 mg of sample was placed on an aluminum pan and heated from 30°C to 900°C with a heating rate 20°C/min under N₂ gas with a flow rate 100 ml/min.

The activated carbon was also analyzed by X-ray diffraction (XRD, Bruker AXS D8 diffractometer) using Cu K α radiation with Ni filtered at 40 kV and 40 mA with a step increment of 0.02 degree and step time of 0.5 s. The elemental composition was determined by elemental analysis (EA, Leco, TruSpec Micro CHNO/S analyzer).

Nitrogen adsorption-desorption isotherms were obtained from a BELSORP-mini II. Before analysis, about 0.15 g of each sample was purged with helium and then pretreated at 150°C under vacuum system. Surface area and pore size distribution were obtained from Brunauer-Emmett-Teller (BET) method and Non-Local Density Functional Theory (NL-DFT) method, respectively.

Functional groups of samples were studied by Fourier-transform infrared spectroscopy (FTIR) (Bruker, Tensor 27). About 0.03 mg of sample was mixed with a small amount of dried KBr, ground and pressed with a hydraulic press. The sample was put on sample holder and measured in the condition; resolution of 4 cm⁻¹, sample scans of 500 at 120 mW and scan from 400 to 4000 cm⁻¹ for FTIR mode and 900-3600 cm⁻¹ for Raman mode.

4.4 Results and discussion

4.4.1 Characterization of activated carbon from physical activation

After pyrolysis, the pores were generated. Figure 4.2 displays the SEM images of charcoal and activated carbons prepared by physical activation with carbon dioxide. The morphology of activated carbon was similar to charcoal, containing pores with various diameters. After activation, some particles on the surface and in the pores were removed. The majority of pores from all samples were macropores with diameter around 2-5 μm . Some of the pores were partially blocked by some non-uniform particles. Moreover, larger pore with diameter about 10-20 μm were observed.

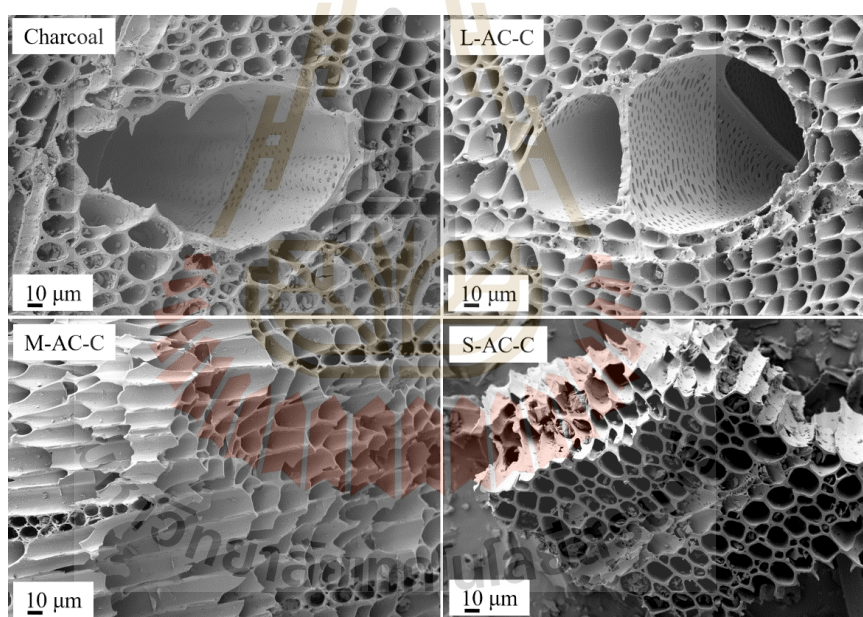


Figure 4.2 SEM images of charcoal and activated carbons with different sizes preparation by physical activation (CO_2) at 800°C for 1 h.

Figure 4.3 shows XRD patterns of charcoal and activated carbon prepared by physical method with carbon dioxide for large, medium and small sizes as notes as L-AC-C, M-AC-C and S-AC-C, respectively. All the samples display two broad

diffraction peaks at 24 and 43° corresponding to (002) and (100) reflection corresponding to a graphitic-type lattice in graphitic carbon (o). This (100) reflection indicates a limited degree of graphitization (Xu et al., 2014). The diffraction peaks at 29.3, 36.7, 38.3, 47.2 and 48.2° related to calcium carbonate species (#) were observed (Viriya-empikul et al., 2012). About the details of calcium carbonate species were mentioned in Chapter III. Usually, such calcium species widely found in biomass under pyrolysis atmosphere (Raveendran et al., 1995). The peaks of calcium carbonate species increased when the particle of charcoal was smaller. To confirm the existence of calcium carbonate, the particle in the pore was analyzed by SEM-EDX, see Figure 4.13.

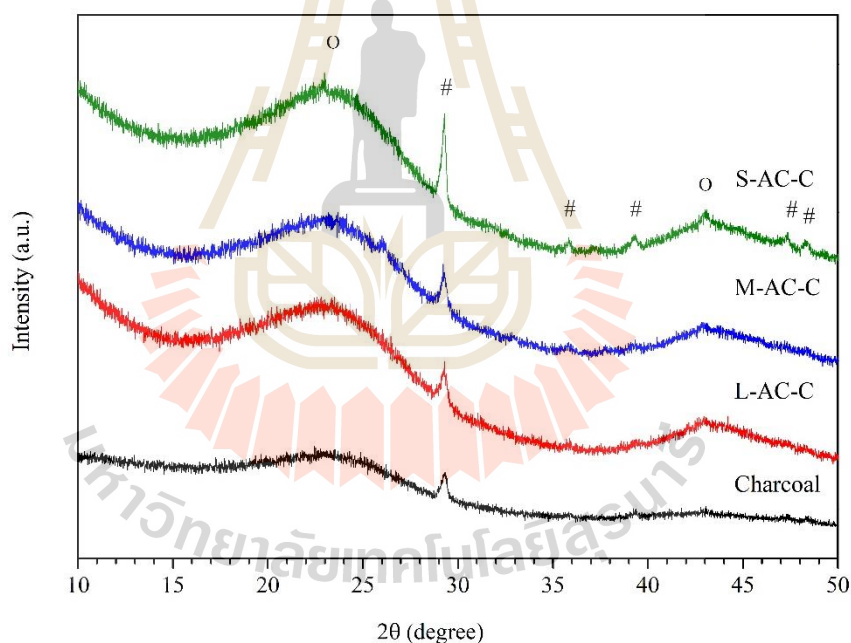


Figure 4.3 XRD patterns of activated carbon by physical activation with different sizes from *L. leucocephala* charcoal.

Main component of activated carbon is shown in Table 4.1. The oxygen content was estimated by difference [100- (% C+ % H+ % N+ %S)]. After the charcoal was activated by carbon dioxide, all samples showed higher carbon content. Activated

carbon from the medium size of charcoal provide the highest carbon content. Percent of product yield was increased from large size to small size but percent burn-off was decreased indicated that the ash coating and activation occur only on the external surface area. Thus, the small size has a BET surface area lower than all of the samples (see in Table 4.2).

Table 4.1 Elemental analysis of charcoal and activated carbon by physical activation at 800°C, 1 h.

Sample	Elemental composition (%)					C/H	Yield (%)	burn-off (%)
	C	H	N	S	O			
Charcoal	76.18	1.899	0.849	0.069	21.00	40.1	-	-
L-AC-C	80.09	1.710	1.049	0.008	17.14	46.8	80.5	19.5
M-AC-C	90.03	0.557	0.367	0.069	8.98	162.1	86.3	13.7
S-AC-C	86.94	1.518	0.961	0.016	10.56	57.3	91.0	9.0

Besides the elemental compositions, percent burn-off were determined by the equation below (Ngernyen et al., 2006).

$$\% \text{ Burn-off} = \frac{(W_0 - W)}{W_0} \times 100$$

Where W_0 is weight of the original charcoal.

W is weight of activated carbon.

Nitrogen sorption isotherms and pore size distributions of all activated carbons are shown in Figure 4.4(a) and (b), respectively. Surface areas and pore

volumes are reported in Table 4.2. All the samples have type I isotherm according to the IUPAC classification indicating that micropores are dominant (Thommes et al., 2015). All activated carbon samples have higher surface areas than the charcoal precursor attributing to an increase of pore volumes. Activated carbon with the highest BET surface area was formed the charcoal with the largest particle size. Micropore diameter and mean pore diameter of all activated carbon was about 0.6 nm and 1.7 nm, respectively.

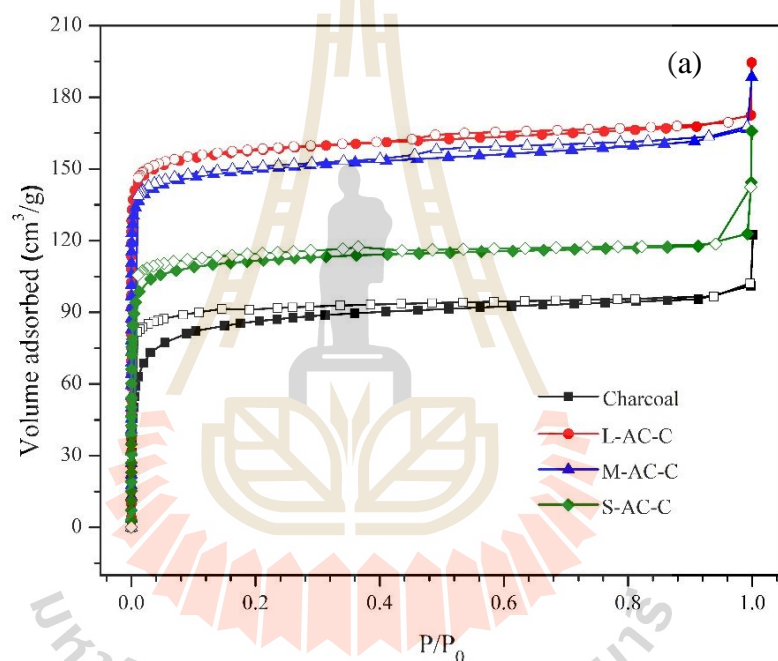


Figure 4.4 (a) Adsorption-desorption isotherms of charcoal and activated carbons; filled: adsorption, empty: desorption.

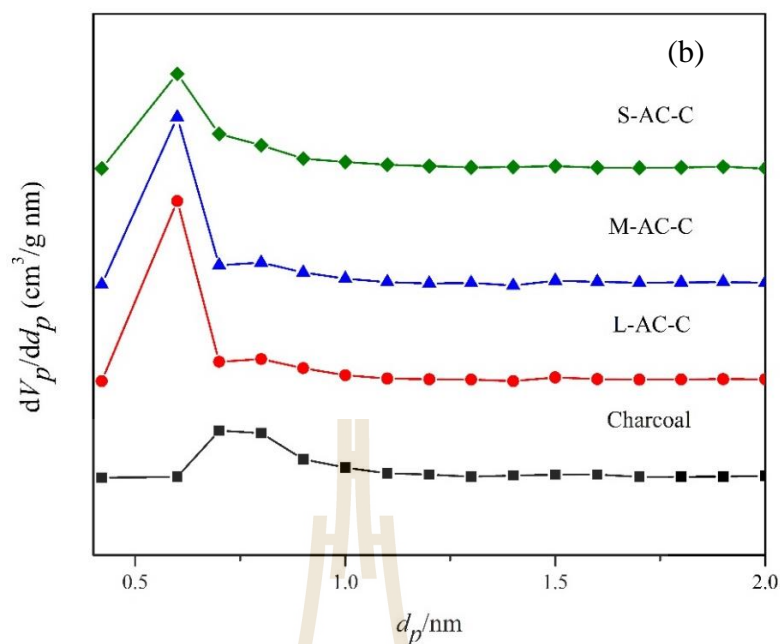


Figure 4.4 (Continued) (b) Pore size distributions of charcoal and activated carbons.

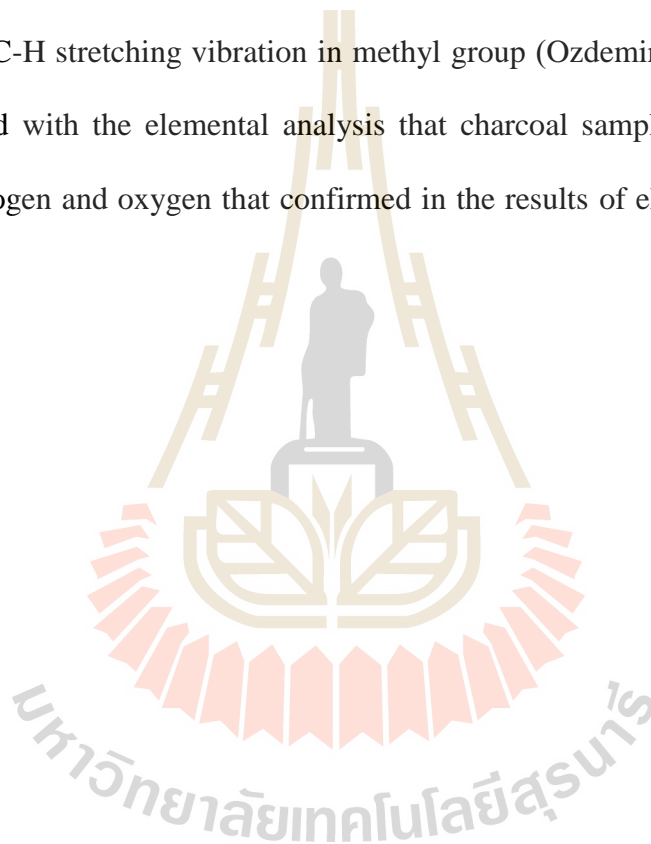
Table 4.2 Nitrogen adsorption-desorption analysis of charcoal and activated carbon.

Sample	$S_{\text{BET}}^{\text{a}}$ (m^2/g)	$V_{\text{micro}}^{\text{b}}$ (cm^3/g)	$V_{\text{meso}}^{\text{c}}$ (cm^3/g)	$V_{\text{total}}^{\text{d}}$ (cm^3/g)	D_{p}^{e} (nm)
Charcoal	329	0.143	0.036	0.156	1.89
L-AC-C	609	0.267	0.034	0.266	1.75
M-AC-C	593	0.253	0.038	0.258	1.74
S-AC-C	431	0.189	0.026	0.190	1.76

Note: a = BET surface area, b = Micropore volume, c = Mesopore volume, d = Total pore volume and e = Mean pore diameter

Figure 4.5 shows FTIR spectra of the charcoal and activated carbon samples. All of the samples have band positions similar to the literature (Ozdemir et al., 2014). The broad band around 3400 cm^{-1} corresponds to -OH stretching vibration of alcohol

and phenol. The bands around 1600 and 1400 cm^{-1} were assigned C=C aromatic ring stretching vibration (Ozdemir et al., 2014). The band in the region of 1300 to 1000 cm^{-1} may be ascribed to C-O in carboxylic acids, alcohols, phenols, ether or ester groups. The peaks between 900 and 650 cm^{-1} were related to C-H out-of-plane bending of aromatic rings. The peak at 878 cm^{-1} can be assigned to isolated H in the aromatic rings (Liu et al., 2016). The small peaks at 2910 and 2820 cm^{-1} in the spectra of L-AC-C represent of C-H stretching vibration in methyl group (Ozdemir et al., 2014). The IR results agreed with the elemental analysis that charcoal samples and activated still contain hydrogen and oxygen that confirmed in the results of elemental analysis (see Table 4.1).



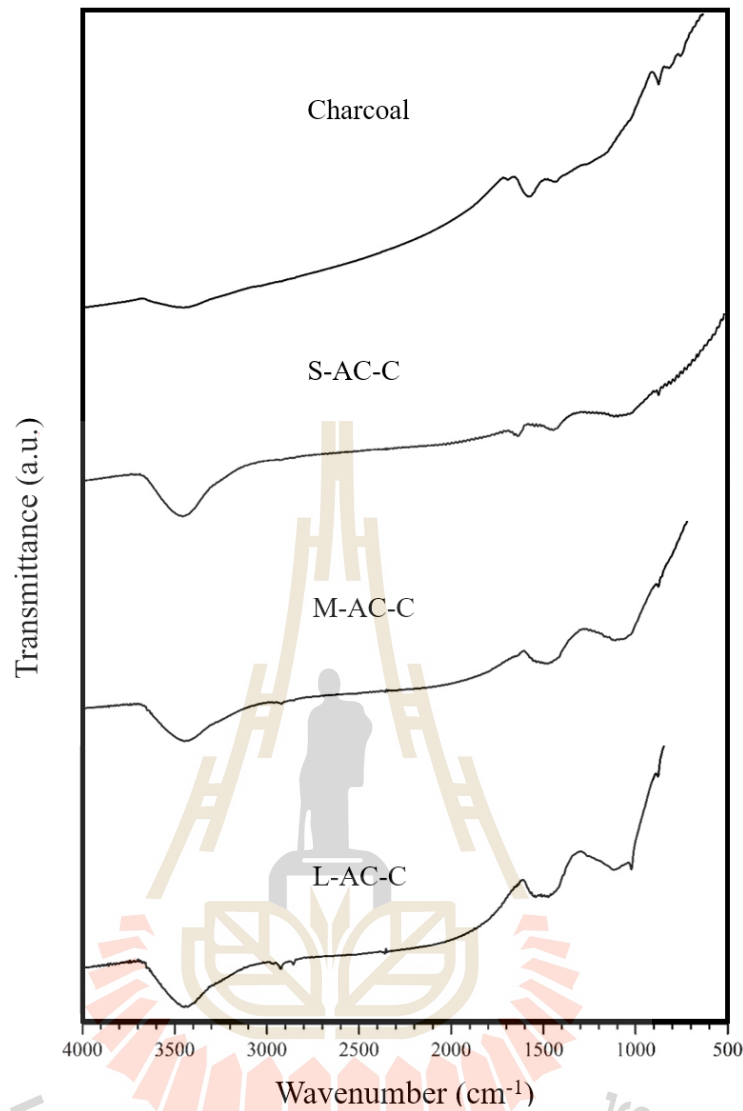


Figure 4.5 FTIR spectra of charcoal and activated carbons of physical method.

Nature of carbon in activated carbons, especially the distribution and state of sp^2 bonded carbon was analyzed by Raman spectroscopy. Figure 4.6 shows Raman spectra of activated carbon samples. The spectra have main characteristic bands including disorder, D-band at 1350 cm^{-1} , and graphite, G-band at 1580 cm^{-1} and 2D-bands at around 2700 cm^{-1} . The G peak was contributed to the C-C band stretching of all pairs of sp^2 atoms in the both rings and chains. Thus, the G peak is the main Raman

signature for sp^2 carbon. the D band was attributed to in-plane vibrations of sp^2 bonded carbon within structural defects (Rhim et al., 2010). All of the samples show band shift of D, G and 2D confirming that they contain graphitic carbon. the weak intensities indicate poor crystallinity, consistent with the XRD.

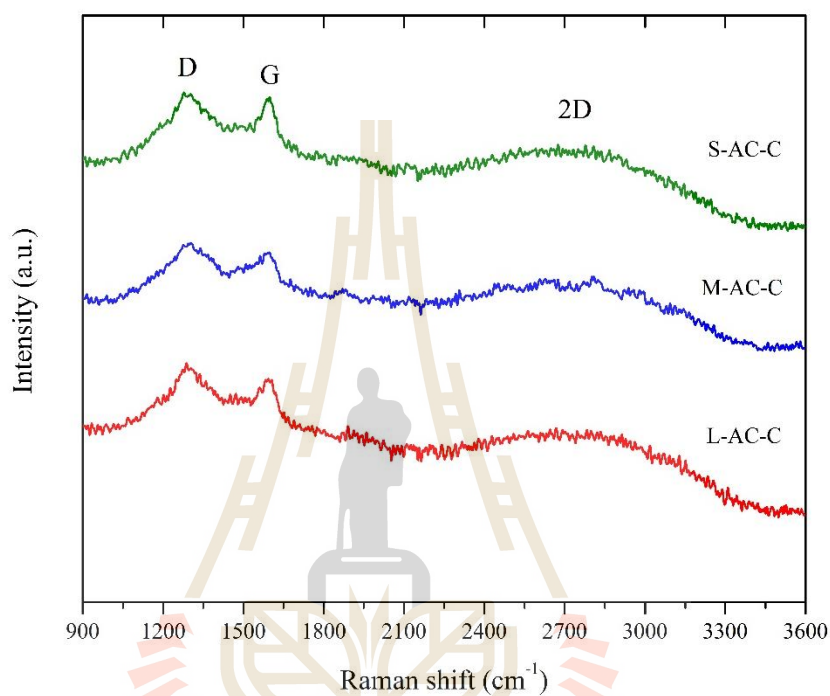


Figure 4.6 Raman spectra of activated carbon.

4.4.2 Characterization of activated carbon from chemical activation

After pyrolysis, the pores were generated. Figure 4.7 displays the SEM images of charcoal from *L. leucocephala* wood and activated carbons. The majority of pores from all samples were macropores with diameter around 2-5 μm . Some of the pores were partially blocked by some non-uniform particles. Moreover, larger pore with diameter about 10-20 μm were observed. The wall of those pores also consists of mesopores with diameter around 2 nm (see in Table 4.4). After activation, the pore structures were similar to charcoal sample.

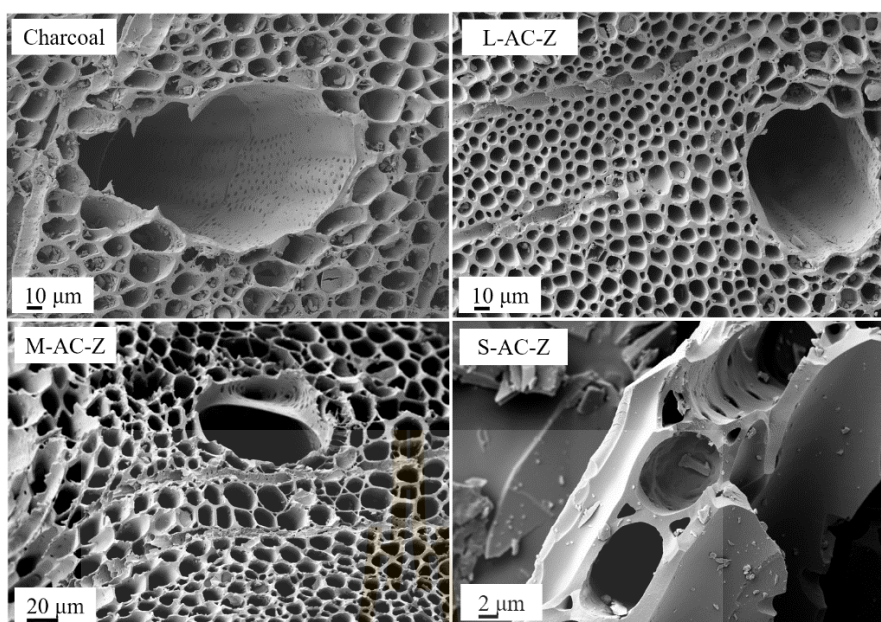


Figure 4.7 SEM images of charcoal and activated carbons with different sizes preparation by chemical activation (ZnCl_2) at 800°C for 1 h.

Figure 4.8 shows the XRD patterns of charcoal and activated carbon with different sizes as note as L-AC-Z, M-AC-Z and S-AC-Z which prepared by chemical method with ZnCl_2 . In case of activated carbon, only graphitic carbon peak were observed. Two broad diffraction peaks of graphitic-type lattice (\circ) occurred at the same position of $2\theta = 24$ and 43° (Xu et al., 2014), but the calcium carbonate peak ($\#$) did not occur indicating that the calcium carbonate can be dissolved in dilute HCl and leached from the pore of activated carbon. It should be indicated that high efficiency of chemical reagent can be completely generated porous carbon materials.

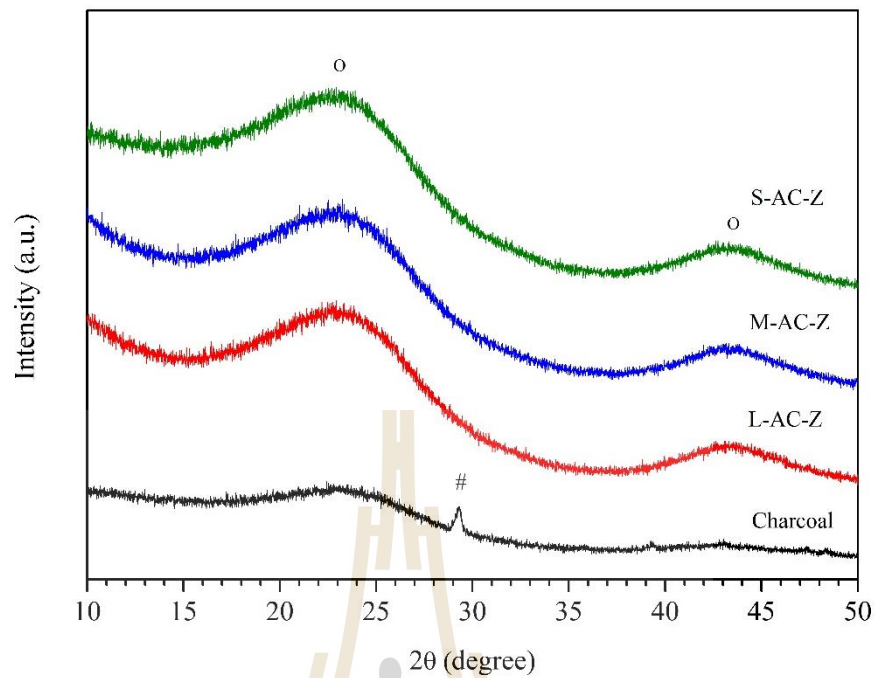


Figure 4.8 XRD patterns of charcoal and activated carbon by chemical activation.

Table 4.3, after activation, all samples show higher carbon contents. Activated carbon from the medium size of charcoal provide the highest carbon content. Percent of product yield of L-AC-Z, M-AC-Z and S-AC-Z slightly decreased and percent burn-off increased. For this method, the size is not significant, and high activating temperature is not suitable for chemical activation because of the lower BET surface area (see in Table 4.4). Normally, the chemical activation was used in the low activation temperature at 500-700°C (Ozdemir et al., 2014).

Table 4.3 Elemental analysis of activated carbon produced by chemical activation at 800°C for 1 h.

Sample	Elemental composition (%)					C/H	Yield (%)	burn-off (%)
	C	H	N	S	O			
Charcoal	76.18	1.899	0.849	0.069	21.00	40.1	-	-
L-AC-Z	84.06	1.781	1.082	-	13.08	47.2	81.1	18.9
M-AC-Z	93.01	1.705	1.480	0.003	3.80	54.6	77.0	23.0
S-AC-Z	78.12	1.342	1.117	0.013	19.41	58.1	76.5	23.5

Adsorption isotherms and pore size distributions of the charcoal and activated carbons are shown in Figure 4.9(a) and (b), respectively. All the samples are type I isotherm according to the IUPAC classification indicating that micropores is dominant (Moreno-Piraján et al., 2010). Activating temperatures and particle sizes have effect for physical activation (see Figure 4.4(a)) more than chemical activation (see Figure 4.9(a)). Pore size distributions of all samples in Figure 4.9(b) shows non-uniform micropores diameter.

Surface areas, pore sizes and pore volumes of all samples displayed in Table 4.4. All activated carbons have higher surface area than the charcoal precursor due to increase micropores and total pore volumes. The activated carbon has similar or lower mesopore surface area confirming that micropores was dominant of all samples.

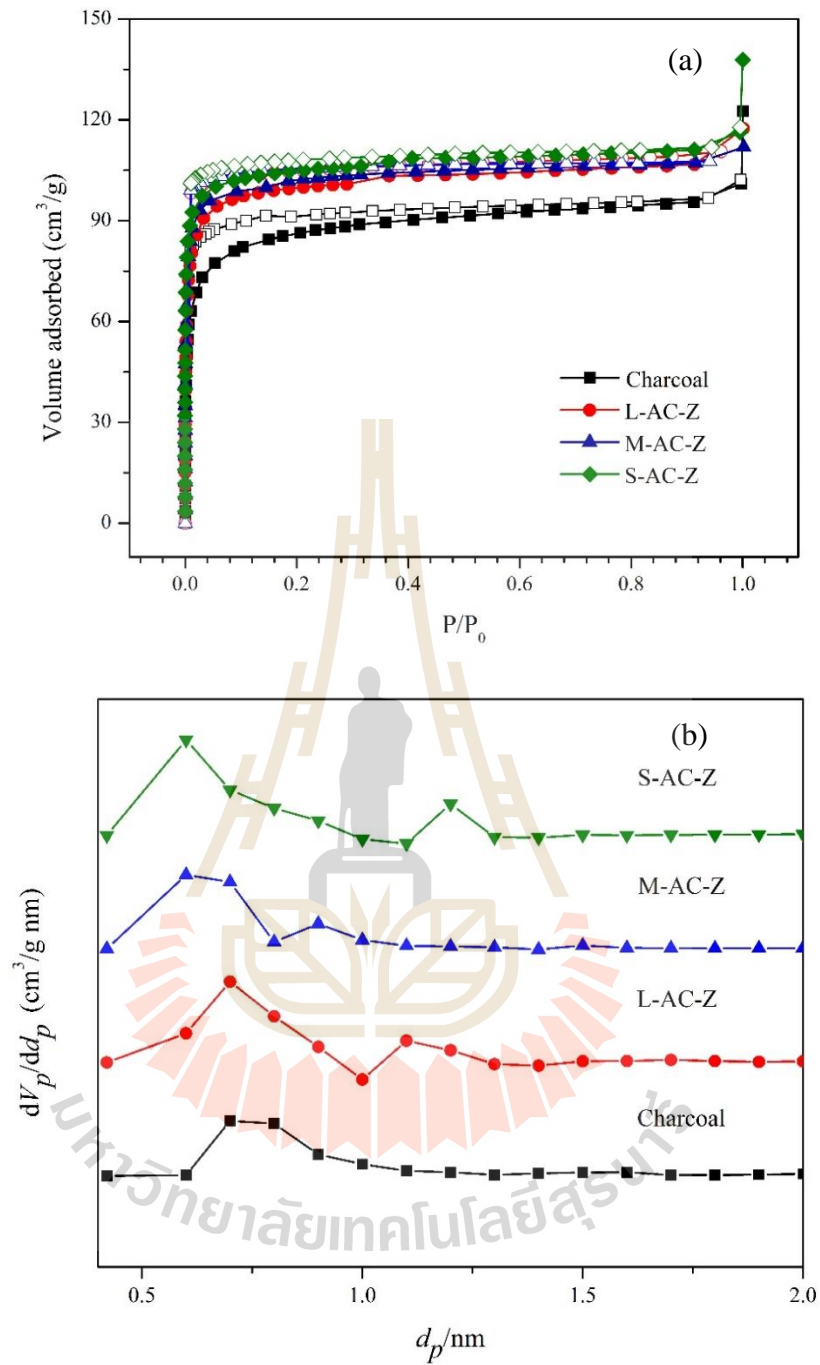


Figure 4.9 (a) Nitrogen adsorption-desorption isotherms, (b) pore size distributions of charcoal and activated carbons; filled: adsorption, empty: desorption.

Table 4.4 Nitrogen adsorption-desorption analysis of activated carbon.

Sample	$S_{\text{BET}}^{\text{a}}$ (m^2/g)	$V_{\text{micro}}^{\text{b}}$ (cm^3/g)	$V_{\text{meso}}^{\text{c}}$ (cm^3/g)	$V_{\text{total}}^{\text{d}}$ (cm^3/g)	D_{p}^{e} (nm)
L-AC-Z	387	0.170	0.034	0.180	1.85
M-AC-Z	395	0.173	0.024	0.172	1.74
S-AC-Z	409	0.178	0.026	0.180	1.75

Note: a = BET surface area, b = Micropore volume, c = Mesopore volume, d = Total pore volume and e = Mean pore diameter

Figure 4.10 shows FTIR spectra of the charcoal and activated carbon samples which activation by chemical method. All of the samples have band positions similar to the results of physical activation (see Figure 4.5). The broad band around 3400 cm^{-1} corresponds to -OH stretching, the small peaks at 2910 and 2820 cm^{-1} represent of C-H stretching, the bands around 1600 and 1400 cm^{-1} of C=C aromatic ring stretching vibration (Ozdemir et al., 2014). The band in the region of 1300 to 1000 cm^{-1} may be ascribed to C-O and the peaks between 900 and 650 cm^{-1} were related to C-H out-of-plane bending of aromatic rings. The IR results agreed with the elemental analysis that charcoal samples and activated still contain hydrogen and oxygen that confirmed in the results of elemental analysis (see Table 4.3).

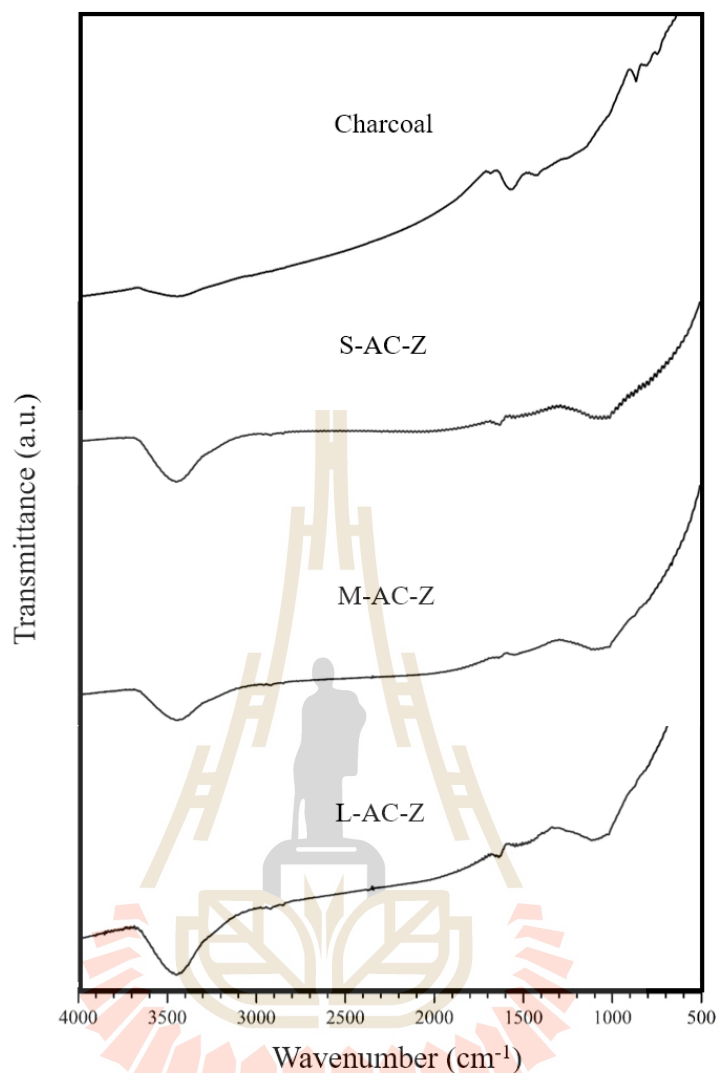


Figure 4.10 FTIR spectra of charcoal and activated carbons of chemical method.

Nature of carbon in activated carbons was analyzed by Raman spectroscopy. Spectra of graphite materials have three main characteristic bands including D-band at 1350 cm^{-1} , G-band at 1580 cm^{-1} and 2D-bands at around 2700 cm^{-1} . Figure 4.11 shows the Raman spectra of activated carbon. All of the samples show D-bands, G-band and 2D-band indicating that the defects and types of graphitic structure (Shimodaira and Masui, 2002). The intensity of band ratio depended on graphitization to porous carbon.

From the results related to XRD patterns that confirmed the graphite occurs after the activation.

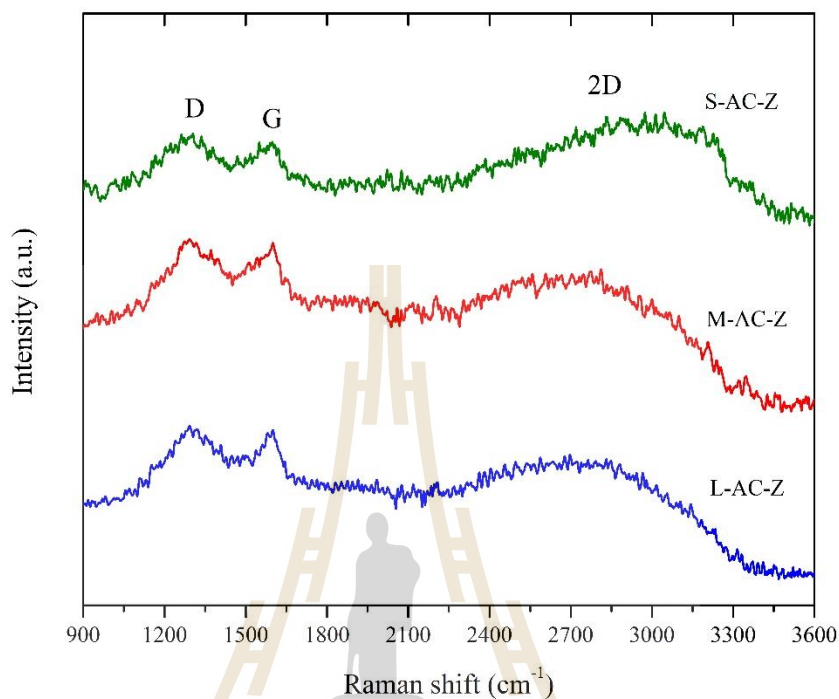


Figure 4.11 Raman spectra of activated carbon.

4.4.3 Characterization of activated carbon by various activation temperature

From the results, the medium size of charcoal and physical activation were chosen for a further study because it gave the highest carbon content and easier preparation. The effect of activation temperature was studied by varying the activation temperature from 600 to 800°C and charcoal provided from Iwasaki kiln and tube furnace.

Figure 4.12(a) and (b) show the XRD patterns of charcoal and activated carbon from various activation temperatures that charcoal provided from Iwasaki kiln and tube furnace. Peaks of graphitic carbon (○) were observed at $2\theta = 24$ and 43° . Peaks of calcium carbonate, CaCO_3 (#) and calcium oxide, CaO (*) were observed at

$2\theta = 29.3$ and 36.7° , respectively. Figure 4.12(a), charcoal provided from Iwasaki kiln shows the weakest intensity of CaCO_3 peak at high temperature of 800°C in the sample of AC800IW. It was possible that CaCO_3 decomposed to CaO when increasing the temperature (Viriya-empikul et al., 2012). The decomposition of CaCO_3 can be proposed in a reaction below. Figure 4.12(b) also shows the XRD patterns of AC800TF, charcoal provided from a tube furnace and activation at 800°C . The result has similar in Figure 4.12(a).

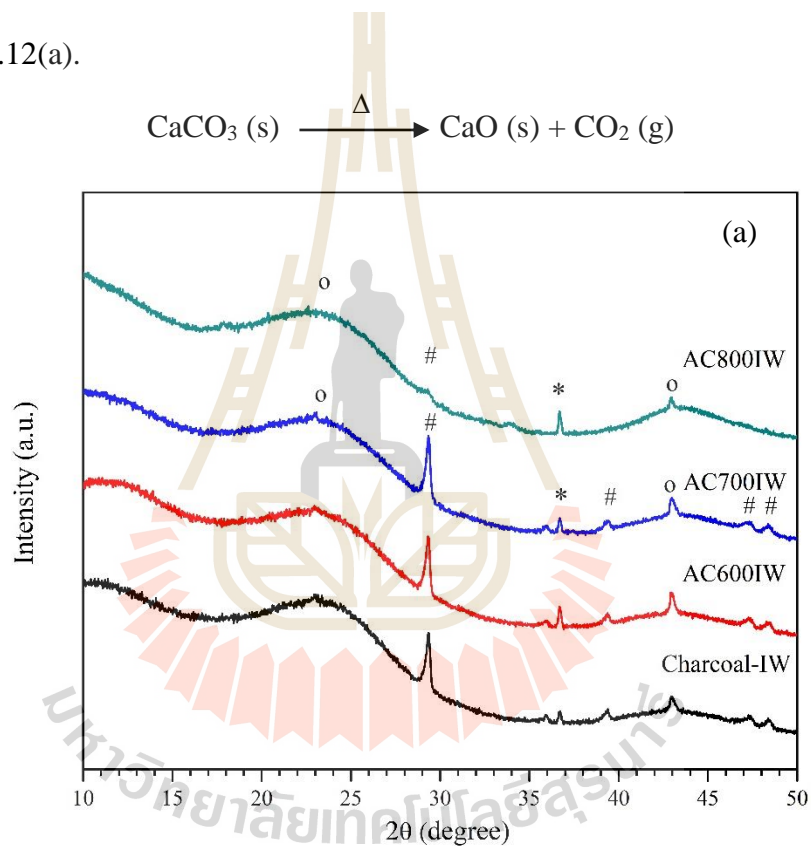


Figure 4.12 XRD patterns of activated carbon with charcoal from (a) Iwasaki kiln with various activating temperature for 1 h.

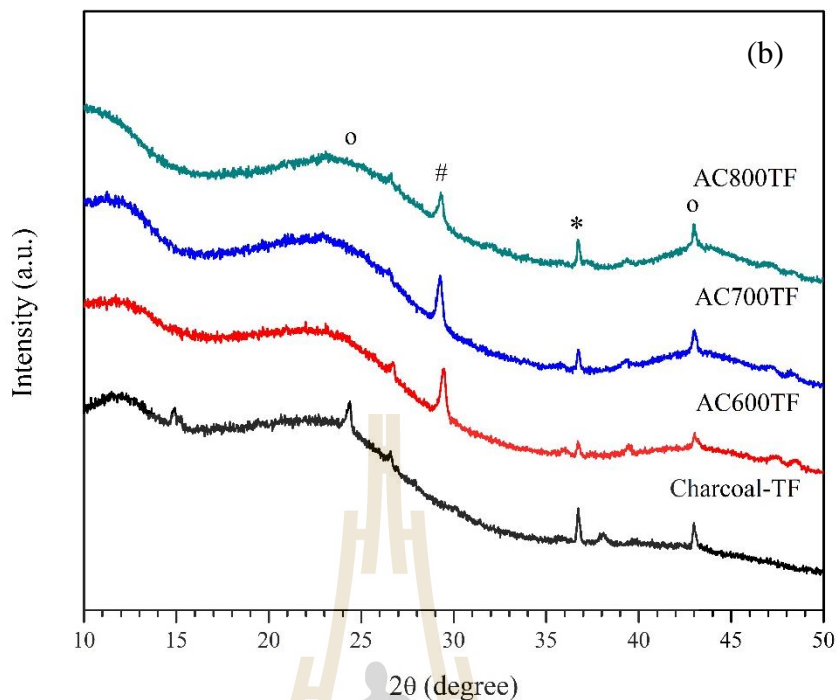


Figure 4.12 (Continued) XRD patterns of activated carbon with charcoal from (b) tube furnace with various activating temperature for 1 h.

Figure 4.13(a) to (d) shows morphology of the charcoal (from Iwasaki kiln) and activated carbons. At low activating temperature, the pore is not clear that has remained calcium carbonate species. The compositions was confirmed by SEM-EDX (see Figure 4.13(e) and (f)). TEM image of activated carbon (AC800IW) displayed clearly carbon sheet as shown in Figure 4.13(g) and (h). Figure 4.14(a) to (d) shows the SEM images of charcoal and activated carbon, production in a tube furnace. For the result shows clear pore and uniform porous structure indicating that high BET surfaces area (see Table 4.6).

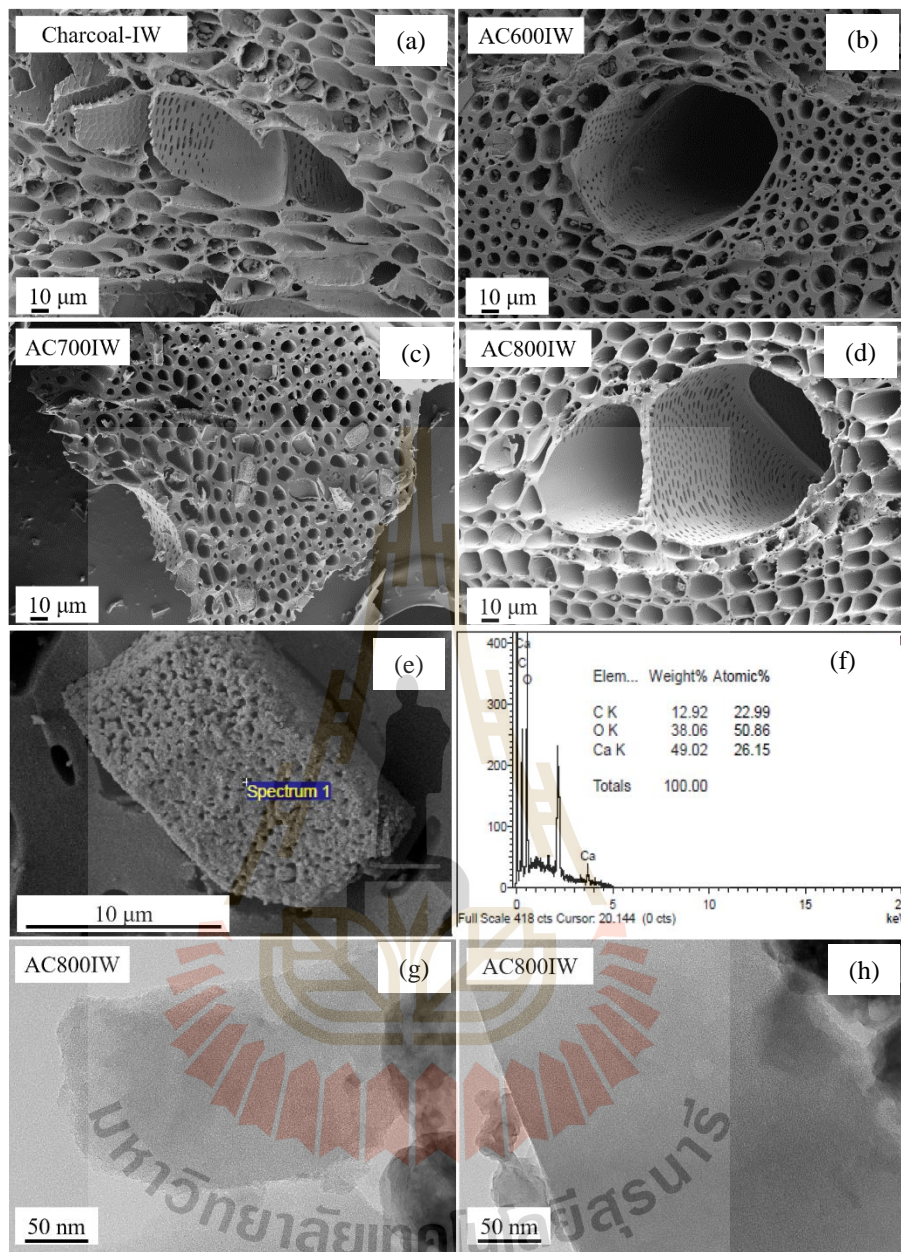


Figure 4.13 SEM images of (a) charcoal, (b to d) activated carbon, (e, f) its EDX composition, (g, h) TEM images of AC800IW.

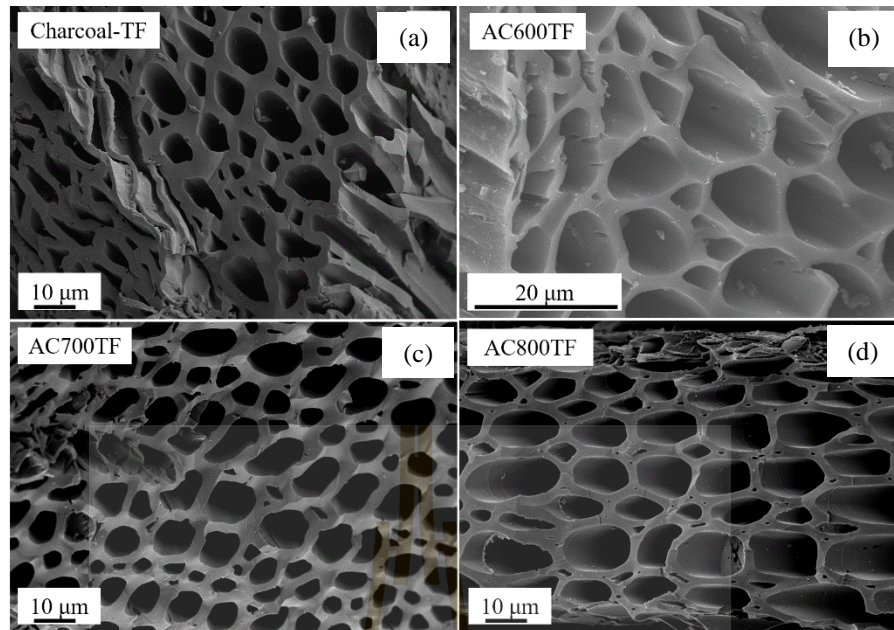


Figure 4.14 SEM images of (a) charcoal (from a tube furnace), (b-d) activated carbon.

The elemental analysis of sample from Iwasaki kiln and tube furnace are shown in Table 4.5. Both samples have high carbon content, suitable as a starting materials for activated carbon. After activation, the obtained activated carbons have higher carbon content than the charcoals precursor. The activated carbons have high carbon contents indicating that high temperature and long-time carbonization could intensify graphitization (Hou et al., 2015).

Table 4.5 The elemental composition of activated carbon.

Samples	Elemental composition (%)					C/H
	C	H	N	S	O	
Charcoal-IW	76.18	1.899	0.849	0.069	21.00	40.1
AC600IW	81.37	1.734	0.968	0.072	15.86	46.9
AC700IW	83.57	1.012	1.114	0.076	14.23	82.6
AC800IW	90.03	0.557	0.367	0.069	8.98	161.6
Charcoal-TF	71.09	3.651	0.571	0.065	24.62	19.4
AC600TF	80.55	2.181	0.731	0.069	16.47	36.9
AC700TF	82.58	1.367	0.869	0.071	15.11	60.4
AC800TF	80.71	1.146	1.094	0.078	16.97	70.4

Table 4.6 shows the physical properties of charcoal and activated carbon preparation by physical activation. The charcoal from Iwasaki kiln has higher BET surface area (S_{BET}), micropore volume (V_{micro}), mesopore volume (V_{meso}), and total pore volume (V_{total}) than the charcoal from tube furnace because of high temperature and long-time carbonization under oxygen-lean in environment. For the activated carbon, the results from nitrogen adsorption-desorption increased with increasing the activating temperatures indicating that the gasification of carbon dioxide and carbon was occurred and generated the micropore volume and surface area (Ngernyen et al., 2006). In contrast, when increasing the temperature, the product yield decreased corresponding to percent burn-off increased. The percent burn-off for the samples of AC600IW, AC700IW and AC800IW was 5.9%, 11.5% and 22.5%, respectively, related to decreasing product yield of 94.1%, 88.5% and 77.5%, respectively. For the samples of

AC600TF, AC700TF and AC800TF have percent burn-off such as 27.7%, 28.6% and 51.3%, respectively, and product yield was 72.3%, 71.3% and 48.7%, respectively. However, both charcoals from Iwasaki kiln and tube furnace produced activated carbon with high carbon content.

Table 4.6 Adsorption analysis of charcoal and activated carbon by physical activation.

Sample	S_{BET} (m^2/g)	V_{micro} (cm^3/g)	V_{meso} (cm^3/g)	V_{total} (cm^3/g)	D_p (nm)
Charcoal-IW	329	0.143	0.036	0.156	1.89
AC600IW	332	0.136	0.009	0.145	1.23
AC700IW	374	0.171	0.048	0.181	1.94
AC800IW	593	0.253	0.038	0.258	1.74
Charcoal-TF	3	0.001	0.010	0.010	14.36
AC600TF	464	0.199	0.032	0.203	1.75
AC700TF	535	0.233	0.035	0.232	1.73
AC800TF	935	0.408	0.083	0.421	1.80

Note: a = BET surface area, b = Micropore volume, c = Mesopore volume, d = Total pore volume and e = Mean pore diameter

Figure 4.15(a) and (b) shows the isotherms of charcoal and activated carbon that are the characteristic of isotherm type I. At a high activation temperature, sample AC800IW and AC800TF has high intensity of nitrogen adsorption. However, the samples-IW from activation temperature lower than 800°C did not provide clear isotherms, especially in the sample of AC600IW probably from calcium species which

filled the pore after pyrolysis (see EDX in Figure 4.13(e)). In contrast, all of the samples-TF show high intensity of nitrogen adsorption and micropore diameter was around 0.6 nm. The production of charcoal-TF was pretreated under nitrogen gas and activated with carbon dioxide that showed clearly the pore, high surface area and high carbon contents.

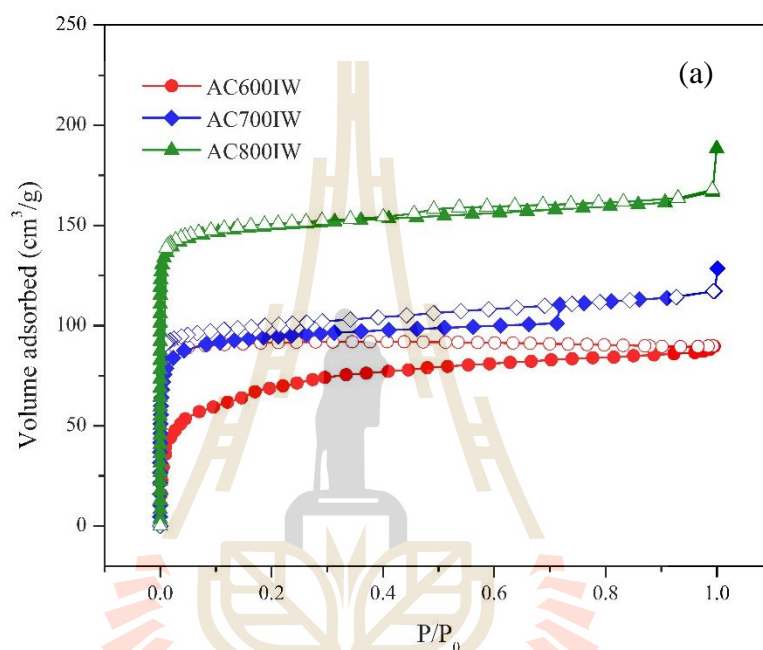


Figure 4.15 Adsorption isotherms of (a) activated carbon from charcoal in Iwasaki kiln; filled: adsorption, empty: desorption.

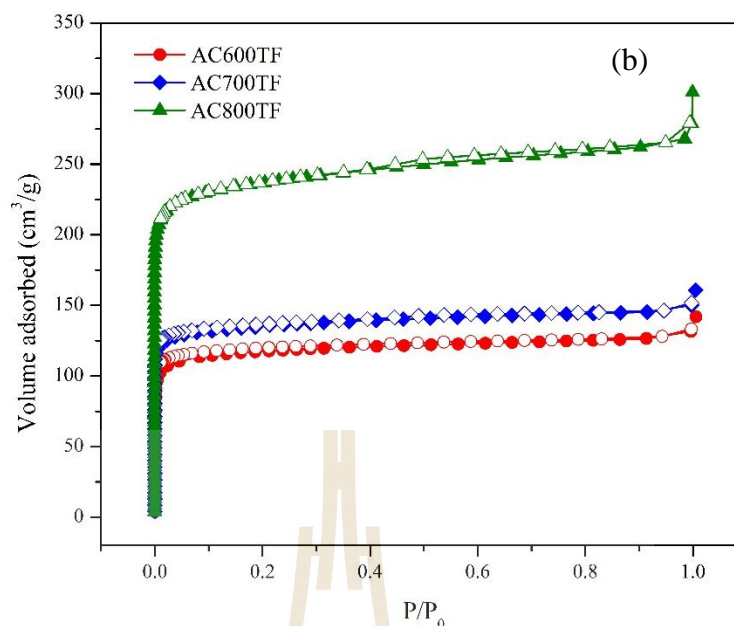


Figure 4.15 (Continued) Adsorption isotherms of (b) charcoal in a tube furnace; filled: adsorption, empty: desorption.

4.5 Conclusions

Charcoals of *L. leucocephala* wood were produced from tube furnace and Iwasaki kiln and used for the preparation of activated carbons by physical and chemical activation with carbon dioxide and ZnCl_2 , respectively. The activated carbon from tube furnace charcoal gave higher S_{BET} , V_{micro} , V_{meso} , V_{total} than that from the charcoal from tube furnace. However, the activated carbon from Iwasaki kiln charcoal has higher carbon contents than activated carbon from the charcoal from tube furnace. The AC800TF gave the maximum surface area and total pore volume of $935 \text{ m}^2/\text{g}$ and $0.421 \text{ cm}^3/\text{g}$, respectively. Both of AC800IW and AC800TF could be used as catalyst supports.

4.6 References

- Açıkyıldız, M., Gürses, A., and Karaca, S. (2014). Preparation and characterization of activated carbon from plant wastes with chemical activation. **Microporous and Mesoporous Materials**. 198: 45-49.
- Angın, D., Altıntig, E., and Köse, T. E. (2013). Influence of process parameters on the surface and chemical properties of activated carbon obtained from biochar by chemical activation. **Bioresource Technology**. 148: 542-549.
- Cheng, S., Wei, L., Zhao, X., Kadis, E., Cao, Y., Julson, J., and Gu, Z. (2016). Hydrodeoxygenation of prairie cordgrass bio-oil over Ni based activated carbon synergistic catalysts combined with different metals. **New Biotechnology**. 33(4): 440-448.
- Heibati, B., Rodriguez-Couto, S., Al-Ghouti, M. A., Asif, M., Tyagi, I., Agarwal, S., and Gupta, V. K. (2015). Kinetics and thermodynamics of enhanced adsorption of the dye AR 18 using activated carbons prepared from walnut and poplar woods. **Journal of Molecular Liquids**. 208: 99-105.
- Hou, C. H., Liu, N. L., and Hsi, H. C. (2015). Highly porous activated carbons from resource-recovered *Leucaena leucocephala* wood as capacitive deionization electrodes. **Chemosphere**. 141: 71-79.
- Jambulingam, M., Karthikeyan, S., Sivakumar, P., Kiruthika, J., and Maiyalagan, T. (2007). Characteristic studies of some activated carbons from agricultural wastes. **Journal of Scientific and Industrial Research**. 66: 495-500.
- Liu, Z., Huang, Y., and Zhao, G. (2016). Preparation and characterization of activated carbon fibers from liquefied wood by ZnCl₂ activation. **BioResources**. 11(2): 3178-3190.

- Mahmoud, D. K., Salleh, M. A. M., Karim, A. W. A., and Idris, A. (2014). Utilization of *Leucaena leucocephala* wood char as bioenergy by-product for methylene blue adsorption: Production, characterization and application. **Journal of Advanced Science and Engineering Research**. 4(4): 204-211.
- Moreno-Piraján, J. C., Tirano, J., Salamanca, B., and Giraldo, L. (2010). Activated carbon modified with copper for adsorption of propanethiol. **International Journal of Molecular Sciences**. 11(3): 927-942.
- Ngernyen, Y., Tangsathitkulchai, C., and Tangsathitkulchai, M. (2006). Porous properties of activated carbon produced from Eucalyptus and wattle wood by carbon dioxide activation. **Korean Journal of Chemical Engineering**. 23(6): 1046-1054.
- Ozdemir, I., Şahin, M., Orhan, R., and Erdem, M. (2014). Preparation and characterization of activated carbon from grape stalk by zinc chloride activation. **Fuel Processing Technology**. 125: 200-206.
- Raveendran, K., Ganesh, A., and Khilar, K. C. (1995). Influence of mineral matter on biomass pyrolysis characteristics. **Fuel**. 74(12): 1812-1822.
- Rhim, Y. R., Zhang, D., Fairbrother, D. H., Wepasnick, K. A., Livi, K. J., Bodnar, R. J., and Nagle, D. C. (2010). Changes in electrical and microstructural properties of microcrystalline cellulose as function of carbonization temperature. **Carbon**. 48(4): 1012-1024.
- Sahu, J. N., Acharya, J., and Meikap, B. C. (2010). Optimization of production conditions for activated carbons from Tamarind wood by zinc chloride using response surface methodology. **Bioresource Technology**. 101(6): 1974-1982.

- Shimodaira, N., and Masui, A. (2002). Raman spectroscopic investigations of activated carbon materials. **Journal of Applied Physics**. 92(2): 902-909.
- Thommes, M., Kaneko, K., Neimark, A. V., Olivier, J. P., Rodriguez-Reinoso, F., Rouquerol, J., and Sing, K. S. (2015). Physisorption of gases, with special reference to the evaluation of surface area and pore size distribution (IUPAC Technical Report). **Pure and Applied Chemistry**. 87(9-10): 1051-1069.
- Viriya-empikul, N., Krasae, P., Nualpaeng, W., Yoosuk, B., and Faungnawakij, K., 2012. Biodiesel production over Ca-based solid catalysts derived from industrial wastes. **Fuel**. 92(1): 239-244.
- Xin, H., Guo, K., Li, D., Yang, H., and Hu, C. (2016). Production of high-grade diesel from palmitic acid over activated carbon-supported nickel phosphide catalysts. **Applied Catalysis B: Environmental**. 187: 375-385.
- Xu, J., Gao, Q., Zhang, Y., Tan, Y., Tian, W., Zhu, L., and Jiang, L. (2014). Preparing two-dimensional microporous carbon from pistachio nutshell with high areal capacitance as supercapacitor materials. **Scientific Reports**. 4: 5545.

CHAPTER V

HYDRODEOXYGENATION OF PALM OIL TO BIO-HYDROGENATED DIESEL (BHD) PRODUCT OVER METAL PHOSPHIDES

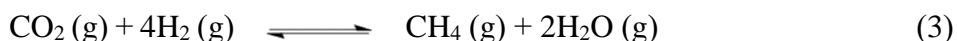
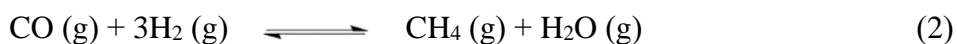
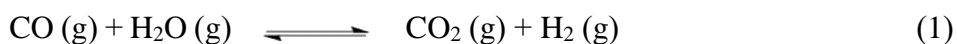
5.1 Abstract

Palm oil can be used as a feedstock to produce renewable transportation biofuel through hydrodeoxygenation (HDO) which is an elimination of oxygen by cleavage of C-O bond under H₂ atmosphere. This process produces the second generation biofuel known as bio-hydrogenated diesel (BHD). In this work, HDO of palm oil over phosphides of Ni, Co and Cu was investigated. Physicochemical properties of the catalysts were studied by scanning electron microscopy (SEM), X-ray diffraction (XRD) and X-ray absorption near edge structure (XANES) spectroscopy. From the result, the reduction temperature of 650°C was optimal to completely convert metal phosphate to metal phosphide. The optimum condition for catalytic testing was at 380°C under H₂ atmosphere of 50 bar for the contact time 6 h in a continuous fixed-bed flow reactor. The catalytic activity of the phosphides was in the order: Ni > Co > Cu. The major products were straight chain alkanes with selectivity toward C₁₅-C₁₈. The catalyst with a mixed phase of Ni₂P and Ni₁₂P₅ showed favorable selectivity to BHD products.

5.2 Introduction

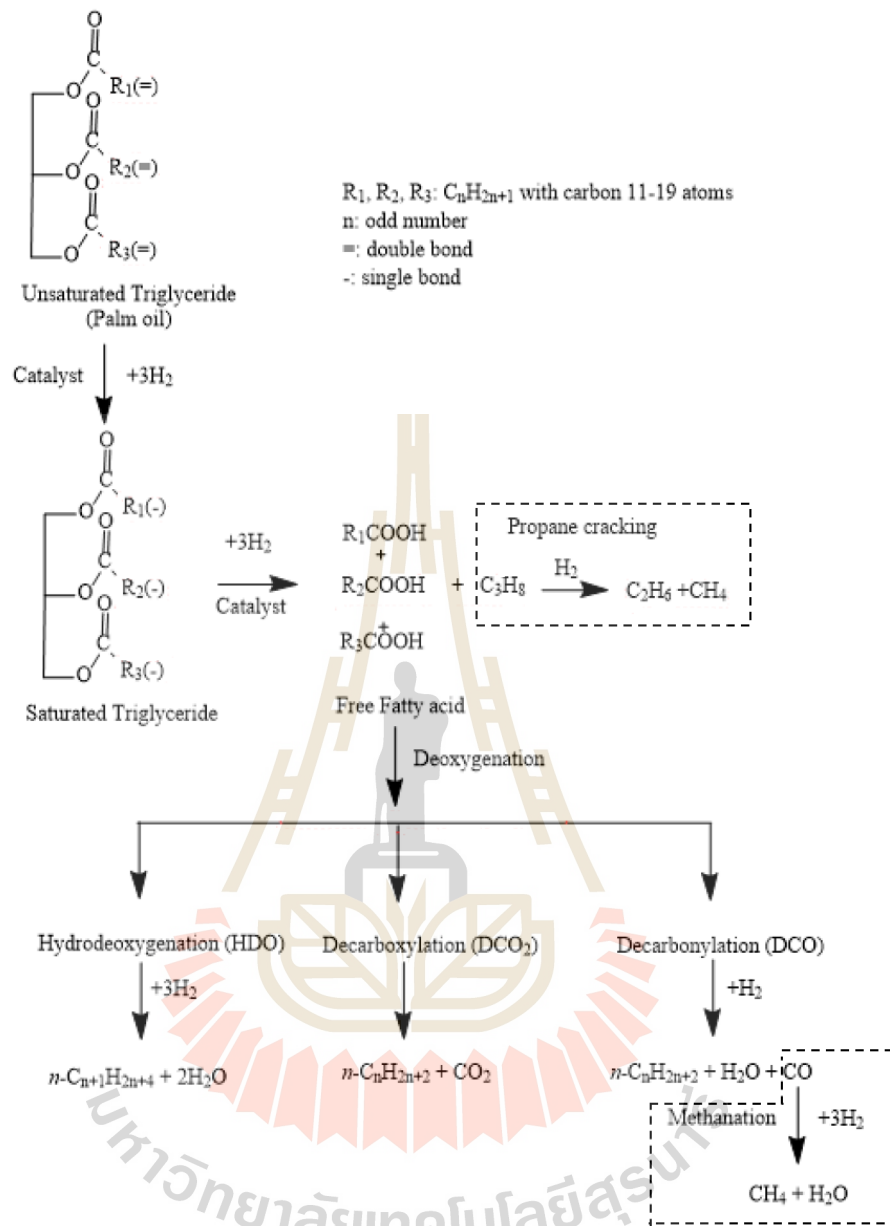
As a demand for fossil fuel is increasing, biofuel has an important role as a renewable feedstock for the production of green-diesel or bio-hydrogenated diesel (BHD) via hydrodeoxygenation (HDO). This reaction removes oxygenated part from a molecule and improves the properties of biodiesel from high oxygen content, high cloud point, high viscosity, increasing of NO_x emissions, low heating value and corrosion of metal engine (Phimsen et al., 2017) to high cetane number, high thermal and oxidation stability (Mikkonen et al., 2008). Scheme 5.1 shows proposed reaction pathways of palm oil or unsaturated triglyceride (TG) that are converted to BHD through hydrodeoxygenation under H_2 atmosphere in the presence of heterogeneous catalysts. In the reaction, double bonds of the unsaturated triglycerides are converted to saturated triglyceride by hydrogenation. Hydrogenolysis of saturated triglycerides produces free fatty acids and propane (C_3H_8) as an initial primary product that could be changed to ethane (C_2H_6) and methane (CH_4). Then, the oxygen is removed from a molecule of free fatty acids via deoxygenation, through three competition reactions of hydrodeoxygenation (HDO), decarbonylation (DCO) and decarboxylation (DCO_2). HDO is the primary H_2 consumption pathway which produces *n*-alkane with the same number of carbon as the feedstock and water as a by-product via C-O bond cleavage. Both DCO and DCO_2 pathways produce *n*-alkane via C-C bond cleavage leading to loss of carbon atom as CO gas and water (from DCO) and CO_2 (from DCO_2) (Itthibenchapong et al., 2017; Srifa et al., 2014; Xin et al., 2016). The DCO pathway uses less H_2 than HDO but the CO product could further react with hydrogen to produce methane and water. Moreover, CO could react with water to produce CO_2 and H_2 (Equation 1). In contrast, the DCO_2 route does not require H_2 . Other possible reactions

with the excess H_2 in the reaction system were water gas shift (Equation (1)) and methanation (Equation (2) and (3)) (Phimsen et al., 2017).



Nickel- and cobalt-molybdenum sulfides are the conventional hydrotreating catalysts for deoxygenation of triglyceride to BHD (Itthibenchapong et al., 2017; Srifa et al., 2014). However, the toxicity of sulfide in the products could cause problems to organism and environment. The favorable metal catalysts for the hydrotreating activity are noble metal such as Pd, Pt, Rh and Ru, but the high price is the main limitation in industrial applications (Phimsen et al., 2017). Thus, developing low cost Ni-based non-sulfide catalysts is interesting approach. Nickel phosphide (NiP) is another active form for deoxygenation of several model compounds such as methyl oleate (Yang et al., 2012), palmitic acid (Xin et al., 2016) and methyl palmitate (Guan et al., 2016). Nickel phosphide offered the lower activities of cracking and methanation when compared with metallic nickel due to the effects of P-ligand with acid sites and enhancement in electronic properties (Yang et al., 2012). All of previous nickel phosphide catalysts on supports were prepared by impregnation method. There is not much work on unsupported catalysts.

In this work, phosphides of Ni, Co and Cu were prepared by precipitation method without a support. This was a new innovation for testing the HDO reaction of palm oil to produce a high quality BHD. The results can illustrate the efficient activity of only metal phosphide for HDO reaction.



Scheme 5.1 Proposed pathways to convert palm oil to bio-hydrogenated diesel (BHD) via deoxygenation (modified from Itthibenchapong et al., 2017; Srifa et al., 2014).

5.3 Experimental

5.3.1 Preparation of metal phosphides for catalysts scanning in HDO reaction

Metal phosphide catalysts were synthesized by a method modified from the literature (Khemthong et al., 2012) using phosphoric acid (H_3PO_4 , Sigma-Aldrich, 85%) and the following precursors: nickel(II) carbonate basic ($\text{NiCO}_3 \cdot 2\text{Ni}(\text{OH})_2 \cdot n\text{H}_2\text{O}$, Carlo Erba, 45% (Ni)), copper(II) carbonate basic ($\text{CuCO}_3 \cdot \text{Cu}(\text{OH})_2 \cdot n\text{H}_2\text{O}$, Carlo Erba, $53 \pm 57\%$ (Cu)) and cobalt(II) carbonate hydrate ($\text{CoCO}_3 \cdot n\text{H}_2\text{O}$, ACROS, 45.5% (Co)). The mole ratio of metal to phosphorus in all catalysts was 0.5. Acetone ($\text{C}_3\text{H}_6\text{O}$, Sigma-Aldrich, 99.5%) was used as a precipitating agent.

Nickel catalyst was prepared by precipitation method. One gram of the metal precursor was dissolved in 3 ml of 70%v/v H_3PO_4 and stirred for 2 h until the bubbles disappear. Then, 30 ml of acetone was added within approximately 2 min into the solution under magnetic stirring (500 rpm) for 1 h. The mixture became two layers and the desired precipitated product was in the bottom layer. The mixture was filtered, washed with acetone several times, oven-dried at 80°C for 5 h and calcined at 500°C for 3 h. This sample was named “calcined sample”. The cobalt and copper catalysts were prepared with the same procedure.

5.3.2 Catalyst characterization

The morphology of reduced catalysts was analyzed by scanning electron microscopy (SEM, JEOL model JSM-6400). Phase of samples was studied by X-ray diffraction (XRD) on a Bruker AXS D8 diffractometer using Ni filtered Cu K_α radiation with at 40 kV and 40 mA with a step increment of 0.02 degree and step time of 0.5 s. Crystal sizes were calculated from Scherrer equation:

$$D = \frac{K\lambda}{\beta \cos \theta}$$

Where D is the mean size of crystallite (domains).

K is a dimensionless shape factor, about 0.89.

λ is the X-ray wavelength.

β is the line broadening in radians (FWHM).

θ is the Bragg angle (in degrees).

Oxidation state of the as-synthesized, calcined and reduced catalysts were analyzed by X-ray absorption near edge structure (XANES) at Beamline 5.2 at the Synchrotron Light Research Institute (Public Organization).

5.3.3 Catalytic deoxygenation testing

For palm oil HDO catalytic testing, the calcined sample was pressed to form pellets by hydraulic press, crushed and sieved to the size between 180 and 500 μm . The reaction was conducted in a continuous fixed-bed flow reactor with an internal diameter of 1 cm and length of 71 cm. For each run, 4 g of calcined catalyst was packed between SiC to improve heat transfer. The length of the catalyst-bed was 8 cm. Then, glass beads were fixed on both sides of the reactor to increase contact time between the feed and the catalyst. The reactor set up is shown in Figure 5.1. The calcined catalyst was reduced at 5°C/min under flowing H_2 -reduction at 650°C for 5 h, cooled to room temperature under the flow of nitrogen (20 ml/min) and held overnight.

To begin the testing process, nitrogen was switched off and the sample was pressurized with hydrogen (50 bar). Then, the catalyst was heated from room temperature to desired testing temperature with a rate 10°C/min, held for 15 min and

cooled down. After that, palm oil was fed to the reactor by an HPLC pump with the rate of 0.109 ml/min and mixed with hydrogen flow (109 ml/min, controlled by a mass flow controller). The pressure, collecting time, H₂ to oil ratio and liquid hourly space velocity (LHSV) in HDO testing were 50 bar, 3 h, 1,000:1 N(cm³/cm³) and 1 h⁻¹, respectively. Liquid and gas products were collected every 3 h.

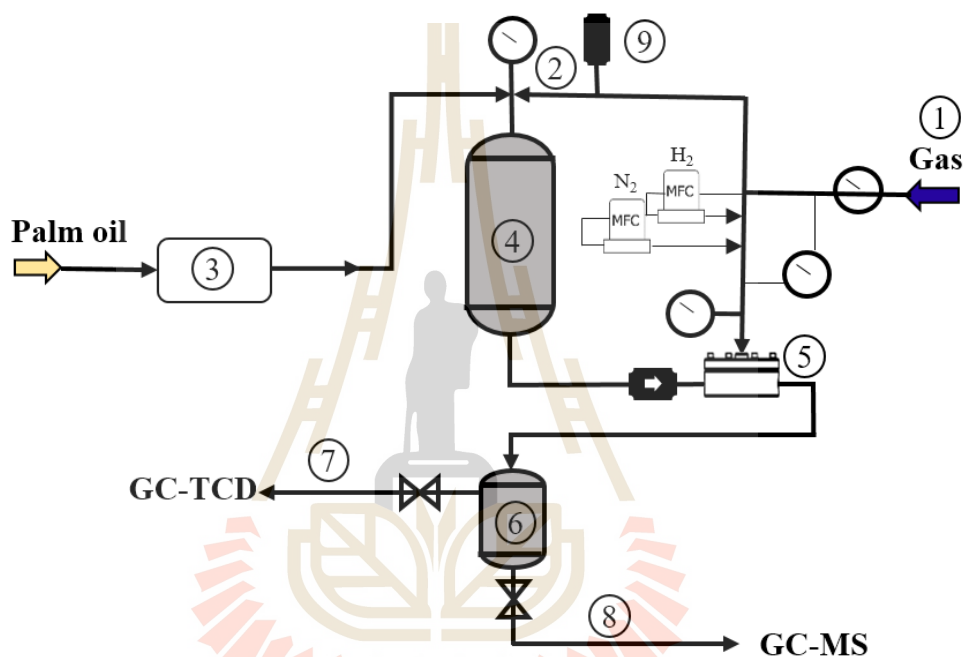


Figure 5.1 Hydrotreating reactor setup: No. 1, hydrogen flow (high pressure regulator); 2, pressure regulator; 3, HPLC pump (Lc-20AD, Bara Scientific); 4, reactor; 5, filler (SS-4TF-90, Swagelok) and back pressure regulator (Equilibar®); 6, product zone; 7, gas product (on-line GC-TCD); 8, liquid product (off-line GC-MS); 9, releasing pressure.

For comparison in catalytic performance in HDO reaction with synthesized nickel catalyst, a commercial nickel phosphide powder (Ni₂P, -100 mesh, 98%) was

purchased from Sigma-Aldrich, pressed and sieved to the size similar to the calcined nickel catalyst.

5.3.4 Product analysis

Liquid products were analyzed by an off-line gas chromatograph coupled with mass spectrometer (GC-MS Agilent 7890A equipped with DB-1HT column 30 m x 0.32 mm x 0.1 μ m). Briefly, 50 mg of sample was diluted with 1 ml of chloroform (CHCl_3 , Sigma-Aldrich, 99%) and then 1 μ l of sample was injected into the GC-MS with a split ratio of 50. The temperature of both injection and detector was 380°C. Quantities of *n*-alkane (*n*-C₇ to C₁₈) were determined from calibration curves of standards such as heptane (C₇H₁₆, Fluka, 99%), octane (C₈H₁₈, Fluka, 99%), *n*-nonane (C₉H₂₀, ACROS, 99%), *n*-undecane (C₁₁H₂₄, ACROS, 99%), dodecane (C₁₂H₂₆, Fluka, 99%), *n*-tridecane (C₁₃H₂₈, ACROS, 99%), tetradecane (C₁₄H₃₀, ACROS, 99%), pentadecane (C₁₅H₃₂, Fluka, 99%), hexadecane (C₁₆H₃₄, Fluka, 99%), heptadecane (C₁₇H₃₆, Fluka, 99%), octadecane (C₁₈H₃₈, Fluka, 99%). Five concentrations of mixed standard were prepared by diluting of 3, 5, 10, 15 and 30 μ l of each standard with 1 ml of chloroform.

Gas products (C₃H₈, C₂H₆, CH₄, CO, CO₂, N₂ and H₂) were analyzed by an on-line gas chromatograph with thermal conductivity detector (GC-TCD; Shimadzu, GC-14B) equipped with molecular sieve 5A (MS5A) and Porapak Q packed columns. The compositions were compared with a commercial mixture of gas standards. The temperature program of GC is similar to the literature (Srifa et al., 2014) as shown in Table 5.1.

Table 5.1 Operating condition for GC-TCD similar to literature (Srifa et al., 2014).

List program	Condition
Initial column temperature (°C)	40
Initial column time (min)	0
Column program rate (°C/min)	5
Final column temperature (°C)	80
Final column time (min)	15
Auxiliary injector column temperature (°C)	100
TCD Detector temperature (°C)	100

The percent conversion of triglycerides, selectivity, product yield, HDO, and the ratio of DCO and DCO₂ were calculated by Equation 1-5, respectively.

$$\text{Conversion of TG (\%)} = \frac{(\text{Mole TG in feed} - \text{Mole TG in product})}{\text{Mole TG in feed}} \times 100 \quad (1)$$

$$\text{Selectivity (\%)} = \frac{(\text{Mole of } n\text{- alkanes (C}_{15} \text{ to C}_{18}) \text{ in product})}{\text{Total mole of } n\text{- alkanes in product}} \times 100 \quad (2)$$

$$\text{Product yield (\%)} = \frac{(\text{Total mole of } n\text{- alkanes in product})}{\text{Total mole of fatty acids in feed}} \times 100 \quad (3)$$

$$\text{HDO (\%)} = \frac{(\text{Total mole of } n\text{- alkanes (C}_{8,10,12,14,16,18}) \text{ in product})}{\text{Total mole of fatty acids in feed}} \times 100 \quad (4)$$

$$\text{DCO + DCO}_2 \text{ (\%)} = \frac{(\text{Total mole of } n\text{- alkanes (C}_{7,9,11,13,15,17}) \text{ in product})}{\text{Total mole of fatty acids in feed}} \times 100 \quad (5)$$

Physical properties of the BHD product including color, pour point and cloud point that determined by using Mini Pour/Cloud point Tester (Tanaka, MPC-102S).

Four and a half milliliter of sample was filled in a vial and setup in the instrument, the temperature was increased from -60 to $+60^{\circ}\text{C}$ ($\pm 0.02^{\circ}\text{C}$) and detected by L/H mode. Percent of water in the BHD product was determined by using Karl Fischer titrator (KF; Metrohm, 870 KF Titrino plus, see Figure 5.2). The titrator was calibrated by mixing methanol (CH_3OH , Sigma-Aldrich, 99.9%) with hydranal-composite 5 ($\text{C}_2\text{H}_6\text{O}$, Fluka) before reacting with 0.01 g of DI water in Titer Ipol mode. For the product analysis, 0.4 g of BHD product was injected and titrated with hydranal-composite 5 in KFT Ipol mode. The percent of water was used to calculate in BHD conversion and not shown in the results.



Figure 5.2 Apparatus of Karl Fischer titrator.

5.4 Results and discussion

5.4.1 Catalysts appearance after the synthesis, calcination and reduction

Photographs of the as-synthesized, calcined and reduced catalysts are displayed in Figure 5.3. The colors changes are as follows: nickel catalyst, from green

to yellow and black; cobalt catalyst, from violet to violetish blue and grey; copper catalysts, from blue to pale-blue and grey, respectively. The changes in color indicated the phase change upon calcination and reduction.

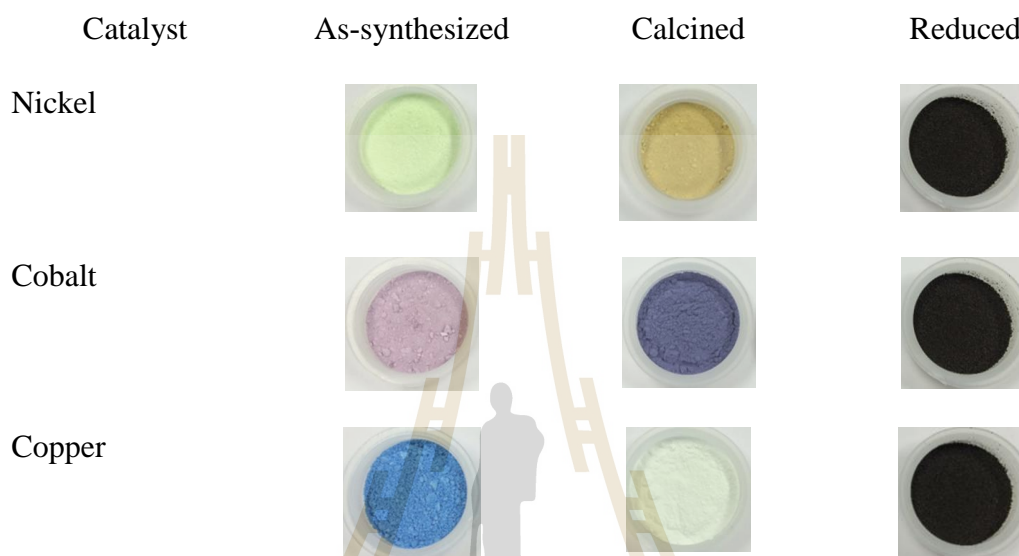


Figure 5.3 Appearance of catalysts after drying, calcination and reduction of nickel, cobalt and copper.

5.4.2 Catalyst morphology from SEM

Figure 5.4, 5.5 and 5.6 shows SEM images of reduced catalysts before testing in HDO reaction. The particle shape of the catalysts from nickel, cobalt and coppers are not uniform and different from each other.

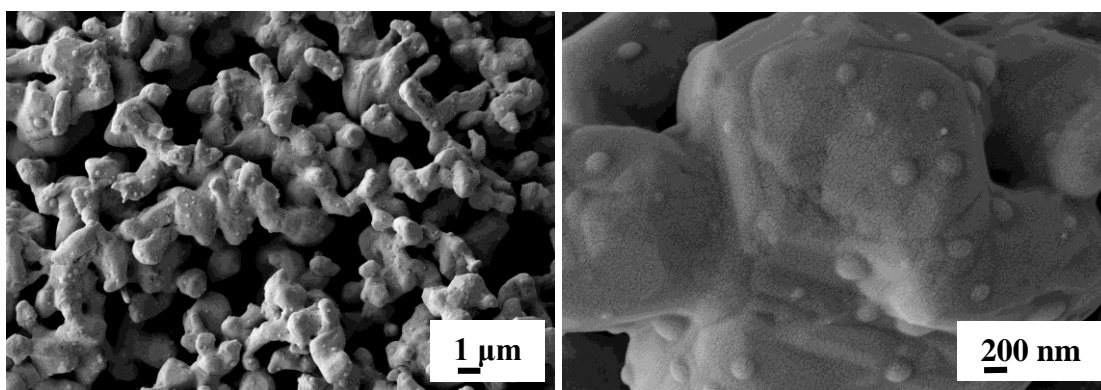


Figure 5.4 SEM images of reduced nickel catalyst before testing in HDO reaction.

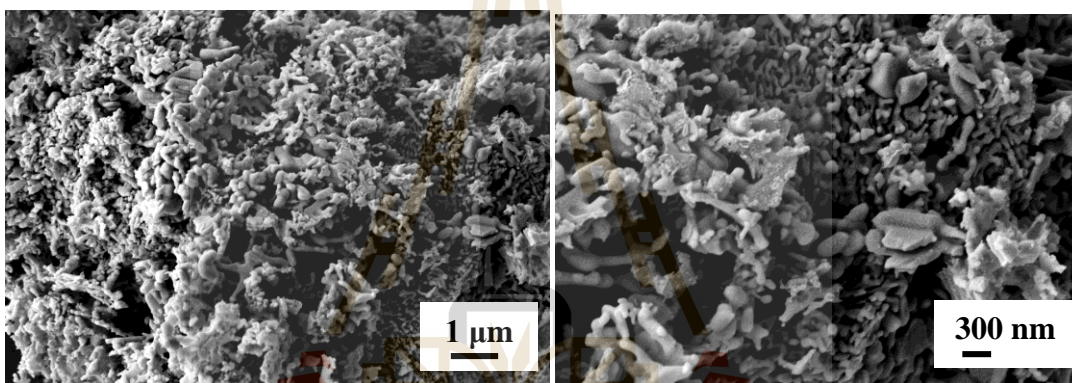


Figure 5.5 SEM images of reduced cobalt catalyst before testing in HDO reaction.

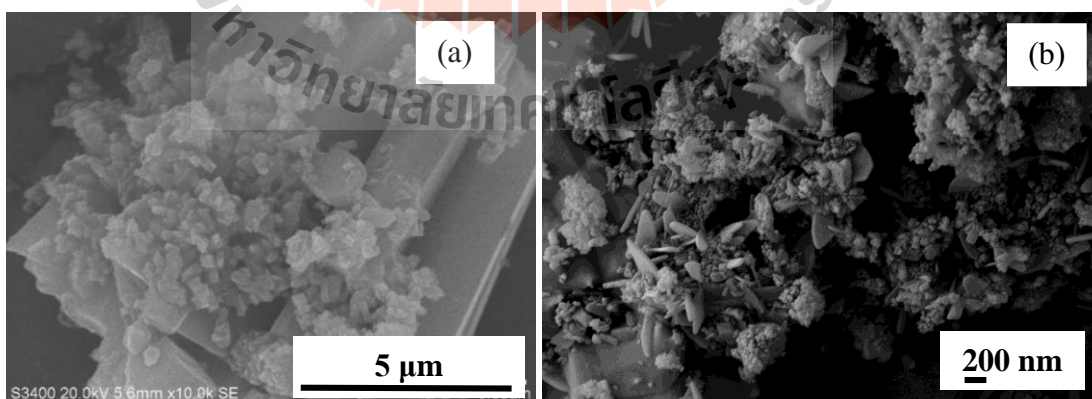


Figure 5.6 SEM images of (a) reduced copper catalyst without SiO₂ and (b) reduced copper catalyst with SiO₂ before testing in HDO reaction.

5.4.3 Catalysts characterization by XRD

Figure 5.7(a) shows XRD patterns of as-synthesized, calcined and reduced nickel samples before and after the catalytic testing. The pattern of the as-synthesized sample was broad indicating an amorphous phase. The calcined-sample has peaks at $2\theta = 30.0, 35.8, 38.2$ and 43.4° which are characteristic of $\alpha\text{-Ni}_2\text{P}_2\text{O}_7$ (PDF 01-074-1604). The diffraction peaks of reduced-sample indicate a mixed phase between Ni_2P and Ni_{12}P_5 (PDF 74-1385 and PDF 74-1381). The peak positions at $2\theta = 40.7, 44.5, 47.3, 54.1$ and 55.0° (PDF 74-1385; Xin et al., 2016) are Ni_2P phase and at $2\theta = 38.3, 41.7$ and 48.9° are the diffraction peaks of Ni_{12}P_5 correspond to a tetragonal structure (Kucernak et al., 2014; Xin et al., 2016).

Structures of Ni_2P and Ni_{12}P_5 generated by Inorganic Crystal Structure Database (ICSD) are shown in Figure 5.7(b) and (c). Ni_2P has a hexagonal structure and the space group $p\text{-}62\text{m}$ with the following lattice parameters: $a = b = 5.859 \text{ \AA}$ and $c = 3.382 \text{ \AA}$. Ni_{12}P_5 has a tetragonal structure with lattice parameters $a = b = 8.646 \text{ \AA}$ and $c = 5.07 \text{ \AA}$ (Kucernak et al., 2014; Xin et al., 2016).

The crystallite sizes of Ni_2P and Ni_{12}P_5 at before testing, calculated using the Scherrer equation were 45.3 nm and 31.7 nm, respectively. After the reaction testing the crystallite size of Ni_2P decreased while the crystallite size of Ni_{12}P_5 increased indicating further reduction of Ni_2P by hydrogen in the reactor to Ni_{12}P_5 . The crystallite sizes of Ni_2P and Ni_{12}P_5 at after reaction testing were 36.9 nm and 40.9 nm, respectively.

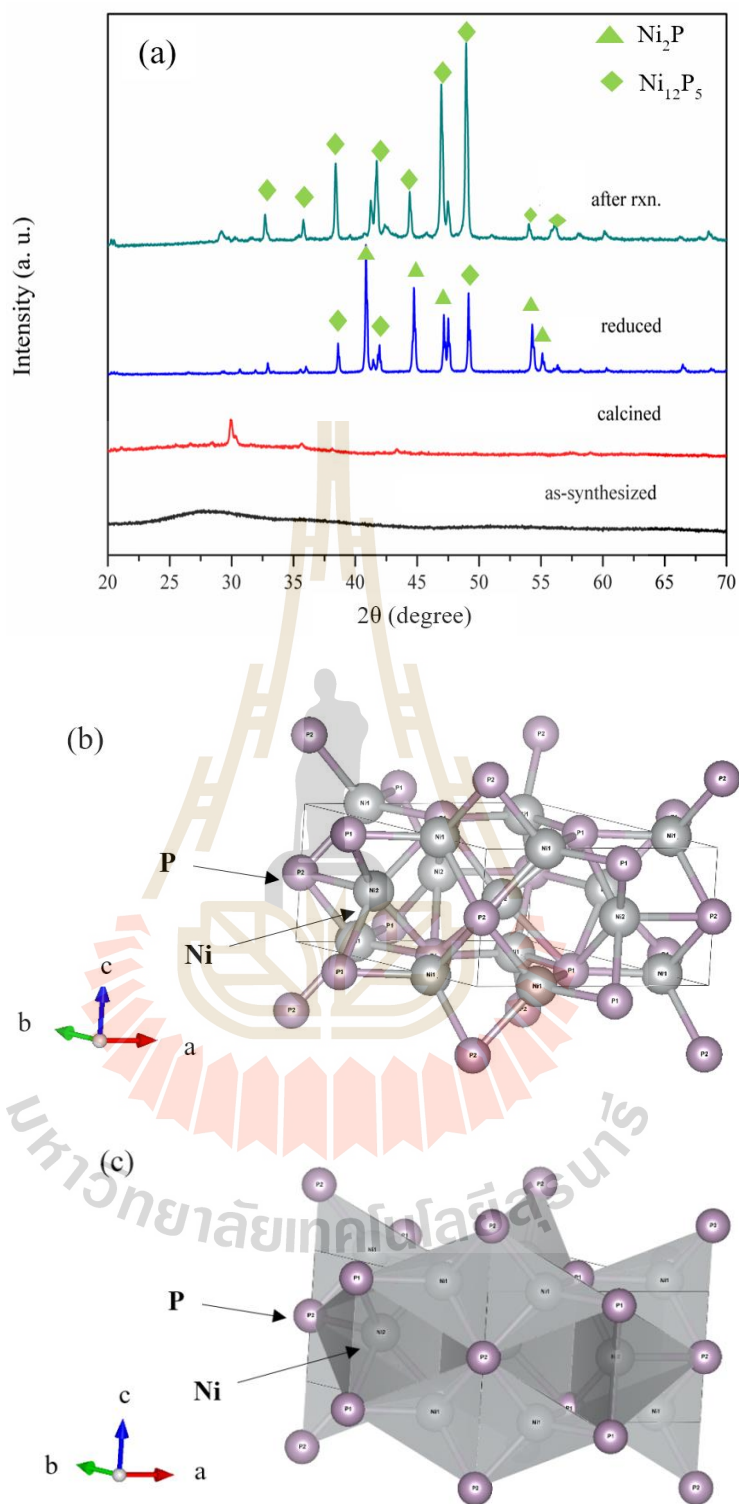


Figure 5.7 (a) XRD patterns of as-synthesized, calcined and reduced nickel catalyst, (b, c) structure of Ni_2P generated from ICSD program.

Figure 5.8(a) shows the XRD patterns of as-synthesized, calcined and reduced cobalt samples before and after the catalytic testing. The as-synthesized sample displays peaks at $2\theta = 25.0, 32.6, 38.7, 42.7, 46.4$ and 53.7° corresponding to $\text{Co}(\text{H}_2\text{PO}_4)_2 \cdot 2\text{H}_2\text{O}$. The calcined sample shows peaks at $2\theta = 31.2, 36.8, 44.8, 59.4$ and 65.2° corresponding to Co_3O_4 (PDF 00-042-146). The reduced cobalt sample gives peaks at $2\theta = 40.7, 41.0$ and 52.0° corresponding to the planes 121, 211, 022 of cobalt phosphide (Co_2P) (PDF 00-032-0306). Those peaks confirmed that Co_3O_4 was reduced to Co_2P under hydrogen pressure (Liu et al., 2008). The crystal sizes of Co_2P before and after testing calculated by Scherrer equation were 32.6 and 38.6 nm, respectively. The results indicated that catalyst sintering occurred during the reaction.

Structures of Co_2P drawn by ICSD program are shown in Figure 5.8(b) and (c). The structure is orthorhombic and the space group is Pnma (62) with the lattice parameters as follows: $a = 5.654 \text{ \AA}$, $b = 3.511 \text{ \AA}$ and $c = 6.606 \text{ \AA}$.

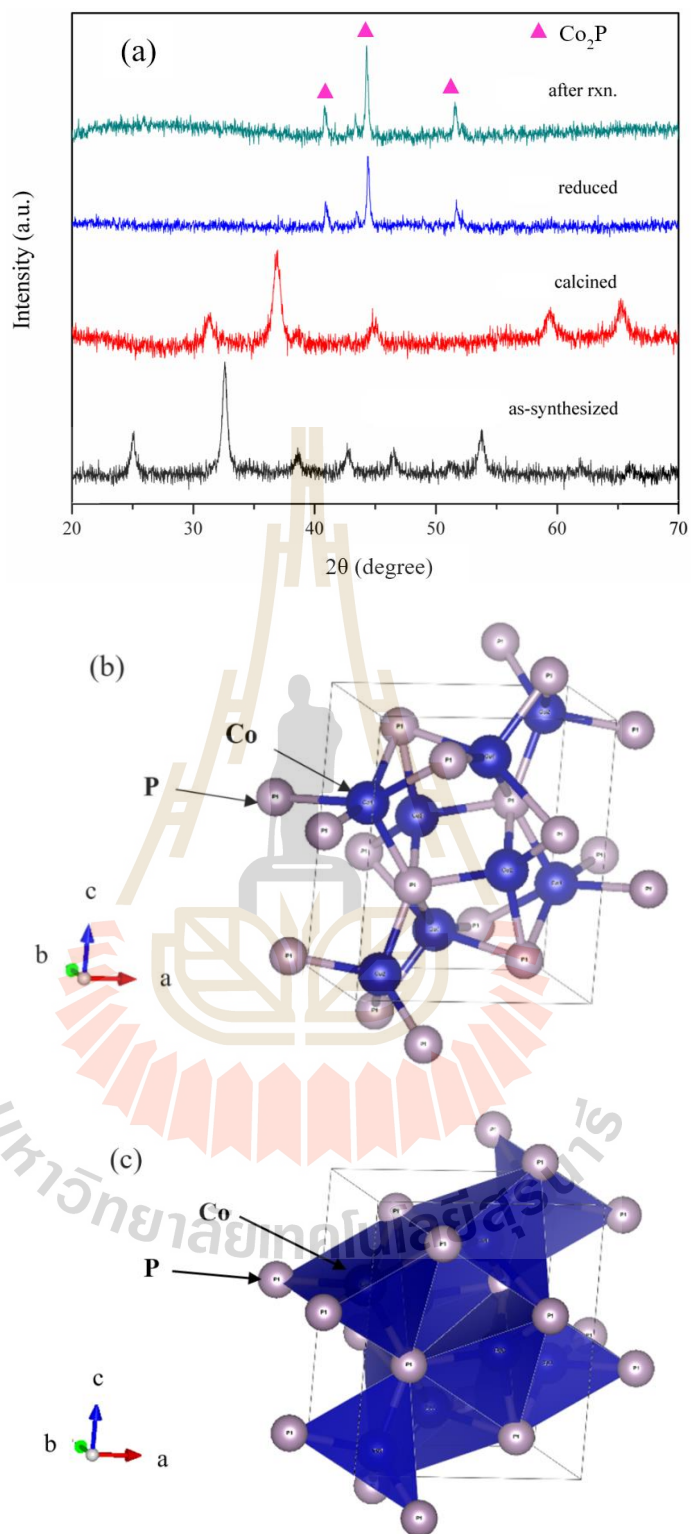


Figure 5.8 (a) XRD patterns of as-synthesized-, calcined- and reduced-cobalt catalysts and (b, c) structure of Co_2P generated from ICSD program.

Figure 5.9(a) shows XRD patterns of as-synthesized-, calcined- and reduced-copper samples before and after testing in reaction. The as-synthesized sample displays peaks at $2\theta = 27.6, 29.0, 31.0, 32.4$ and 35.2° corresponding to copper hydrogen phosphate monohydrate ($\text{CuHPO}_4 \cdot \text{H}_2\text{O}$) (PDF 01-083-1857). The calcined sample shows peak at $2\theta = 28.8, 30.4, 35.5^\circ$ corresponding to copper pyrophosphate ($\alpha\text{-Cu}_2\text{P}_2\text{O}_7$) (PDF 00-044-0182; Khemthong et al., 2012; Su et al., 1999). The reduced copper sample showed peak position at $2\theta = 36.3, 39.3, 41.8, 45.3, 46.4$ and 47.5° corresponding to Cu_3P (PDF 00-002-1263). After the reaction testing, the peaks intensities increased indicating that sintering occurred. The crystalline sizes of Cu_3P before and after the catalytic testing were 46.9 nm and 74.6 nm, respectively. The crystallite sizes at after reaction testing showed higher crystallite sizes than before testing indicating that agglomeration of Cu-Cu bonds.

Structures of Cu_3P drawn by ICSD program are shown in Figure 5.9(b) and (c). The copper phosphide (Cu_3P) has a trigonal structure with space group P-3 c1(165), the following lattice parameters $a = b = 6.992 \text{ \AA}$ and $c = 7.170 \text{ \AA}$.

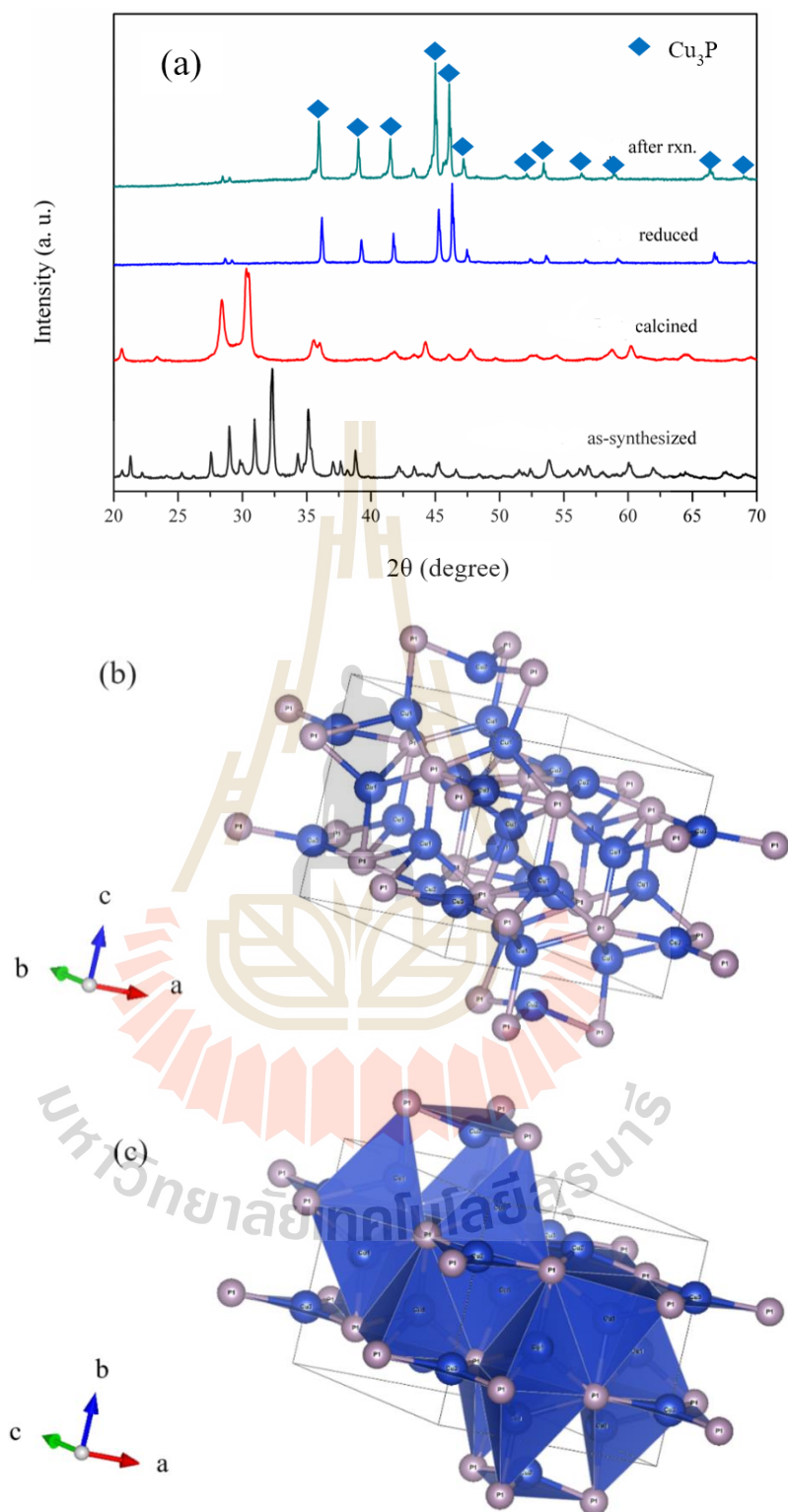


Figure 5.9 (a) XRD patterns of as-synthesized-, calcined- and reduced-copper catalysts and (b, c) structure of Cu_3P generated from ICSD program.

5.4.4 Catalysts characterization by XANES

Figure 5.10 shows XANES spectra of nickel samples compared with standard materials and Table 5.2 shows their edge positions. The as-synthesized and calcined Ni samples had similar XANES spectra and edge position except that the calcined sample had a stronger white line. Thus, these samples had nickel with the same oxidation state. The edge energies of nickel in these samples are similar to that of in NiO confirming that the dominant oxidation state of these Ni samples were +2 (Itthibenchapong et al., 2017).

The XANES spectra of the reduced sample had some similarity to Ni₂P and metallic Ni. The white line decreased but still higher than that of Ni₂P and metallic nickel. The edge energy of Ni was close to that of Ni₂P but higher than the edge of metallic nickel.

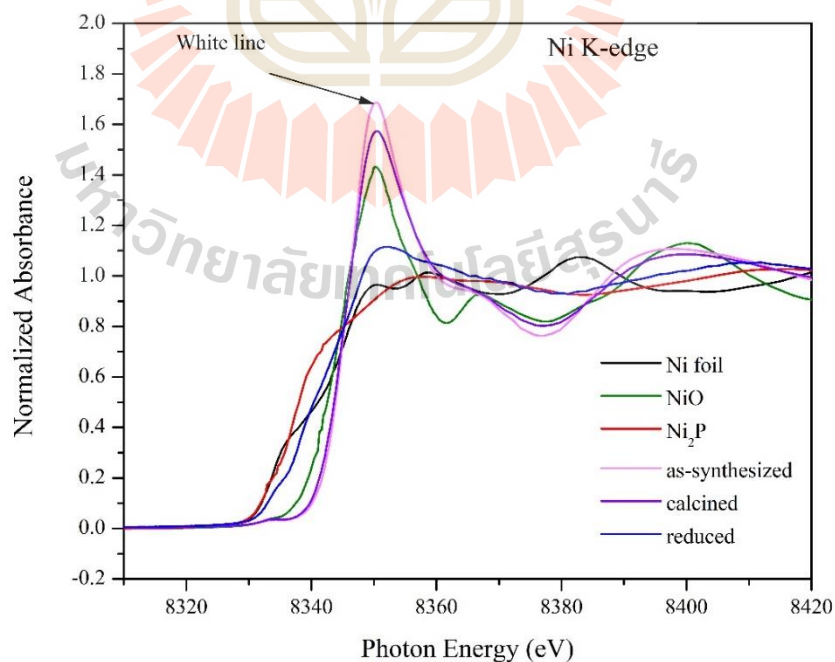


Figure 5.10 XANES spectrum of nickel catalysts and standards.

Table 5.2 Edge position of nickel sample and standards.

Sample	Edge position (eV)
As-synthesized sample	8345.9
Calcined sample	8344.9
Reduced sample	8341.6
Ni foil (Ni ⁰)	8332.3
Ni ₂ P (Ni ^{1+,2+})	8341.9
NiO (Ni ²⁺)	8345.5

Figure 5.11 shows XANES spectra of cobalt samples compared with reference materials including Co foil, CoO and Co₃O₄. Table 5.3 shows their edge positions. The as-synthesized sample had the highest edge energy close to that of Co₃O₄. After being reduced, the edge was close to that of CoO. Thus, the oxidation state of cobalt changed from +3 to +2 after calcination and reduction (Khemthong et al., 2010). The XANES spectra of the reduced sample lied between that of the metallic foil and oxides and the white line decreased.

Figure 5.12 shows XANES spectra of Cu samples and compares with copper reference including Cu foil, Cu₂O and CuO. Table 5.4 shows edge position of copper samples and copper references. The XANES feature of as-synthesized and calcined samples had similar edge energy and higher than those of the standards. The oxidation state of these samples was +2 (Vaseem et al., 2008). The edge energy of copper in the reduced sample was 8978.5 eV, lower than those of all standards indicating that it was reduced to low oxidation state.

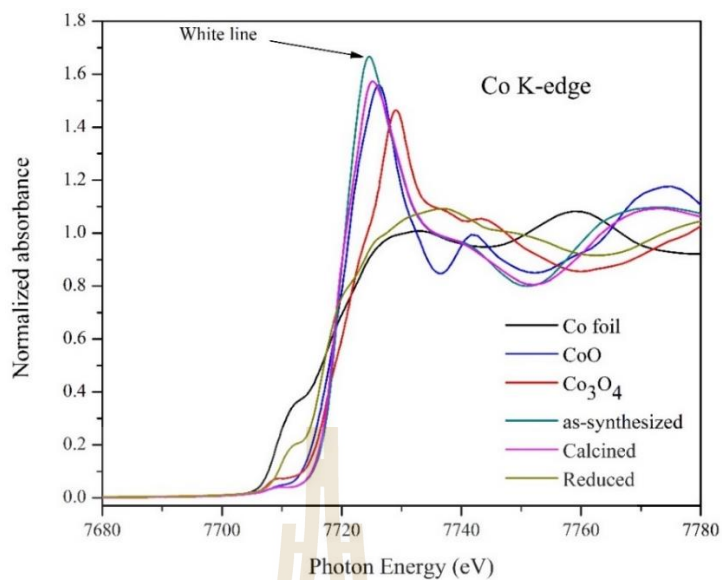


Figure 5.11 XANES spectrum of cobalt catalysts and standards.

Table 5.3 Edge position of cobalt sample and standards.

Sample	Edge position (eV)
As-synthesized sample	7719.09
Calcined sample	7718.32
Reduced sample	7716.59
Co foil (Co^0)	7709.8
CoO (Co^{2+})	7717.2
Co_3O_4 ($\text{Co}^{2+,3+}$)	7719.6

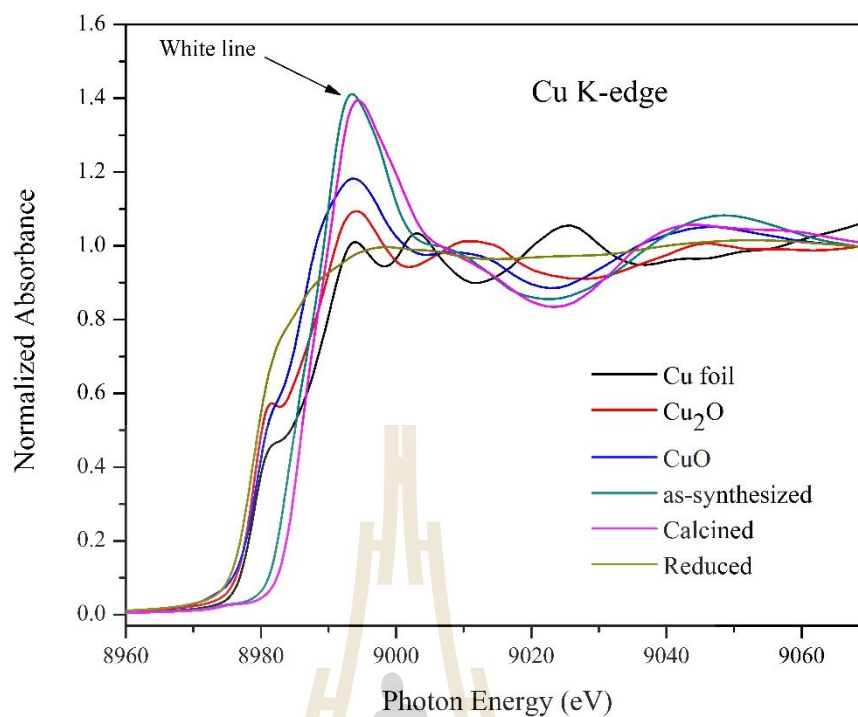


Figure 5.12 XANES spectrum of copper catalysts and standards.

Table 5.4 Edge position of copper sample and standards.

Sample	Edge position (eV)
As-synthesized sample	8983.9
Calcined sample	8985.9
Reduced sample	8978.5
Cu foil (Cu^0)	8979.0
Cu_2O (Cu^{1+})	8980.4
CuO (Cu^{2+})	8983.6

Figure 5.13 shows XRD pattern of commercial Ni_2P (-100 mesh, Sigma-Aldrich, 98%) which is used for comparison with the synthesized nickel phosphide catalyst in HDO of palm oil. After testing in HDO reaction under high hydrogen

pressure, the nickel phosphide sample showed the mixed phase of Ni_2P and Ni_{12}P_5 . The crystallites size of before and after the reaction were 17.5 nm and 29.3 nm (calculated by Scherrer equation), respectively. Figure 5.14 shows the morphology of commercial nickel phosphide catalyst before testing in the reaction. It shows the large particle sizes which has some small particle on the surface of the catalyst.

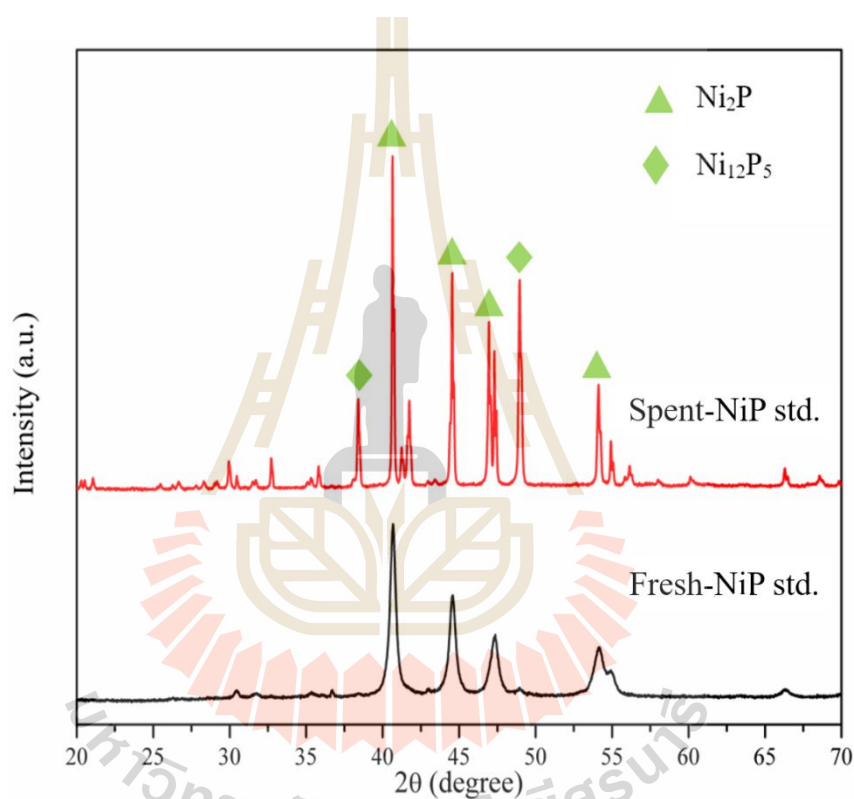


Figure 5.13 XRD patterns of commercial Ni_2P catalyst at before and after HDO reaction of palm oil.

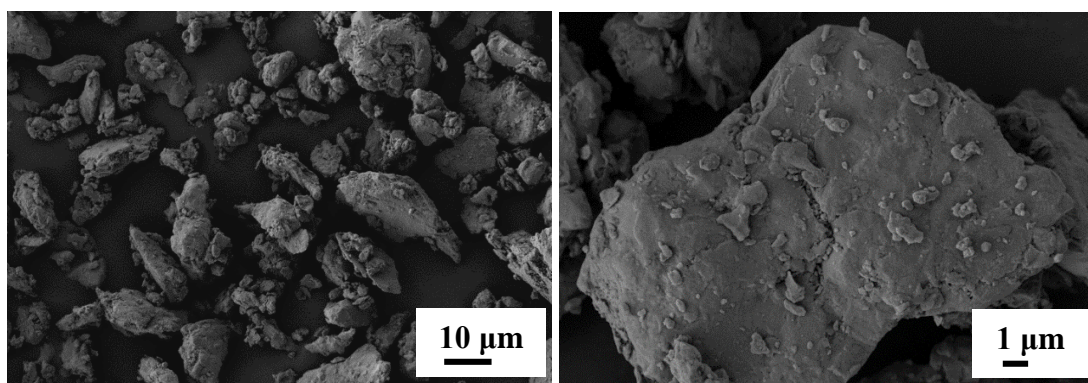


Figure 5.14 SEM images of commercial nickel phosphide catalyst before testing in HDO reaction.

5.4.5 Catalytic hydrotreating of palm oil

Figure 5.15(a) shows conversions and C_{15} - C_{18} selectivity of metal phosphide catalysts. Figure 5.15(b) shows product yields, selectivity of HDO and DCO_2+DCO . At 300°C the conversions from the phosphides catalysts are in the following order: Ni > Co > Cu. However, the selectivity of C_{15} - C_{18} , HDO and DCO_2+DCO from all catalysts are either not detectable or very low. Thus, this temperature is not suitable for hydrotreating of palm oil. At 350°C, the trend of activities is still the same. The conversions and C_{15} - C_{18} selectivity on Ni catalyst reached 100%. The yield of 100% was obtained from HDO and DCO_2+DCO . On Co catalyst, the conversions also increased but the C_{15} - C_{18} selectivity were much lower than Ni catalyst. The yields from Co catalysts were about 30% also from HDO and DCO_2+DCO . On Cu catalyst, the conversion dropped significantly and C_{15} - C_{18} selectivity were still not detectable. The yields from Cu catalyst at this temperature were not detectable. At 400°C the conversions from all catalysts were 100%. The C_{15} - C_{18} selectivity were in the following order: Ni > Co > Cu. However, the selectivity from Ni and Co catalysts were lower than

those at 350°C. The yields, selectivity of HDO and DCO₂+DCO were lower than 350°C with the same trend, namely, Ni > Co > Cu. From those results, at 350°C Ni was the best catalyst and was the most suitable temperature.

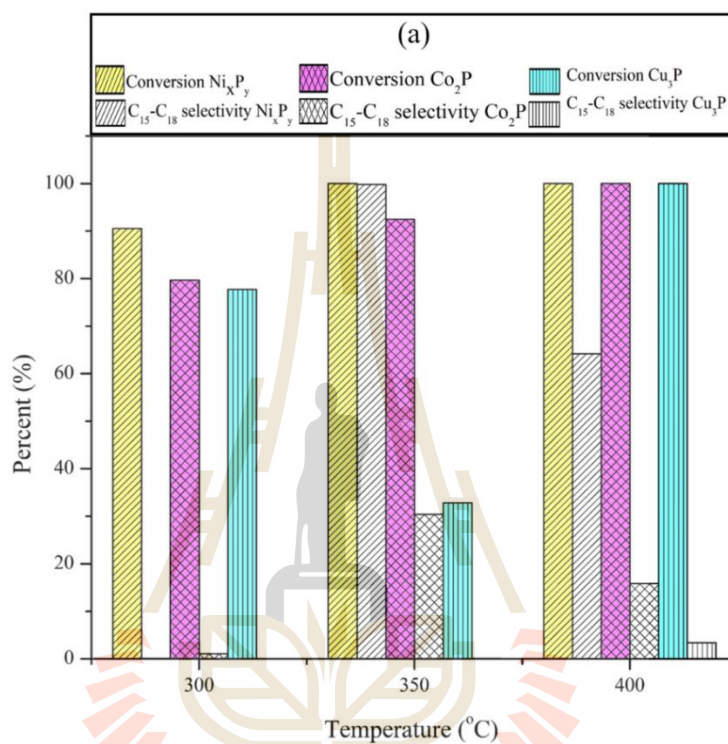


Figure 5.15 (a) Conversion and selectivity of sample screening by varying the temperature.

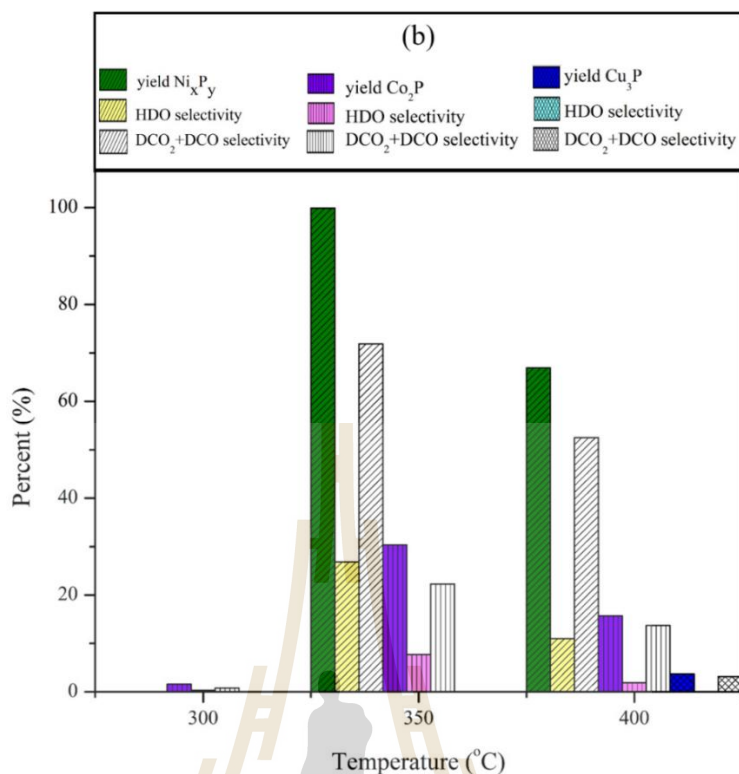


Figure 5.15 (Continued) (b) Product yield and competitive reaction of sample screening by varying the temperature.

Appearance of products from Ni, Co and Cu catalysts are shown in Figure 5.16. Here, the attention is focused on product from Ni catalyst which showed the best performance. The color of product from Ni catalyst at 350°C was still light yellowish indicating the present of unsaturated bonds which could lead to undesirable reactions. Thus, an attempt to improve the product quality was made by increasing the temperature to 380°C and products were analyzed at 3, 6 and 9 h.

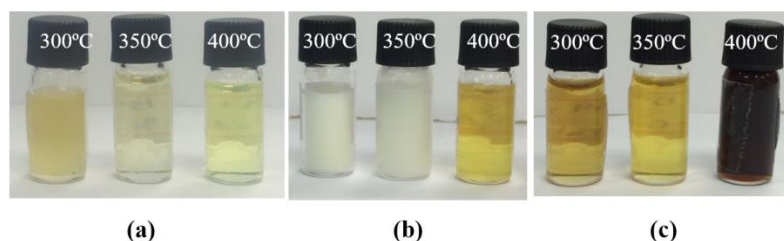


Figure 5.16 Appearance BHD product of screening samples (a) Ni_xP_y , (b) Co_2P , (c) Cu_3P ; at 300, 350 and 400°C, hydrogen pressure 50 bar.

Figure 5.17(a) shows comparison of catalytic performance between Ni_xP_y catalyst and commercial Ni_2P at 380°C. products were collected after 3, 6 and 9 h. At 3 h, Ni_xP_y catalyst did not produce much products. The conversion on commercial Ni_2P was complete with low yield and selectivity. At 6 h, both Ni_xP_y catalyst and commercial Ni_2P gave complete conversions. However, the Ni_xP_y catalyst gave better yield and selectivity than the commercial Ni_2P . At 9 h, both Ni_xP_y catalyst and commercial Ni_2P still gave complete conversions. The yield, $\text{C}_{15}\text{-C}_{18}$ selectivity and DCO_2+DCO selectivity increased over Ni_xP_y catalyst but decrease over the commercial Ni_2P .

Figure 5.17(b) shows distribution of $\text{C}_{15}\text{-C}_{18}$ products. C_{15} and C_{18} were the major products from both catalysts consistent with the gas product from methanation, i.e., CO reduced to CH_4 (see Figure 5.17(c)). The results indicated that DCO_2 and DCO are the major reaction routes. Itthibenchapong et al. (2017) reported cracking as a side reaction of $\text{Ni-MoS}_2/\gamma\text{-Al}_2\text{O}_3$ catalyst tended to occur at high temperature, especially, propane cracking at 330°C based on an increased in the ethane (C_2H_6) composition in the gas products. The increase in yield, $\text{C}_{15}\text{-C}_{18}$ selectivity and DCO_2+DCO selectivity could indicate changes on the Ni_xP_y catalysts.

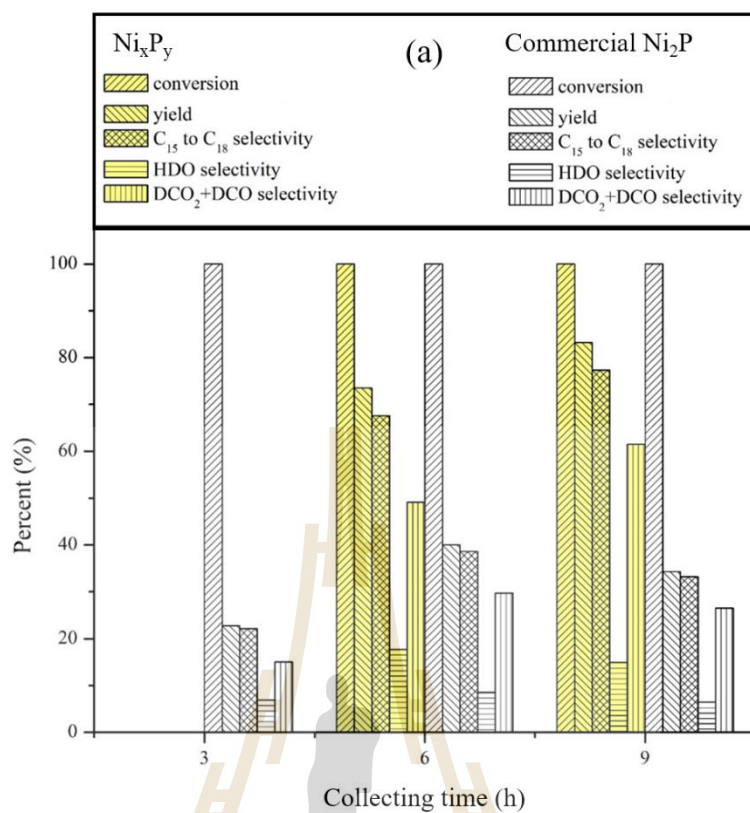


Figure 5.17 (a) Conversion, product yield and competitive reaction of palm oil tested at 380°C, hydrogen pressure of 50 bar, product collecting time of 0-9 h and LHSV of 1 h⁻¹.

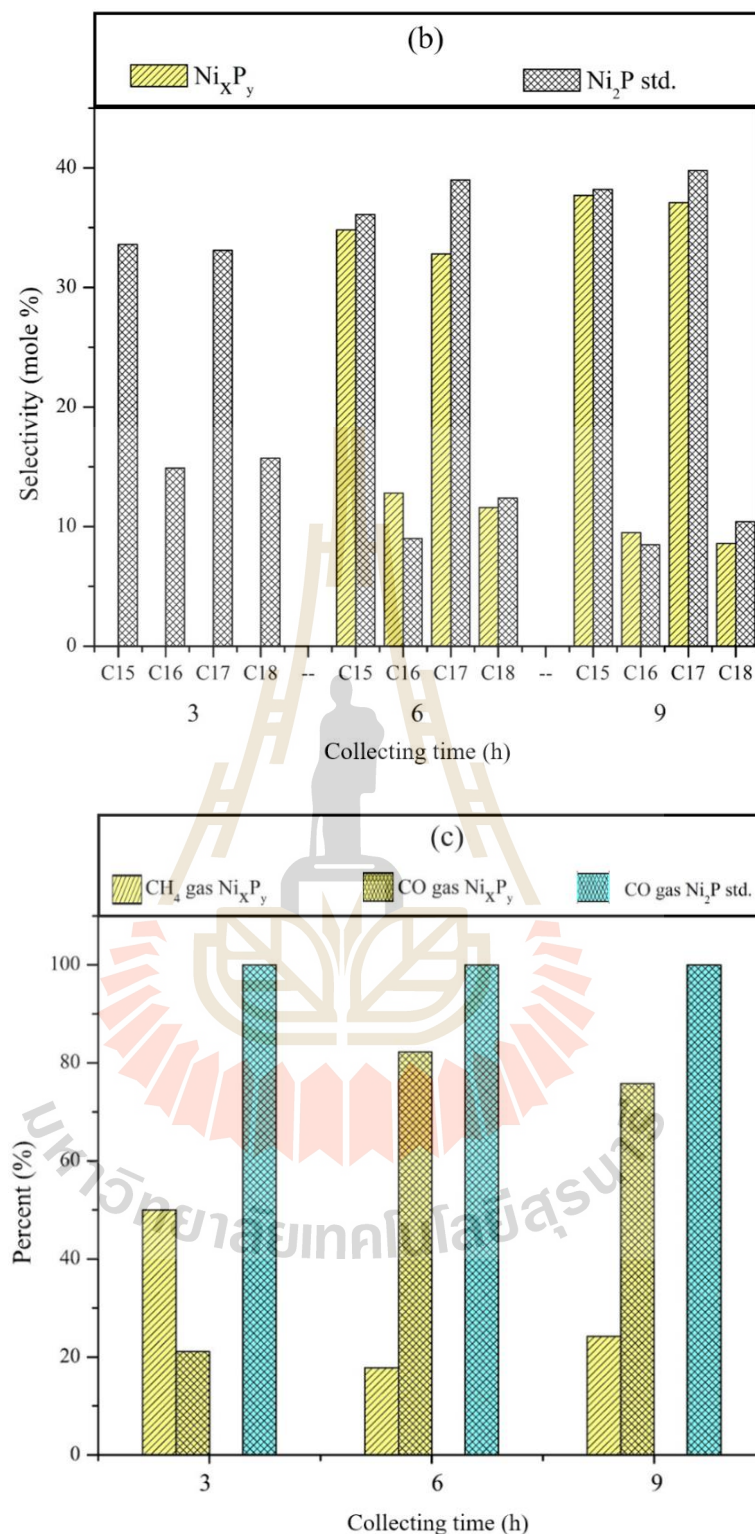


Figure 5.17 (Continued) (b) Selectivity, (c) gas product of palm oil tested at 380°C, hydrogen pressure of 50 bar, product collecting time of 0-9 h and LHSV of 1 h⁻¹.

Figure 5.18 shows appearance of products from Ni catalyst and commercial Ni₂P. Only the product from Ni catalyst at 9 h was colorless, indicating the best oil quality.

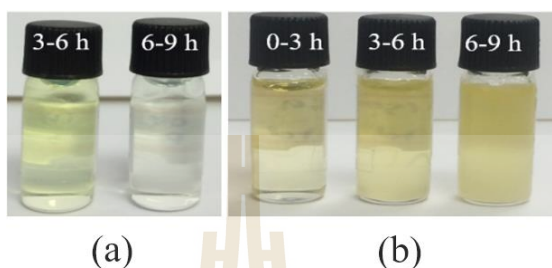


Figure 5.18 Appearance BHD product of screening samples (a) Ni_xP_y, (b) commercial Ni₂P at 380°C and hydrogen pressure 50 bar.

Table 5.5 shows the properties of BHD product including color, pour point and cloud point of BHD products from Ni catalyst and commercial Ni₂P. All of the products showed clear color and high quality of fuel which low pour point and cloud point. Soletio-Boyás et al. (2012) reported the high properties of liquid hydrocarbon product that had pour point and cloud point less than 20°C.

Table 5.5 The physical properties of BHD product.

Catalysts	Color	Pour Point/Cloud Point (°C)	
		Collecting time (6 h)	Collecting time (9 h)
Ni _x P _y	Clear yellow	9.0/10.0	13.8/18.0
Commercial Ni ₂ P	Pale yellow	7.0/16.0	14.0/19.0

5.4.6 Characterization of spent catalysts

XRD pattern of spent Ni, Co and Cu catalysts are shown in Figure 5.7(a), 5.8(a) and 5.9(a), respectively. The spent Ni catalyst showed stronger peaks of Ni_{12}P_5 phase than the fresh reduced catalyst indicating that further reduction of Ni_2P occurred during the reaction due to the long period of heating under H_2 atmosphere and transformed it to Ni_{12}P_5 .

The XRD pattern of the spent Co_3P and Cu_3P shows peaks similar to freshly reduced catalysts, but with stronger intensities. The results indicated that sintering also occurred on these catalysts.

5.5 Conclusions

Phosphides of Ni, Co and Cu were prepared by precipitation method and characterized by several techniques. After reduction, the nickel sample contained a mixed phase of Ni_2P and Ni_{12}P_5 whereas cobalt and copper samples contained Co_2P and Cu_3P , respectively. After the reaction testing, spent nickel catalyst had more amount of Ni_{12}P_5 phase. Catalytic performance in HDO reaction of all sample testing at 300, 350 and 400°C was following in the order: $\text{Ni} > \text{Co} > \text{Cu}$. From the results, Ni was the best catalyst and 350°C was the most suitable temperature. The color of product from Ni catalyst at 350°C was still light yellowish indicating the present of unsaturated bonds which could lead to undesirable reactions. Thus, an attempt to improve the product quality was made by increasing the temperature to 380°C and products were analyzed at 3, 6 and 9 h which compared by commercial Ni_2P catalyst. At 9 h, both Ni_xP_y catalyst and commercial Ni_2P still gave complete conversions. The yield, $\text{C}_{15}\text{-C}_{18}$ selectivity and $\text{DCO}_2 + \text{DCO}$ selectivity increased over Ni_xP_y catalyst but decrease over

the commercial Ni₂P. The optimum product yield of Ni_xP_y catalyst was 83.2 % and selectivity to HDO, DCO₂ + DCO and C₁₅ to C₁₈ was 15.0 %, 61.5 % and 77.3 %, respectively.

5.6 References

- Berhault, G., Afanasiev, P., Loboue, H., Geantet, C., Cseri, T., Pichon, C., and Lafond, A. (2009). In situ XRD, XAS, and magnetic susceptibility study of the reduction of ammonium nickel phosphate NiNH₄PO₄•H₂O into nickel phosphide. **Inorganic Chemistry**. 48(7): 2985-2992.
- Guan, Q., Wan, F., Han, F., Liu, Z., and Li, W. (2016). Hydrodeoxygenation of methyl palmitate over MCM-41 supported nickel phosphide catalysts. **Catalysis Today**. 259: 467-473.
- Itthibenchapong, V., Srifa, A., Kaewmeesri, R., Kidkhunthod, P., and Faungnawakij, K. (2017). Deoxygenation of palm kernel oil to jet fuel-like hydrocarbons using Ni-MoS₂/γ-Al₂O₃ catalysts. **Energy Conversion and Management**. 134: 188-196.
- Khemthong, P., Klysubun, W., Prayoonpokarach, S., and Wittayakun, J. (2010). Reducibility of cobalt species impregnated on NaY and HY zeolites. **Materials Chemistry and Physics**. 121(1): 131-137.
- Khemthong, P., Daorattanachai, P., Laosiripojana, N., and Faungnawakij, K. (2012). Copper phosphate nanostructures dehydration of fructose to 5-hydroxymethylfurfural. **Catalysis Communications**. 29: 96-100.

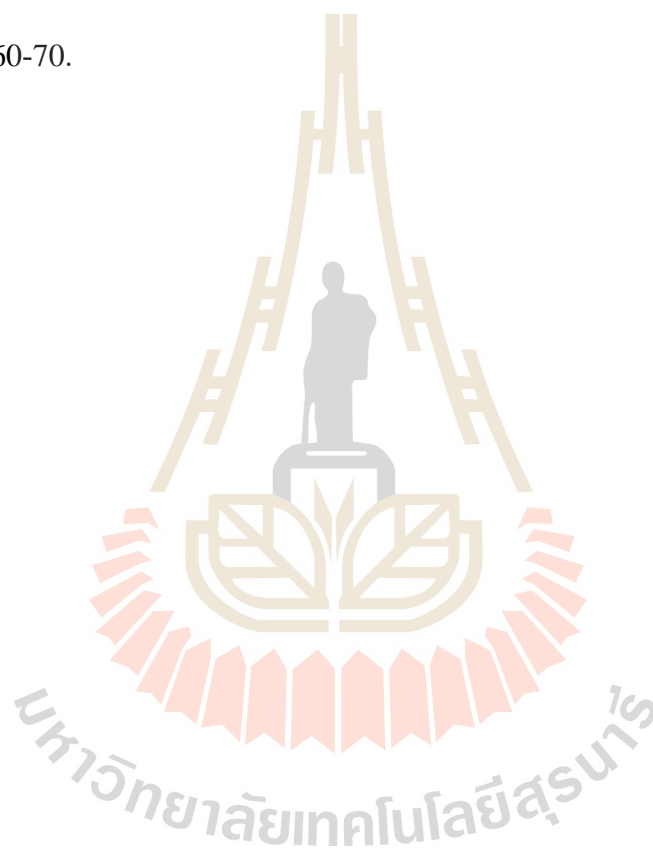
- Kucernak, A. R. J., and Sundaram, V. N. N. (2014). Nickel phosphide: the effect of phosphorus content on hydrogen evolution activity and corrosion resistance in acid medium. **Journal of Materials Chemistry A**. 2: 17435-17445.
- Liu, S., Qian, Y., and Ma, X. (2008). Polymer-assisted synthesis of Co₂P nanocrystals. **Materials Letters**. 62(1): 11-14.
- Mikkonen, S. (2008). Second-generation renewable diesel offers advantages. **Hydrocarbon Processing**. 87(2): 63-66.
- Phimsen, S., Kiatkittipong, W., Yamada, H., Tagawa, T., Kiatkittipong, K., Laosiripojana, N., and Assabumrungrat, S. (2017). Nickel sulfide, nickel phosphide and nickel carbide catalysts for bio-hydrotreated fuel production. **Energy Conversion and Management**. 151: 324-333.
- Sotelo-Boyás, R., Trejo-Zárraga, F., and de Jesús Hernández-Loyo, F. (2012). Hydroconversion of triglycerides into green liquid fuels. In Hydrogenation. **InTech**. 187-215.
- Srifa, A., Faungnawakij, K., Itthibenchapong, V., Viriya-Empikul, N., Charinpanitkul, T., and Assabumrungrat, S. (2014). Production of bio-hydrogenated diesel by catalytic hydrotreating of palm oil over NiMoS₂/γ-Al₂O₃ catalyst. **Bioresource Technology**. 158: 81-90.
- Su, H. L., Xie, Y., Li, B., Liu, X. M., and Qian, Y. T. (1999). A simple, convenient, mild solvothermal route to nanocrystalline Cu₃P and Ni₂P. **Solid State Ionics**. 122(1-4): 157-160.
- Vaseem, M., Umar, A., Hahn, Y. B., Kim, D. H., Lee, K. S., Jang, J. S., and Lee, J. S. (2008). Flower-shaped CuO nanostructures: structural, photocatalytic and XANES studies. **Catalysis Communications**. 10(1): 11-16.

Xin, H., Guo, K., Li, D., Yang, H., and Hu, C. (2016). Production of high-grade diesel from palmitic acid over activated carbon-supported nickel phosphide catalysts.

Applied Catalysis B: Environmental. 187: 375-385.

Yang, Y., Ochoa-Hernández, C., Pizarro, P., Víctor, A., Coronado, J. M., and Serrano, D. P. (2015). Influence of the Ni/P ratio and metal loading on the performance of Ni_xP_y/SBA-15 catalysts for the hydrodeoxygenation of methyl oleate. **Fuel.**

144: 60-70.



CHAPTER VI

HYDRODEOXYGENATION OF PALM OIL TO BIO-HYDROGENATED DIESEL OVER NICKEL PHOSPHIDE SUPPORTED ON ACTIVATED CARBON AND SBA-15

6.1 Abstract

Catalysts containing nickel phosphide on activated carbon produced from a tube furnace (NiP/AC_TF), from Iwasaki kiln (NiP/AC_IW) and SBA-15 (NiP/SBA-15) were prepared. After reduction, Ni₂P phase was obtained in all catalysts with crystal size of 18.4, 26.2 nm and 25.4 nm, respectively. The catalysts were tested on for hydrodeoxygenation (HDO) reaction of palm oil in a continuous fixed-bed flow reactor to produce bio-hydrogenated diesel (BHD). The testing condition was at 350°C for NiP/AC and at 380°C for NiP/SBA-15 catalysts under H₂ atmosphere of 50 bar and collecting time 6 h. The catalytic activity of the catalyst based on BHD selectivity was in the order: NiP/AC_IW > NiP/SBA-15 > NiP/AC_TF. The NiP/AC_IW catalysts gave the highest BHD yield of 98.3%.

6.2 Introduction

From Chapter V, nickel phosphide was the best catalyst for hydrodeoxygenation (HDO) reaction to produce bio-hydrogenated diesel (BHD) product. However, changes of the catalysts by sintering and reduction occurred during the reaction. Such changes could be minimized by dispersion of nickel phosphide species on supports with high surface area such as activated carbon (Xin et al., 2016), SBA-15 (Yang et al., 2012; Liu et al., 2004) and MCM-41 (Guan et al., 2016). In this Chapter, the selected support materials were activated carbon and SBA-15.

Activated carbon is an amorphous solid with a large surface area from the presence of microspores (width < 2 nm). Activated carbon is interesting as a support material in HDO reaction because it has both acidic hydrophilic surface and basic hydrophobic surface. The acidic nature could assist hydrogenation and cleavage of C(sp²)-O bond and deoxygenation while the basic nature could decrease coke formation (Arun et al., 2015). The surface functional groups on activated carbon were important to prepare metal catalysts in HDO of palm oil to produce BHD product.

The molar ratios of nickel phosphide loading had effect for catalytic performance in HDO reaction. Xin et al. (2016) studied the effect of Ni/P molar ratios loading on activated carbon to produced high-grade diesel from palmitic acid. They varied Ni/P ratios from 0.5 to 4.0 and found that there were various crystalline phases including pure phase Ni₂P, mixed phase between Ni₂P and Ni₁₂P₅, pure phase Ni₁₂P₅ and mixed phase between Ni₁₂P₅ and Ni. Moreover, phosphide was released when the reduction temperature was increased and the nickel phosphides changed to mixed phase. The mixed phase between Ni₂P and Ni₁₂P₅ dispersed well on the activated carbon and

showed high conversion and selectivity on HDO reaction of palmitic acid. In contrast, the nickel in metallic form showed low activity.

In addition, siliceous Santa Barbara Amorphous (SBA-15) is another choice of support for HDO reaction. SBA-15 is a mesoporous silica with uniform hexagonal pores with a narrow pore size distribution, high thermal stability and high surface area. Such properties could help a dispersion of the active phase (Soni et al., 2013; Huirache-Acuña et al., 2013; Thielemann et al., 2011).

Yang et al. (2012) reported that Ni₂P/SBA-15 catalyst showed very promising performance in the HDO reaction of methyl oleate with selectivity of 60%. The catalyst had high efficiency in removal oxygen for DCO₂ and HDO pathway.

Thus this work, nickel phosphide was loaded on the activated carbon produced from a tube furnace (AC_TF), from Iwasaki kiln (AC_IW) and SBA-15 by wet impregnation method. Particularly, utilization of AC_IW and AC_TF are produced from Lead tree wood was a new innovation.

6.3 Experimental

6.3.1 Preparation of activated carbon

Charcoals from Iwasaki kiln and tube furnace were used to produce activated carbon by a procedure modified from literature (Ngernyen et al., 2006). The obtained charcoal was ground by using ball mill, sieved in size of 1.70 mm-250 μm and dried at 100°C overnight in a hot-air oven. Then, the dried charcoal (4 g) was filled in a ceramic boat and placed at the middle of a horizontal tube furnace (Carbolite, UK) with a length of 122.2 cm and internal diameter of 3.8 cm and purged with nitrogen for about 15 min. The setup of activating equipment is shown in Figure

6.1. The temperature was increased from room temperature to 800°C at a heating rate of 10°C/min under the flow of nitrogen (100 ml/min, Lind Gas, 99.995%). After the nitrogen flow was stopped, carbon dioxide (Lind Gas, 99.9%) was flowed into the furnace at a constant flow rate of 100 ml/min and held for 1 h. After that the power was switched off and the furnace was allowed to cool to ambient temperature under the flow of nitrogen. The obtained activated carbon was collected and stored in a desiccator for further analysis. The activated carbons of charcoal from Iwasaki kiln and tube furnace were named AC_IW and AC_TF, respectively.

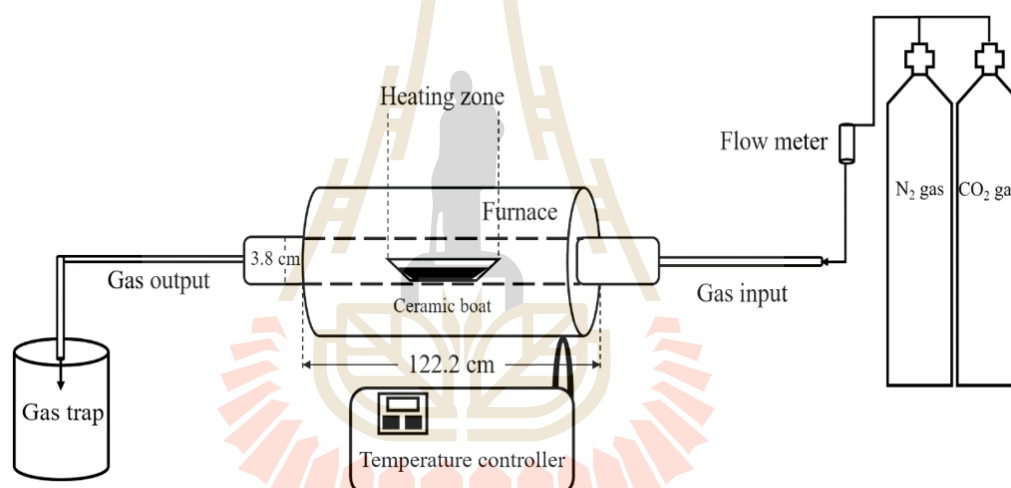


Figure 6.1 Equipment setup for activation in a horizontal tube furnace.

6.3.2 Preparation of NiP/AC by wet impregnation

The method preparation was applied from literature (Xin et al., 2016) with nickel loading of 10 wt.% and the Ni/P ratio was 0.5. Briefly, firstly, the dried-activated carbon was ground and immersed in 1 M ammonia solution (NH₃•H₂O, Carlo Erba, 30%) for 18 h and then washed with DI water until a neutral pH. Then, the sample was dried at 100°C for 12 h and calcined at 600°C for 4 h under nitrogen

atmosphere (N_2 flow rate 50 ml/min). Secondly, 1.5 g of di-ammonium hydrogen phosphate ($(NH_4)_2HPO_4$, Carlo Erba, 98%) was dissolved in 10 ml of DI water and stirred. Then, 1.6 g of the nickel nitrate hexahydrate ($Ni(NO_3)_2 \cdot 6H_2O$, UNILAB, 97%) was added into the solution, stirred and adjusted pH 2-3 with 0.5 M nitric solution (HNO_3 , Sigma-Aldrich, 70%) to produce a clear solution. Finally, 6 g of calcined-activated carbons were impregnated with aqueous solution of nickel phosphate, stirred for 3 h, sonicated for 30 min at room temperature, dried at $100^\circ C$ and calcined at $600^\circ C$ for 4 h under nitrogen atmosphere. The sample was named “calcined-NiP/AC_IW and calcined-NiP/AC_TF”.

6.3.3 Synthesis of siliceous SBA-15

SBA-15 was synthesized by method modified from literature (Yang et al., 2012). Pluronic[®] P123 ($EO_{20}PO_{70}EO_{20}$, Sigma-Aldrich, 35% (PEG)) (3.74 g) was dissolved in 152.6 ml of 1.5 M hydrochloric solution (HCl, Sigma-Aldrich, 37%) in a three-neck round-bottom flask, stirred and refluxed at $40^\circ C$ for 24 h. Then, 8.7 ml of tetraethoxysilane (TEOS, Sigma-Aldrich, 99%) was slowly added into the mixture and kept at $40^\circ C$ for 5 h. The mixture was transferred into a 275-ml Teflon-lined stainless steel autoclave and aged at $100^\circ C$ for 24 h. After cooling down, the solid product was centrifuged at 4000 rpm for 5 min and washed with DI water until pH 7. The solid product was dried at $60^\circ C$ for 12 h and calcined at $550^\circ C$ for 16 h (heating rate of $1^\circ C/min$). The sample called “calcined-SBA-15”.

6.3.4 Preparation of NiP/SBA-15 by wet impregnation

The method preparation was modified from literature (Guan et al., 2016; Soni et al., 2013) with metal loading of 10 wt. % and the mole ratio of Ni/P ratio was 0.5. Di-ammonium hydrogen phosphate ($(NH_4)_2HPO_4$, Carlo Erba, 98%) (1.98 g) was

dissolved in 20 ml of DI water and stirred. Then, 2.18 g of the nickel nitrate hexahydrate ($\text{Ni}(\text{NO}_3)_2 \cdot 6\text{H}_2\text{O}$; UNILAB, 97%) was added into the solution, stirred and adjusted pH 2-3 with 0.5 M nitric solution (HNO_3 , Sigma-Aldrich, 70%) to produce a clear solution. Four grams of calcined-SBA-15 was gradually added into the mixture and stirred for 30 min at room temperature. Then, the sample was sonicated for 30 min to increase the metal dispersion, evaporated the water, dried at 105°C overnight and calcined at 500°C for 3 h. The sample called “calcined-NiP/SBA-15”.

6.3.5 Catalyst characterization

The morphology of reduced catalysts was analyzed by scanning electron microscopy (SEM, JEOL model JSM-6400) and transmission electron microscopy (TEM, JEOL model JEM-2100). In TEM sample preparation, a small amount of the sample was dispersed into 1 ml of ethanol ($\text{C}_2\text{H}_6\text{O}$, Sigma-Aldrich, 99%), sonicated for 10 min and dropped on carbon film on 200-square-mesh copper grid and dried. The grid was put into TEM sample holder and inserted into vacuum chamber. The voltage for electron acceleration was 200 mV.

Phase of samples was studied by X-ray diffraction (XRD) on a Bruker AXS D8 diffractometer using Ni filtered $\text{Cu K}\alpha$ radiation with at 40 kV and 40 mA with a step increment of 0.02 degree and step time of 0.5 s. Crystal sizes were calculated from Scherrer equation:

$$D = \frac{K\lambda}{\beta \cos \theta}$$

Where D is the mean size of crystallite (domains).

K is a dimensionless shape factor, about 0.89.

λ is the X-ray wavelength.

β is the line broadening in radians (FWHM).

θ is the Bragg angle (in degrees).

Nitrogen adsorption-desorption isotherms were obtained from a BELSORP-mini II. Before analysis, about 0.15 g of each sample was purged with helium and then pretreated at 150°C under vacuum system. Surface and pore size distribution were obtained from Brunauer-Emmett-Teller (BET) method and Non-Local Density Functional Theory (NL-DFT) method, respectively.

6.3.6 Catalytic deoxygenation testing

For palm oil HDO catalytic testing, the calcined catalyst was pressed to form pellets by hydraulic press, crushed and sieved to the size between 180 and 500 μm . The reaction was conducted in a continuous fixed-bed flow reactor with an internal diameter of 1 cm and length of 71 cm. For each run, 4 g of calcined catalyst was packed between SiC to improve heat transfer. The length of the catalyst-bed was 8 cm. Then, glass beads were fixed on both sides of the reactor to increase collecting time between the feed and the catalyst. The reactor set up is shown in Chapter V (Figure 5.1). The calcined catalysts NiP/AC_IW and NiP/AC_TF were reduced at 600°C under H₂ flow (30 ml/min), heating rate 2°C/min for 2 h and then cooled down under nitrogen gas and held overnight. The calcined catalyst NiP/SBA-15 was reduced at 5°C/min under flowing H₂-reduction at 650°C for 5 h, cooled to room temperature under the flow of nitrogen (20 ml/min) and held overnight.

To begin the testing process, nitrogen was switched off and the sample was pressurized with hydrogen (50 bar). Then, the catalyst was heated from room

temperature to desired testing temperature with a rate 10°C/min, held for 15 min and cooled down. After that, palm oil was fed to the reactor by an HPLC pump with the rate of 0.109 ml/min and mixed with hydrogen flow (109 ml/min, controlled by a mass flow controller). The pressure, collecting time, H₂ to oil ratio and liquid hourly space velocity (LHSV) in HDO testing were 50 bar, 3 h, 1,000:1 N(cm³/cm³) and 1 h⁻¹, respectively. Liquid and gas products were collected every 3 h.

The temperature testing in HDO reaction of NiP/AC_IW and NiP/AC_TF catalysts were at 350°C and NiP/SBA-15 was at 350 and 380°C. Testing conditions and product analysis were the same as those in Chapter V.

6.4 Results and discussion

6.4.1 Results from characterization and catalytic testing of NiP/AC

6.4.1.1 Catalyst morphology of NiP/AC from SEM and TEM

Figures 6.2(a)-(e) show the SEM images of reduced catalysts before testing in HDO reaction. Figure 6.2(a) and (d) show the morphology images of activated carbon and particle shape of nickel phosphide on the surface which was sphere and rod shapes (see Figure 6.2(b) and (e)). Figure 6.2(c) and (f) show the TEM images of reduced catalyst before testing in HDO reaction that the dark spots were the particle of nickel phosphide dispersion of the surface of activated carbon.

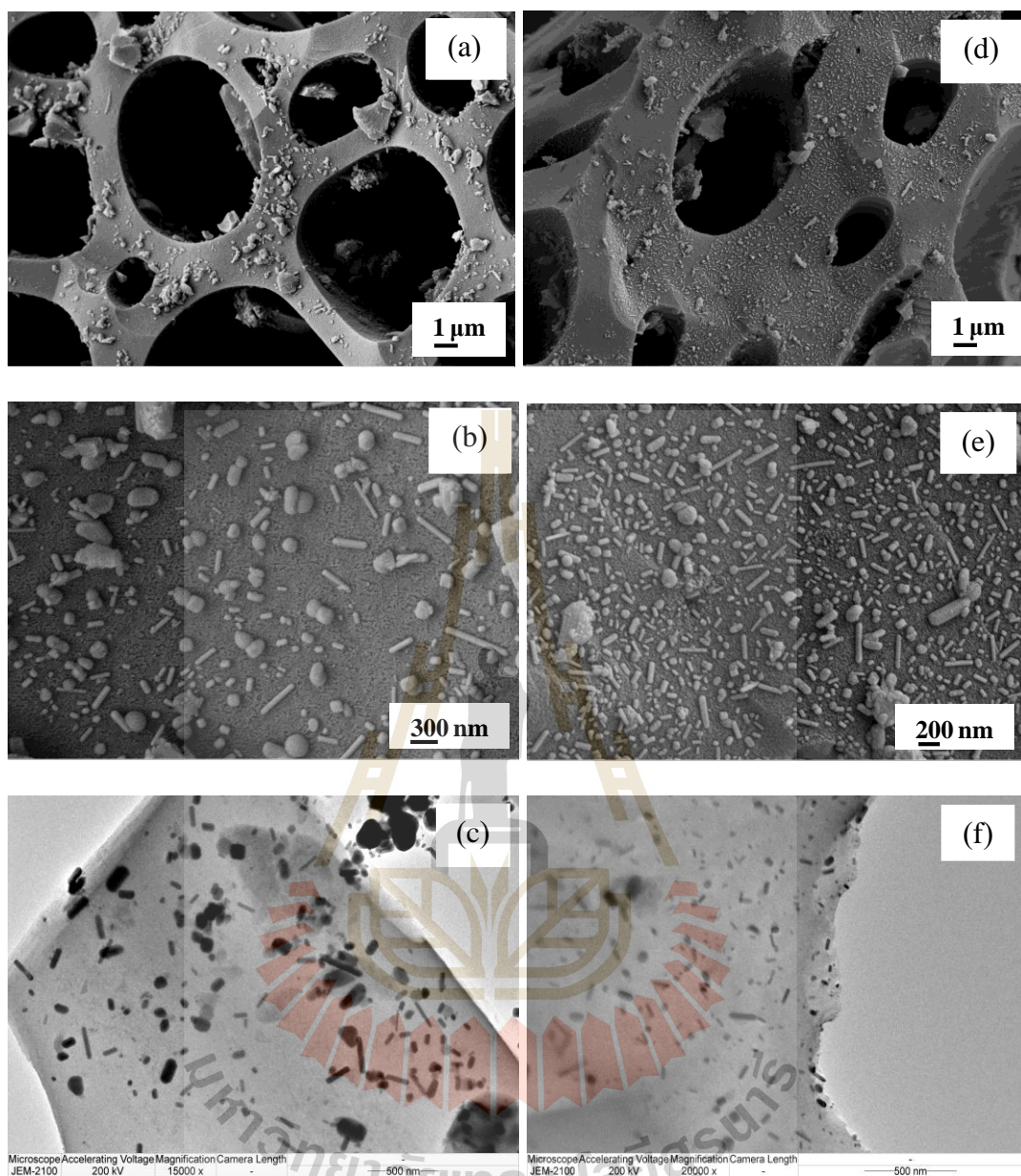


Figure 6.2 (a, b) SEM images and (c) TEM image of NiP/AC_IW; (d, e) SEM images and (f) TEM image of NiP/AC_TF.

6.4.1.2 Catalysts characterization by XRD

Figure 6.3(a) and (b) show the XRD patterns of NiP/AC_IW and NiP/AC_TF, respectively. The peaks from both fresh- and spent-catalysts were sharp indicating crystalline phase. The fresh-catalysts had peaks at $2\theta = 40.7, 44.6, 47.4,$

54.2 and 55.0° corresponding to Ni₂P phase (PDF 01-089-2742). The Ni₂P has a hexagonal structure and the space group p-62 m with the following lattice parameters $a = b = 5.859 \text{ \AA}$ and $c = 3.382 \text{ \AA}$ (Kucernak et al., 2014; Xin et al., 2016). After reaction, the diffraction peaks of spent-catalyst showed the mixed phase between Ni₂P and Ni₁₂P₅ (PDF 01-089-2742 and PDF 00-022-1190). The diffraction peaks of Ni₁₂P₅ were at $2\theta = 38.3$ and 48.9° . The Ni₁₂P₅ has a tetragonal structure with lattice parameters $a = b = 8.646 \text{ \AA}$ and $c = 5.07 \text{ \AA}$ (Kucernak et al., 2014; Xin et al., 2016). Yang et al. (2015) reported the ratios of Ni/P changed to form Ni₁₂P₅ because the phosphorous was partly released during the reaction as volatile species (e.g. P and PH₃). Xin et al. (2016) varied the molar ratio of Ni/P and tested in deoxygenation reaction of palmitic acid, suggesting Ni₂P crystallite showed a poorer dispersion than Ni₁₂P₅. Ni₂P coexisted with Ni₁₂P₅ catalysts dispersed well on the carbon surface. From the spent catalyst, additional peaks at $2\theta = 20.1$ and 29.9° were observed, corresponding to Ni(PO₃)₂ (PDF 00-028-0708) as a monoclinic structure with the following lattice parameters $a = 11.086 \text{ \AA}$, $b = 8.227 \text{ \AA}$ and $c = 9.832 \text{ \AA}$. These nickel phases were appeared from re-oxidation in air of catalyst after the reaction.

The crystallite sizes of Ni₂P in the fresh NiP/AC_IW and NiP/AC_TF calculated by Scherrer equation were 18.4 and 26.2 nm, respectively. The smaller crystallite size indicated a better dispersion which could lead to a better catalytic activity. In the spent catalysts the intensities of the phase Ni₂P on both catalysts decreased significantly due to partial transformation to the phase Ni₁₂P₅. It was possible that the phase change might mainly occur on the surface of the crystals due to the exposure to hydrogen in the catalytic testing process.

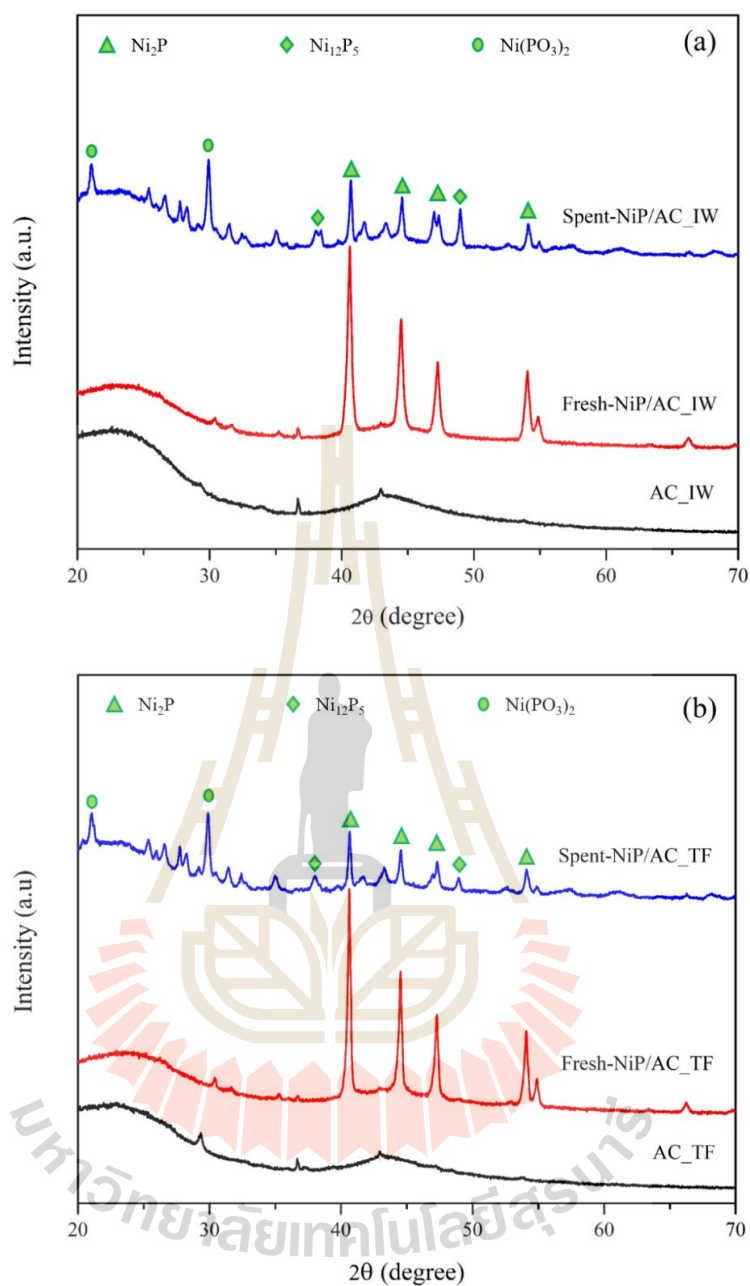


Figure 6.3 XRD patterns of (a) NiP/AC_IW, (b) NiP/AC_TF.

6.4.1.3 Catalysts characterization by nitrogen adsorption-desorption

Nitrogen sorption isotherms and pore size distributions of all activated carbons samples are shown in Figure 6.4(a, c) and (b, d), respectively. Surface areas and pore volumes are reported in Table 6.1. The isotherms of all

samples were mixed type I and type IV according to the IUPAC classification of a characteristic of microporous materials and a narrow hysteresis loop of mesoporous materials in a broad pressure range, respectively. The adsorbed volumes on supported Ni₂P were lower than the bare support because the metal phosphides dispersed in the pores and surface area that were micropore volume (V_{micro}) and external surface area (S_{ext}) were decreased (see Table 6.1). The BET surface area (S_{BET}) of AC_IW and NiP/AC_IW were 593 and 578 m²/g, respectively. The small decrease in surface area of NiP/AC_IW might indicate a good dispersion in micropores, consistent with the XRD results. On the other hand, the S_{BET} of AC_TF and NiP/AC_TF were 935 and 670 m²/g, respectively. The larger decrease in surface area of NiP/AC_TF from the bare support might indicate a poorer dispersion of nickel phosphae species.

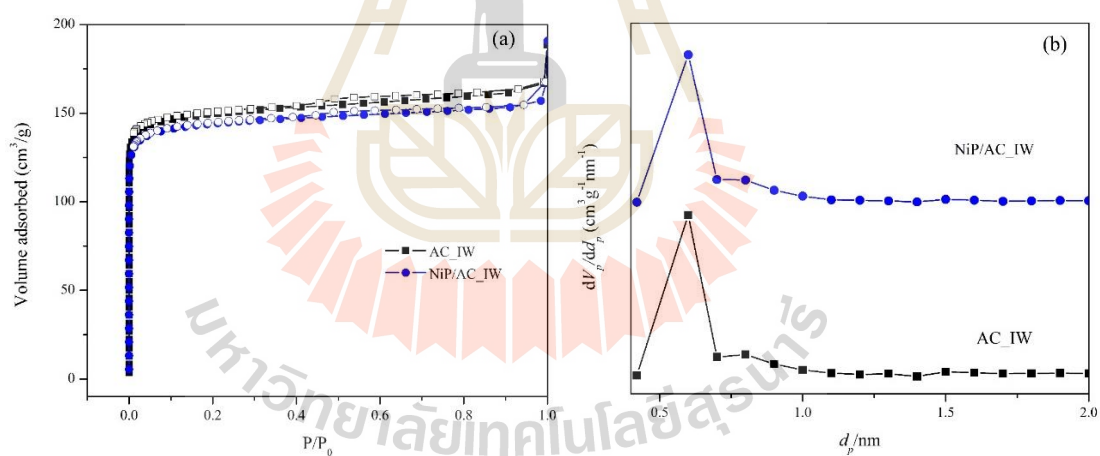


Figure 6.4 (a) Adsorption-desorption isotherms, (b) pore size distributions of nickel catalyst; filled: adsorption, empty: desorption.

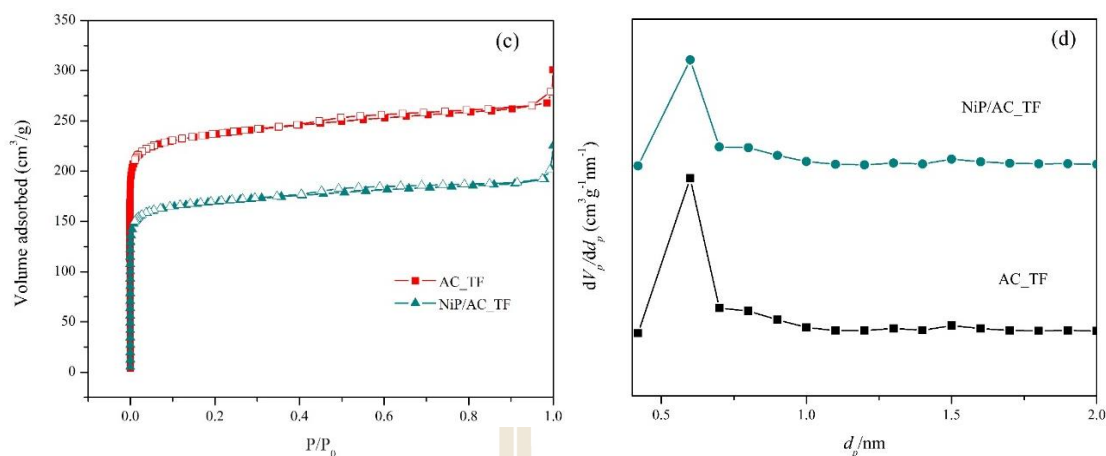


Figure 6.4 (Continued) (c) Adsorption-desorption isotherms, (d) pore size distributions of nickel catalyst; filled: adsorption, empty: desorption.

Table 6.1 Nitrogen adsorption-desorption analysis of activated carbon and NiP/AC catalysts.

Sample	S_{BET}^a (m^2/g)	V_{micro}^b (cm^3/g)	V_{meso}^c (cm^3/g)	V_{total}^d (cm^3/g)	D_p^e (nm)	S_{ext}^f (m^2/g)
AC_IW	593	0.253	0.038	0.258	1.738	12.2
NiP/AC_IW	578	0.243	0.037	0.249	1.728	8.9
AC_TF	935	0.408	0.083	0.421	1.844	20.5
NiP/AC_TF	670	0.245	0.067	0.309	1.801	12.0

Note: a = BET surface area, b = Micropore volume, c = Mesopore volume, d = Total pore volume, e = Mean pore diameter, f = External surface area

6.4.1.4 Catalytic hydrotreating of palm oil

Figure 6.5(a) shows conversion of triglyceride, product yield, selectivity of C_{15} to C_{18} and competitive reaction of NiP/AC_IW and NiP/AC_TF

catalysts. At the collecting time 3 h, NiP/AC_TF catalysts showed a complete conversion but NiP/AC_IW catalyst gave a higher BHD yield and selectivity. From collecting time at 6 h, the complete conversions were obtained from both catalysts. NiP/AC_IW catalyst gave a significantly higher BHD yield and selectivity. The better catalytic performance of NiP/AC_IW could be attributed from the better dispersion of Ni₂P. At collecting time 9 h the complete conversions were still obtained from both catalysts and NiP/AC_IW catalyst gave a significantly higher BHD yield and selectivity. The yield and selectivity from both catalysts from the collecting time 9 h were slightly lower than from 6 h indicating that the catalyst had deactivation due to adsorption of by-products such as coke that can hinder the access to the active size. In addition, partial re-oxidation of phosphorous by water, a by-product of HDO could cause the activity decay (Yang et al., 2015). Higher crystallite size of Ni₂P in NiP/AC_TF resulted in less active sites than NiP/AC_IW, thus, amount of BHD products was slightly lower. The NiP/AC_TF was selective to HDO products while NiP/AC_IW was selected to DCO products (see Figure 6.5(b)). Gas products from the reactions were propane (C₃H₈) and CO (see Figure 6.5(c)). The optimum collecting time was 6 h and the best catalyst was NiP/AC_IW.

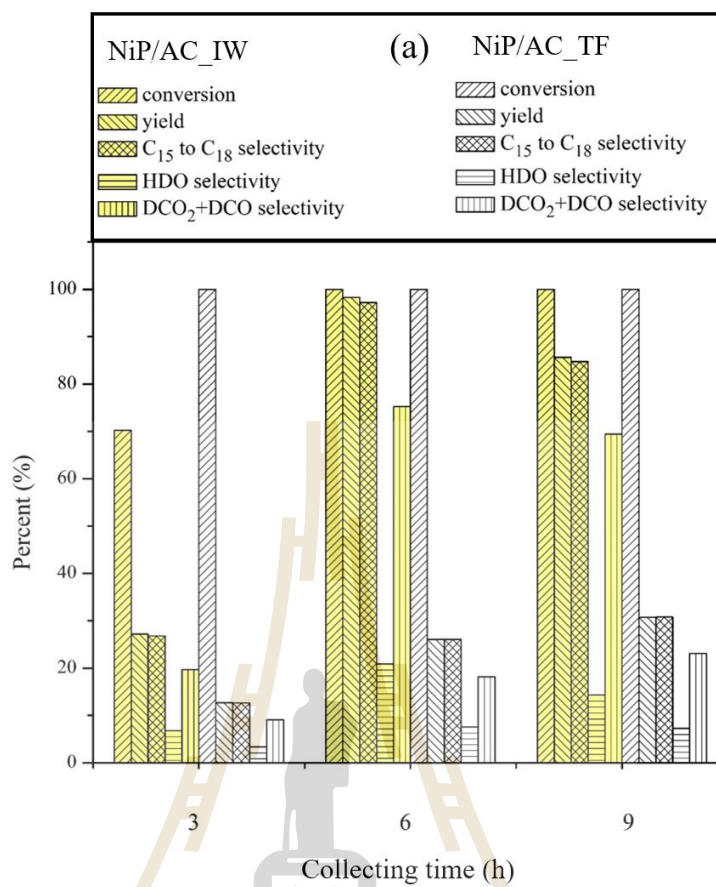


Figure 6.5 (a) Conversion, product yield, selectivity of C₁₅ to C₁₈ and competitive reaction of NiP/AC_IW and NiP/AC_TF catalysts.

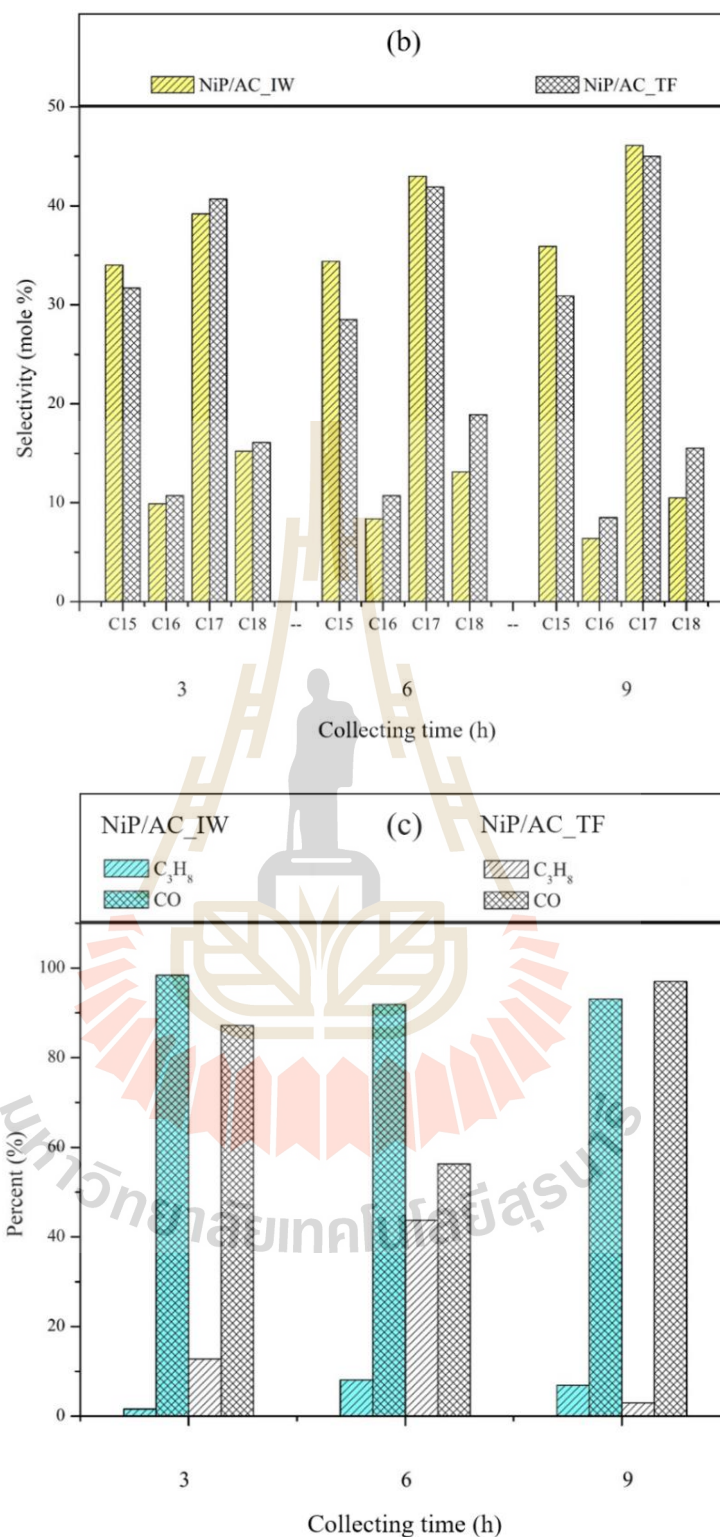


Figure 6.5 (Continued) (b) Selectivity, (c) gas product distribution of NiP/AC_IW and NiP/AC_TF catalysts.

6.4.2 Results from characterization and catalytic testing of NiP/SBA-15

6.4.2.1 Catalyst morphology of NiP/SBA-15 from SEM and TEM

Figure 6.6(a) and (c) show the SEM images of parent SBA-15 and reduced NiP/SBA-15 catalyst before testing in HDO reaction, respectively. The parent SBA-15 sample showed rope-like nano-structure. After loaded with nickel phosphide, the morphology was well-defined wheat-like nano-structure with small particles less than 100 nm and had small particle on the rough surface area of sample (see Figure 6.6(c)). TEM image, a typical hexagonal pore structure of SBA-15 with network channel, uniform pore sizes, and long-range ordering are shown in Figure 6.6(b). Figure 6.6(d) and (e) show TEM images of reduced and spent NiP/SBA-15, respectively. The morphology of the catalyst did not change significantly. Small particles of nickel phosphide were observed as dark spots dispersing in the channels. In addition, there were some large particles of the nickel phase on the external surface. The structure of SBA-15 did not collapse after loading with phosphide, consistent with the XRD result.

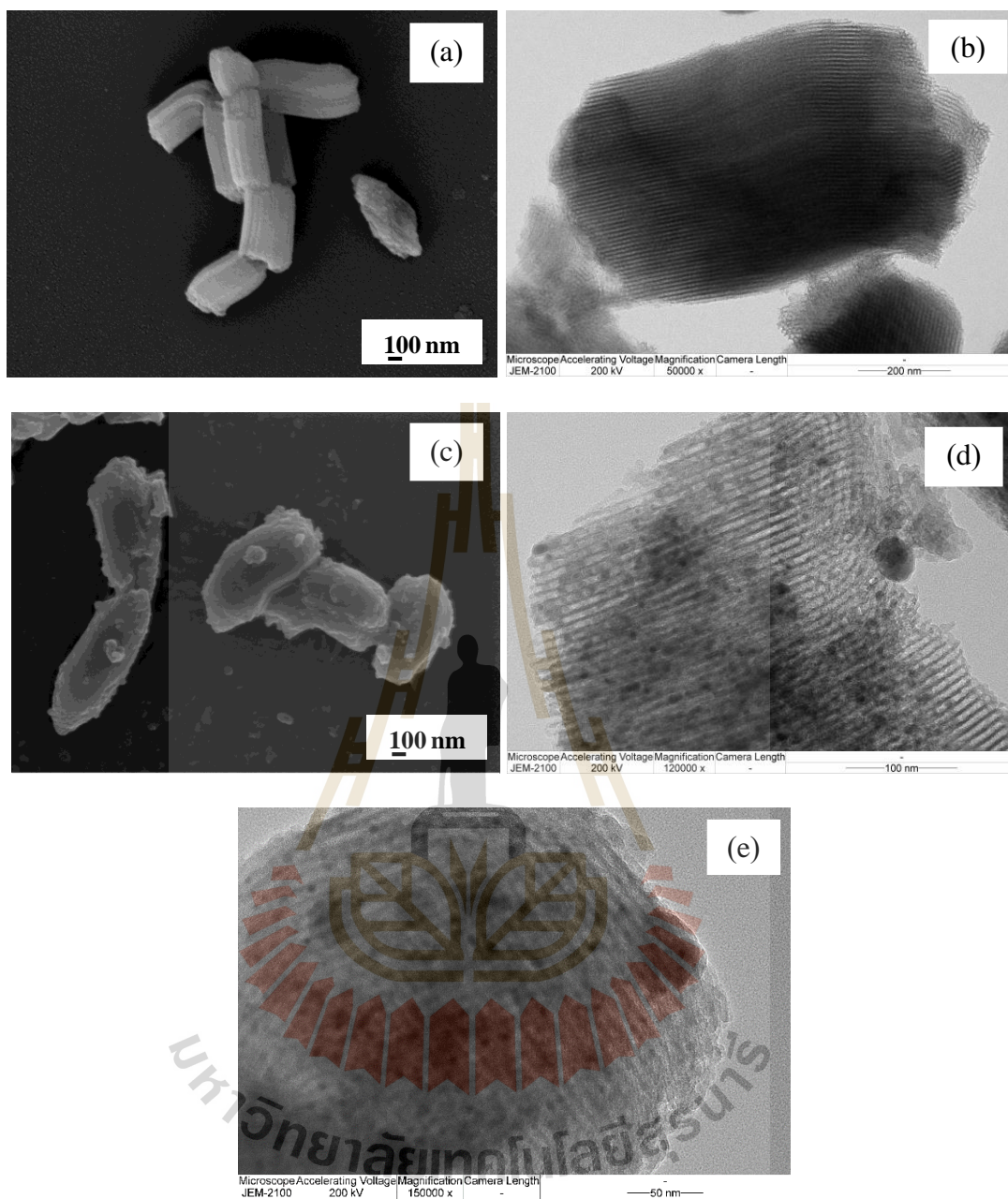


Figure 6.6 SEM images of (a) SBA-15 and (c) reduced NiP/SBA-15; TEM images of (b) SBA-15, (d) reduced NiP/SBA-15, (e) spent NiP/SBA-15.

6.4.2.2 Catalysts characterization by XRD

Figure 6.7(a) and (b) show XRD patterns of SBA-15 at low angle range and NiP/SBA-15 catalyst, respectively. The SBA-15 shows three diffraction

peaks consisting of a sharp peak at low angle around $2\theta = 0.75^\circ$ corresponding to the plane (100) and two weak peaks at $2\theta = 1.5$ and 1.8° corresponding to the planes (110) and (200), respectively (Liu et al., 2004). These diffraction peaks were related to long range 2D hexagonal order of P6mm symmetry structure (Thielemann et al., 2011). Figure 6.7(b), the fresh NiP/SBA-15 catalyst had peak at $2\theta = 40.7, 44.6, 47.2$ and 54.0° as a characteristic peak of Ni_2P (PDF 01-089-2742). After reaction, the diffraction peaks of the spent NiP/SBA-15 catalyst showed the mixed phase between Ni_2P and Ni_{12}P_5 (PDF 01-089-2742 and PDF 00-022-1190). The diffraction peaks of Ni_{12}P_5 were at $2\theta = 38.3$ and 48.9° . These results clearly explained that ratio of Ni/P changes the active phase in the final catalyst (Sonic et al., 2013).

The crystallite size of Ni_2P in the fresh catalyst calculated by Scherrer equation was 25.4 nm. In the spent catalyst, the peak intensities of the phase Ni_2P decreased due the transformation to Ni_{12}P_5 . The crystallite size of Ni_{12}P_5 in the spent NiP/SBA-15 was 27.0 nm. A broad diffraction peak of SBA-15, fresh NiP/SBA-15 and spent NiP/SBA-15 was sharp and shifted at low $2\theta = 22.4, 22.1$ and 21.5° , respectively. These peak positions were amorphous phase of silica (PDF 00-051-1593).

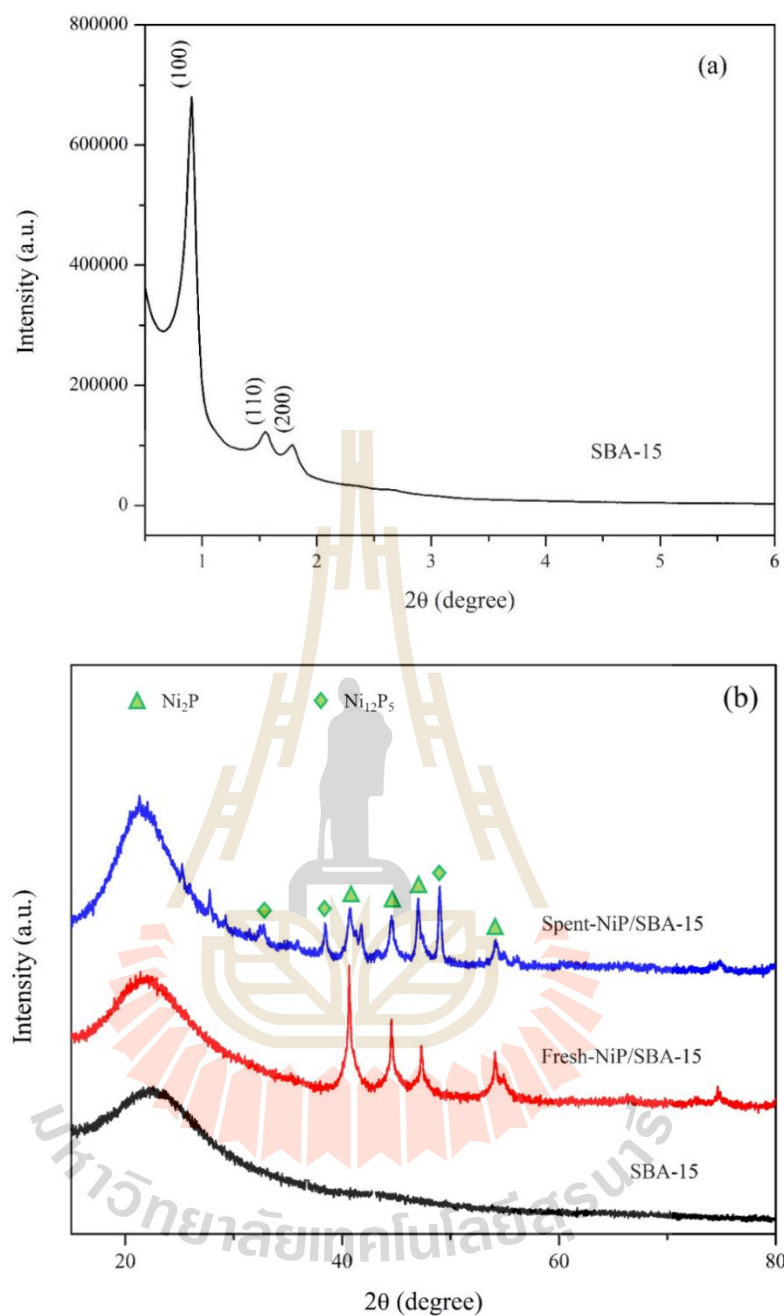


Figure 6.7 XRD pattern of (a) SBA-15 at low angle range, (b) SBA-15, fresh- and spent-NiP/SBA-15 at broad angle range catalysts.

6.4.2.3 Catalysts Characterization by nitrogen adsorption-desorption

Nitrogen sorption isotherms and pore size distributions of all samples are shown in Figure 6.8(a) and (b), respectively. All the samples show a

typical IV isotherm, which is characteristic of mesoporous materials that classified by IUPAC (1985). Unloaded SBA-15 displayed a hysteresis loop of type H1 and had narrow pore distribution centered at 8.1 nm. After loading of the nickel phosphide, hysteresis loops significantly change their shape and desorption branch showed two steps, which indicated the creation of bottle necks in the SBA-15 channels (Yang et al., 2015). The narrow pore distribution centered of NiP/SBA-15 was 5.1 and 8.1 nm (see Figure 6.8(b)). Thielemann et al. (2011) reported that the narrowed and blocked mesoporous causes delayed evaporation leading to a lower desorption pressure P/P_0 and changes in the shape of desorption branch of the isotherm. Then, tensile strength effect was observed at $P/P_0 = 0.45$ leading to a forced closure of the hysteresis loop. It depended on temperature and adsorptive dependent. In addition, the both surface area and pore volumes decreased. Surface area of unloaded SBA-15 and NiP/SBA-15 was decreased from 707 to 314 m^2/g , respectively. It can conclude that nickel phosphides were mainly located inside the channel of the mesostructured silica.

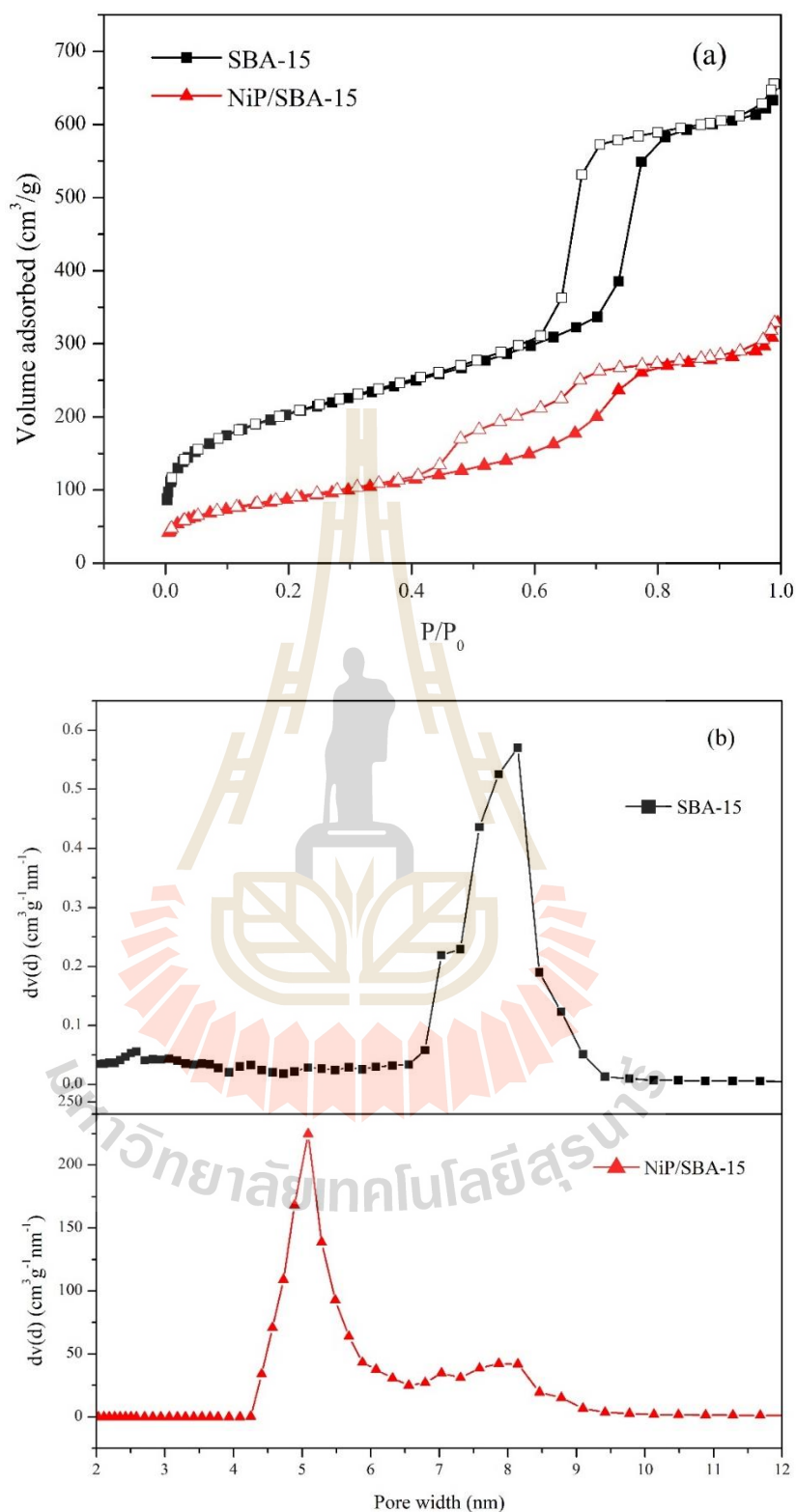


Figure 6.8 (a) Nitrogen adsorption-desorption isotherms, (b) pore size distribution of unloaded SBA-15 and NiP/SBA-15; filled: adsorption, empty: desorption.

6.4.2.4 Catalytic hydrotreating of palm oil

Figure 6.9(a) shows conversion of triglyceride, product yield, selectivity of C₁₅ to C₁₈ and competitive reaction of NiP/SBA-15 catalysts. All of the collecting times of catalyst showed completed conversion of triglyceride. The product yield and competitive reaction increased at the collecting time of catalyst from 3 h to 6 h, while a higher BHD yield and competitive reaction were at 6 h. At collecting time 9 h the product yield was slightly decreased indicating that the catalyst deactivation like adsorption of by-product such as coke that can hinder the access to the active size. In addition, partial re-oxidation of phosphorous by water as a by-product of HDO caused by activity decay (Yang et al., 2015). At 6 h was selective to HDO product, while at 9 h was selective to DCO₂+DCO products. Distribution of gas products are shown in Figure 6.9(b). Carbon monoxide (CO), propane (C₃H₈), ethane (C₂H₆), carbon dioxide (CO₂) and methane (CH₄) were produced. More gas products were obtained with the long reaction collecting time and high pressure indicating more cracking (Itthibenchapong et al., 2017). Thus, NiP/SBA-15 catalyst favored cracking in three pathways of HDO, DCO and DCO₂. Then DCO was the favorable pathways.

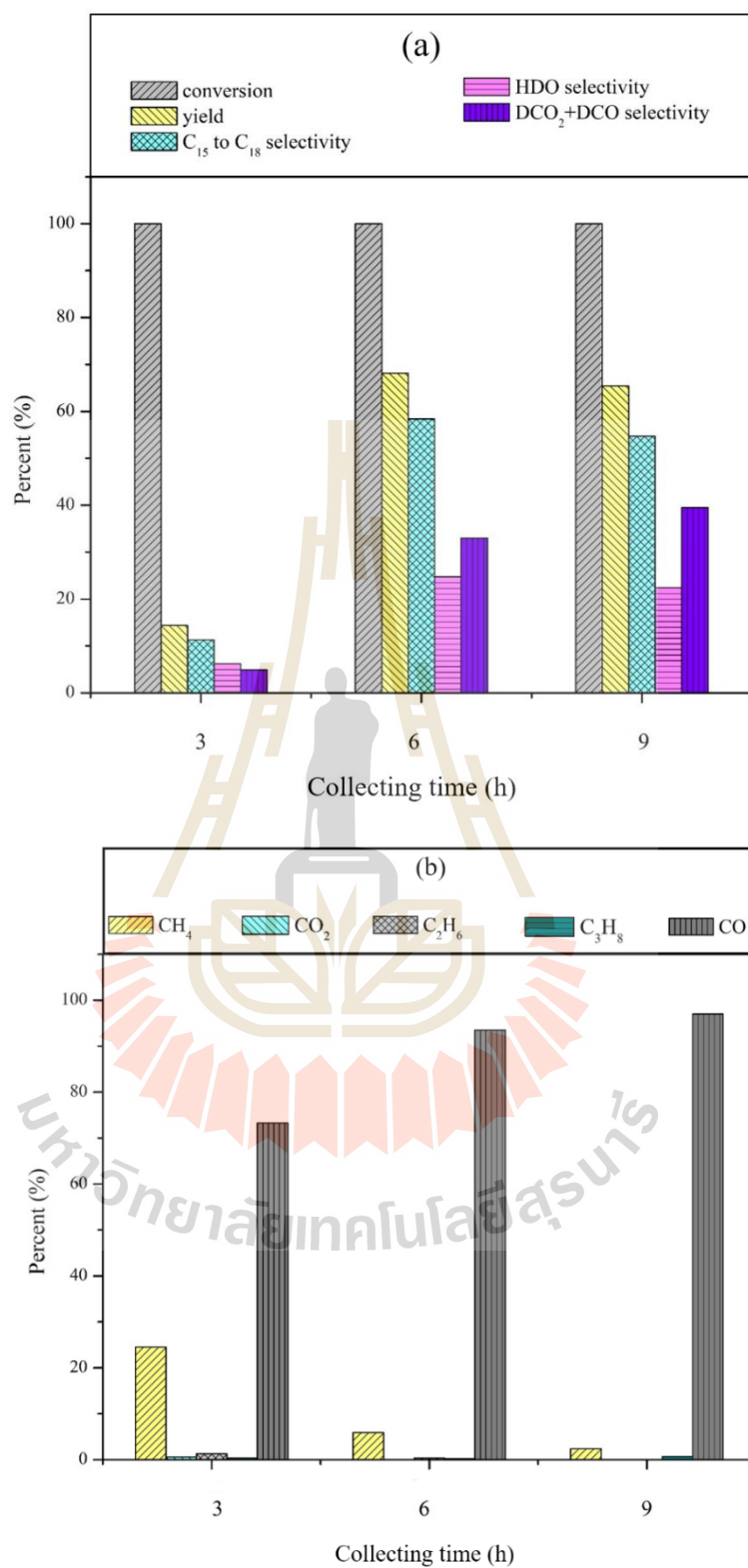


Figure 6.9 (a) Conversion, product yield, selectivity of C₁₅ to C₁₈ and competitive reaction, (b) gas product distribution of NiP/SBA-15 catalysts.

Table 6.2 shows the properties of BHD product including color, pour point and cloud point from NiP/AC_IW, NiP/AC_TF and NiP/SBA-15 catalysts. All of the products showed clear color (see Figure 6.10) and high quality of fuel which low pour point and cloud point. Soletio-Boyás et al. (2012) reported the high properties of liquid hydrocarbon product that had pour point and cloud point less than 20°C.

In the future, with cracking properties of the NiP/SBA-15 catalyst can be used to produce jet fuel-like hydrocarbons that are C₁₀-C₁₂.

Table 6.2 The physical properties of BHD product.

Catalysts	Color	Pour point/Cloud point (°C)	
		Collecting time 6 h	Collecting time 9 h
NiP/AC_IW	Clear	7.0/8.0	6.0/7.0
NiP/AC_TF	Clear	7.0/8.0	7.0/8.0
NiP/SBA-15	Clear yellow	2.0/4.0	8.0/12.0

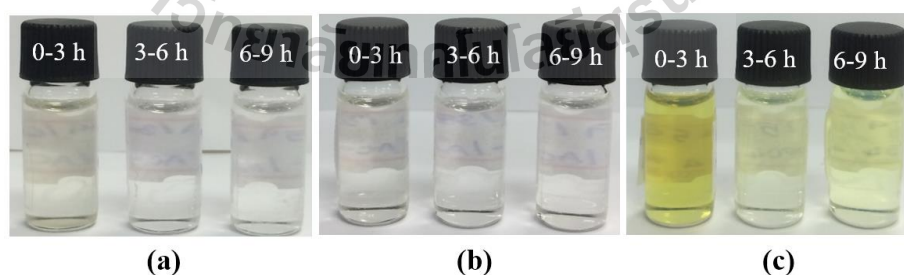


Figure 6.10 BHD product from (a) NiP/AC_IW, (b) NiP/AC_TF, (c) NiP/SBA-15 catalysts.

6.5 Conclusions

The NiP/AC_IW, NiP/AC_TF and NiP/SBA-15 catalysts were prepared by wet impregnation method and characterized by XRD, SEM, TEM and N₂ sorption analysis. After reduction, all catalysts contained pure phase of Ni₂P phase. The crystallite sizes of Ni₂P on NiP/AC_IW, NiP/AC_TF and NiP/SBA-15 were 18.4, 26.2 and 25.4 nm, respectively. On AC, Ni₂P were mainly in micropores with a better dispersion on AC-IW. On SBA-15, Ni₂P were mainly in mesopores. The NiP/AC_IW catalyst showed the best performance in HDO to produce BHD product. Both of NiP/AC_IW and NiP/SBA-15 catalysts were selectivity to DCO activity. From the sample collected after 6 h, the NiP/SBA-15 catalyst was more selective to HDO product than NiP/AC_IW catalyst. After the catalytic testing all catalyst contained a mixed phase of Ni₂P and Ni₁₂P₅.

6.6 References

- Arun, N., Sharma, R. V., and Dalai, A. K. (2015). Green diesel synthesis by hydrodeoxygenation of bio-based feedstocks: Strategies for catalyst design and development. **Renewable and Sustainable Energy Reviews**. 48: 240-255.
- Guan, Q., Wan, F., Han, F., Liu, Z., and Li, W. (2016). Hydrodeoxygenation of methyl palmitate over MCM-41 supported nickel phosphide catalysts. **Catalysis Today**. 259: 467-473.
- Huirache-Acuña, R., Nava, R., Peza-Ledesma, C. L., Lara-Romero, J., Alonso-Núñez, G., Pawelec, B., and Rivera-Muñoz, E. M. (2013). SBA-15 mesoporous silica

- as catalytic support for hydrodesulfurization catalysts. **Materials**. 6(9): 4139-4167.
- Itthibenchapong, V., Srifa, A., Kaewmeesri, R., Kidkhunthod, P., and Faungnawakij, K. (2017). Deoxygenation of palm kernel oil to jet fuel-like hydrocarbons using Ni-MoS₂/γ-Al₂O₃ catalysts. **Energy Conversion and Management**. 134: 188-196.
- Jambulingam, M., Karthikeyan, S., Sivakumar, P., Kiruthika, J., and Maiyalagan, T. (2007). Characteristic studies of some activated carbons from agricultural wastes. **Journal of Scientific and Industrial Research**. 66: 495-500.
- Kucernak, A. R. J., and Sundaram, V. N. N. (2014). Nickel phosphide: the effect of phosphorus content on hydrogen evolution activity and corrosion resistance in acid medium. **Journal of Materials Chemistry A**. 2: 17435-17445.
- Liu, Y. M., Cao, Y., Yi, N., Feng, W. L., Dai, W. L., Yan, S. R., and Fan, K. N. (2004). Vanadium oxide supported on mesoporous SBA-15 as highly selective catalysts in the oxidative dehydrogenation of propane. **Journal of Catalysis**. 224(2): 417-428.
- Ngernyen, Y., Tangsathitkulchai, C., and Tangsathitkulchai, M. (2006). Porous properties of activated carbon produced from Eucalyptus and wattle wood by carbon dioxide activation. **Korean Journal of Chemical Engineering**. 23(6): 1046-1054.
- Phooratsamee, W., Hussaro, K., Teekasap, S., and Hirunlabh, J. (2014). Increasing adsorption of activated carbon from palm oil shell for adsorb H₂S from biogas production by impregnation. **American Journal of Environmental Sciences**. 10(5): 431-445.

- Soni, K. K., Boahene, P. E., Rambabu, N., Dalai, A. K., and Adjaye, J. (2013). Hydrotreating of coker light gas oil on SBA-15 supported nickel phosphide catalysts. **Catalysis Today**. 207: 119-126.
- Sotelo-Boyás, R., Trejo-Zárraga, F., and de Jesús Hernández-Loyo, F. (2012). Hydroconversion of triglycerides into green liquid fuels. In Hydrogenation. **InTech**. 187-215.
- Thielemann, J. P., Girgsdies, F., Schlögl, R., and Hess, C. (2011). Pore structure and surface area of silica SBA-15: influence of washing and scale-up. **Beilstein Journal of Nanotechnology**. 2: 110.
- Xin, H., Guo, K., Li, D., Yang, H., and Hu, C. (2016). Production of high-grade diesel from palmitic acid over activated carbon-supported nickel phosphide catalysts. **Applied Catalysis B: Environmental**. 187: 375-385.
- Yang, Y., Ochoa-Hernández, C., de la Peña O'Shea, V. A., Coronado, J. M., and Serrano, D. P. (2012). Ni₂P/SBA-15 as a hydrodeoxygenation catalyst with enhanced selectivity for the conversion of methyl oleate into n-octadecane. **American Chemical Society Catalysis**. 2(4): 592-598.
- Yang, Y., Ochoa-Hernández, C., Pizarro, P., Víctor, A., Coronado, J. M., and Serrano, D. P. (2015). Influence of the Ni/P ratio and metal loading on the performance of Ni_x P_y/SBA-15 catalysts for the hydrodeoxygenation of methyl oleate. **Fuel**. 144: 60-70.

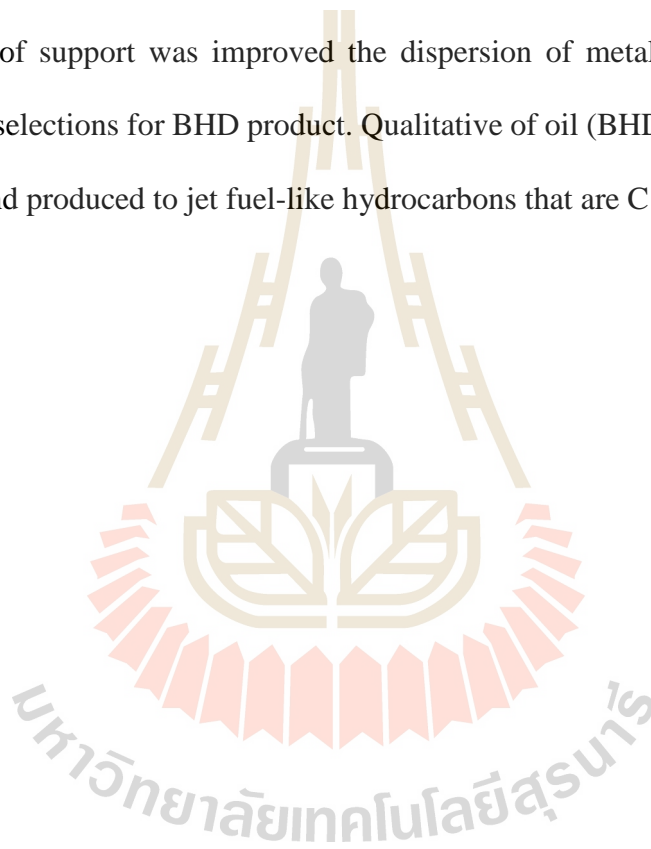
CHAPTER VII

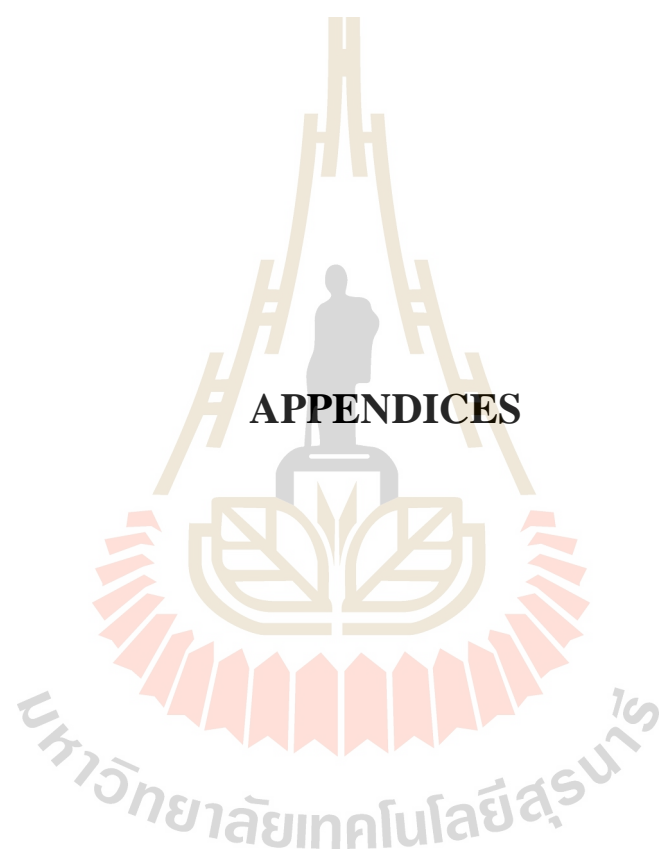
CONCLUSIONS AND RECOMMENDATION

In this thesis, charcoal was produced from *L. leucocephala* or Lead tree wood by carbonization in Iwasaki kiln and a lab scale-tubular furnace. In pyrolysis process, the activated carbon was produced by physical method, activation with CO₂ and chemical method, activation with ZnCl₂. After pyrolysis, the micropores and mesopores were generated and BET surface areas increased with increasing the activating temperature. In addition, the activation at 800°C gave high carbon content and C/H ratio indicating that high temperatures and long carbonization duration may intensify graphitization.

In application, catalytic testing for hydrodeoxygenation (HDO) of palm oil to produce bio-hydrogenated diesel (BHD), both activated carbon such as AC800IW and AC800TF were used as support for metal phosphide. The high surface area of support helped to disperse metal on the support and decreased agglomeration of metal. Bulk metal phosphides such as nickel, cobalt and copper were scanned and supported on the support for HDO reaction. Ni₂P is the best choice and supported on various support of activated carbon and siliceous SBA-15. The NiP/AC_IW, NiP/AC_TF and NiP/SBA-15 were prepared by wet impregnation. All of the catalysts showed completely conversion of palm oil to BHD product. The NiP/AC_IW showed the highest BHD yield at 97.2% in the reaction times of 6 hand selective to decarbonylation (DCO) through gas product distribution was propane (C₃H₈) and carbon monoxide (CO).

Therefore, in future work for applications of activated carbon from *L. leucocephala* wood was suggesting that the surface area will be modified by physical method following chemical activation because the only physical activation method gave high surface area but is not removed the CaCO_3 species from the surface area. The activated carbon from *L. leucocephala* wood will be used as a raw material to produce graphene (rGO) and applied to valuable for supercapacitor. For the HDO reaction, the high surface area of support was improved the dispersion of metal, but did not help to increase and selections for BHD product. Qualitative of oil (BHD) can be improved by distillation and produced to jet fuel-like hydrocarbons that are $\text{C}_{10}\text{-C}_{12}$.





APPENDICES

APPENDIX A

CALIBRATION CURVES OF STANDARDS

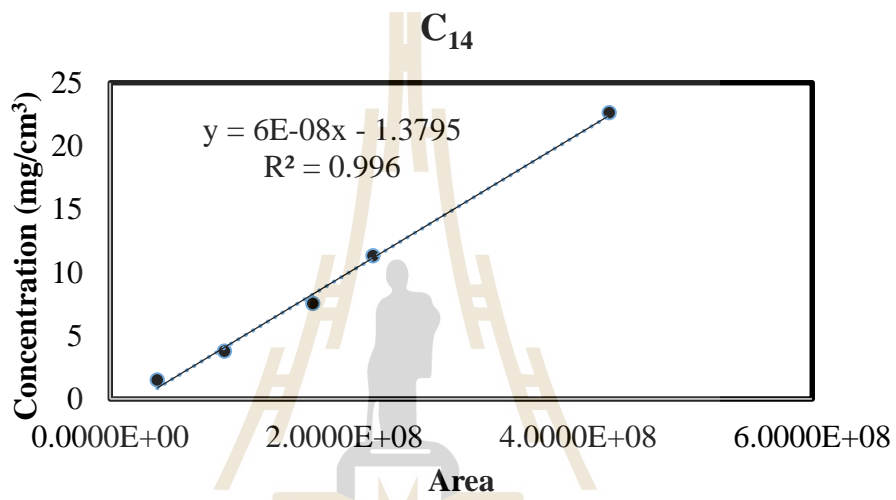


Figure A-1 Calibration curve of Tetradecane (C₁₄).

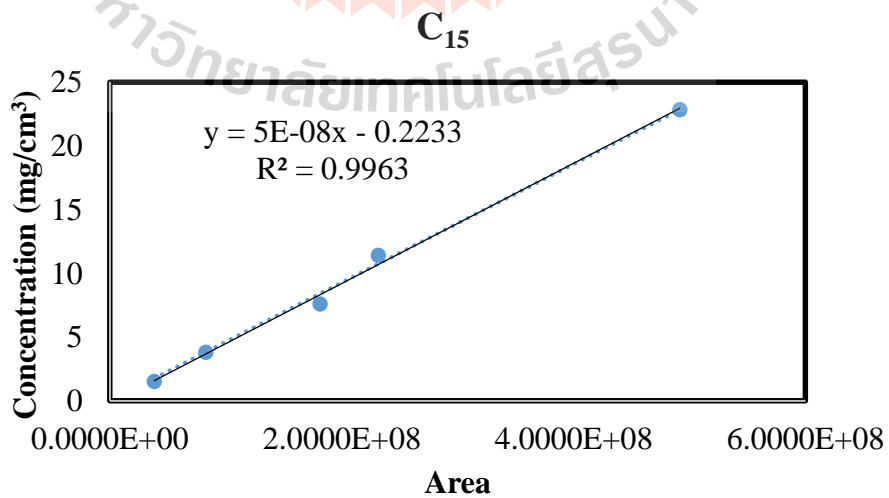


Figure A-2 Calibration curve of Pentadecane (C₁₅).

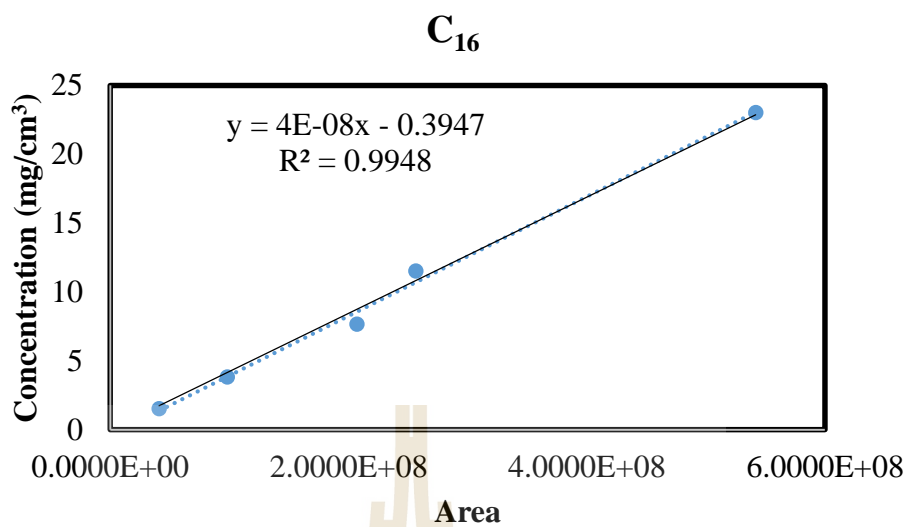


Figure A-3 Calibration curve of Hexadecane (C₁₆).

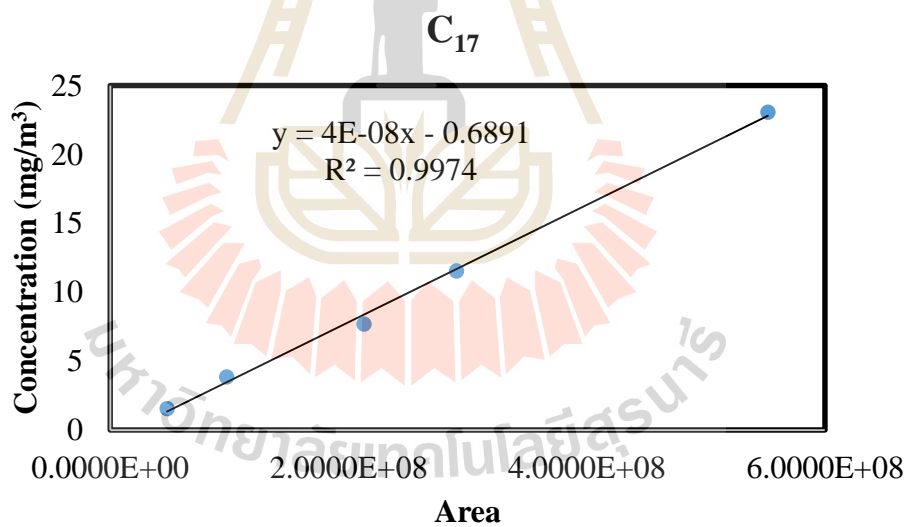


Figure A-4 Calibration curve of Heptadecane (C₁₇).

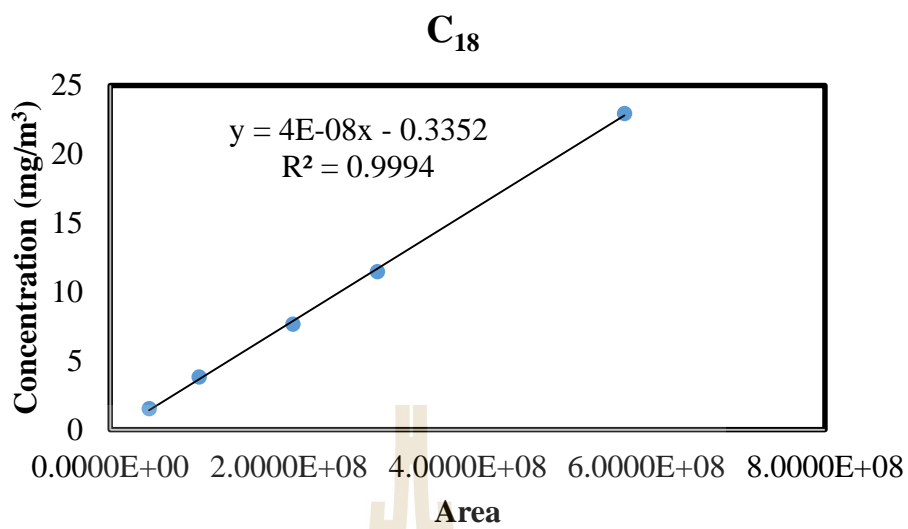
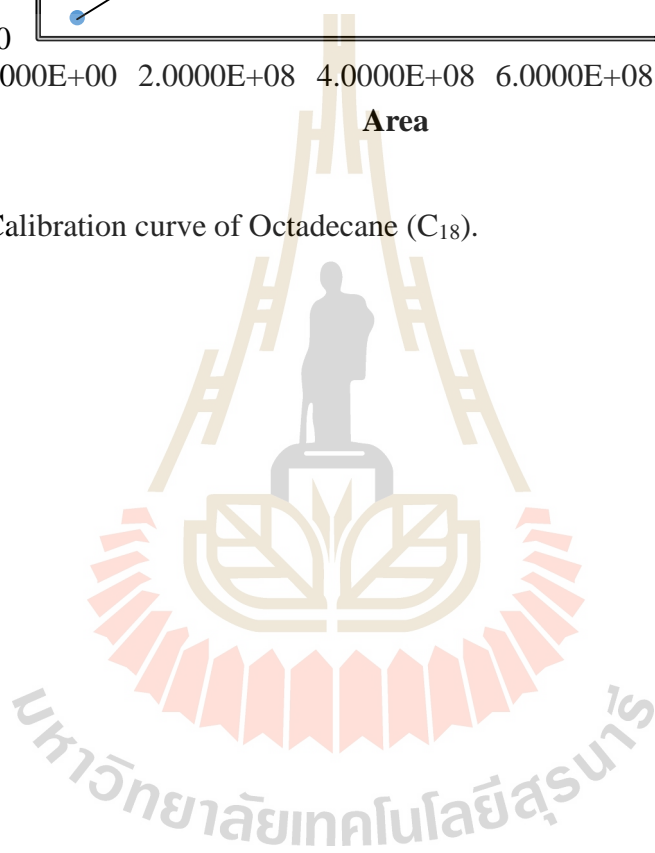


Figure A-5 Calibration curve of Octadecane (C₁₈).



APPENDIX B

CHROMATOGRAMS OF STANDARDS AND SAMPLES

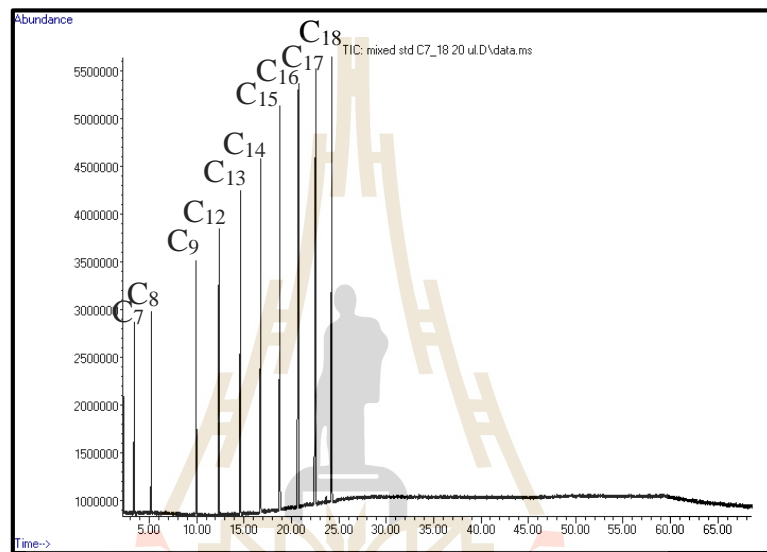


Figure B-1 Chromatogram of mixed standard with concentration of 20 $\mu\text{l}/\text{mg}$.

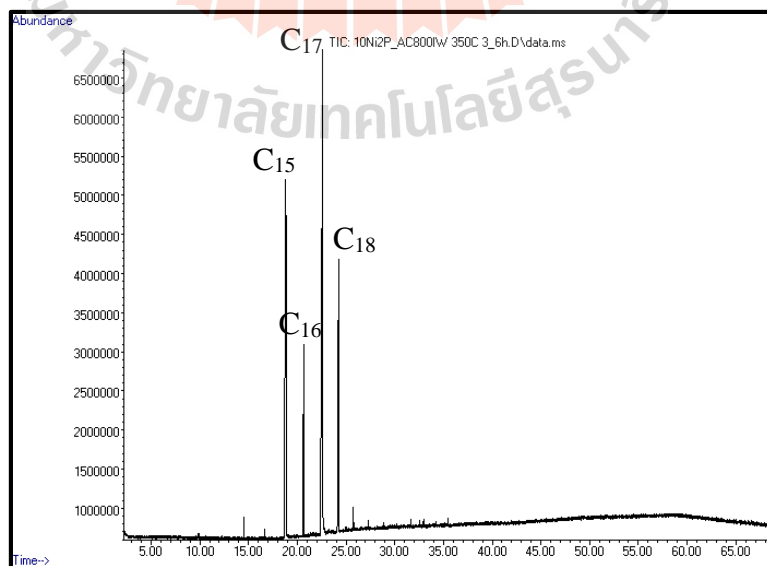


Figure B-2 Chromatogram of NiP/AC_IW sample at collecting time 6 h.

CURRICULUM VITAE

Name Miss Mustika Pimsuta
Birth date 31 March 1986
Address 34/85 Moo 6, Tambon Nongkrok, Amphoe Muang, Sisaket, 33000,
Thailand

Education

2013-2016 Ph.D. (Chemistry), Suranaree University of Technology, Thailand
with scholarship from Thai government, “Science Achievement
Scholarship of Thailand, SAST”

2009-2012 M.Sc. (Chemistry), Suranaree University of Technology, Thailand
with scholarship from Thai government, “Science Achievement
Scholarship of Thailand, SAST”

2005-2008 B.Sc. (Chemistry), Ubon Ratchathani University, Thailand with
scholarship from Thai government, “Science Achievement
Scholarship of Thailand, SAST”

Publication

Pimsuta, M., Sosa, N., Deekamwong, K., Keawkumay, C., Thathong, Y., Rakmae, S.,
Junpirom, S., Prayoonpokarach, S., and Wittayakun, J. (2018). Charcoal and
wood vinegar from pyrolysis of Lead tree wood and activated carbon from
physical activation. **Suranaree Journal of Science and Technology**. 25(2):
177-190.